Ultrafast Dynamical Studies of Two Dimensional Transition Metal Dichalcogenides

by

Meixin Cheng

A thesis
presented to the University of Waterloo
in fulfillment of the
thesis requirement for the degree of
Doctor of Philosophy
in
Chemistry

Waterloo, Ontario, Canada, 2022

Examining Committee Membership

The following served on the Examining Committee for this thesis. The decision of the Examining Committee is by majority vote.

External Examiner:	Daniel Kuroda Associate Professor, Dept. of Chemistry, Louisiana State University
Supervisor:	German Sciaini Associate Professor, Dept. of Chemistry, University of Waterloo
Internal Member:	Scott Hopkins Associate Professor, Dept. of Chemistry, University of Waterloo
	Adam Wei Tsen Assistant Professor, Dept. of Chemistry, University of Waterloo

Internal-External Member: Micheal Pope

Associate Professor, Dept. of Chemical Engineering,

University of Waterloo

Author's Declaration

This thesis consists of material all of which I authored or co-authored: see Statement of Contributions included in the thesis. This is a true copy of the thesis, including any required final revisions, as accepted by my examiners.

I understand that my thesis may be made electronically available to the public.

Statement of Contributions

I declare that I am the sole author of Chapters 1, 2, 5, and 6, which were not part of any of our published or submitted manuscripts.

Chapters 3 and 4 have been adapted from:

Portions of Chapter 3:

1. M. Cheng, S. Zhong, N. Rivas, T. Dekker, A. A. Petruk, P. Gicala, K. Pichugin, F. Chen, X. Luo, Y. Sun, A. W. Tsen, G. Sciaini,"Persistent photogenerated state attained by femtosecond laser irradiation of thin T_d-$MoTe_2$". *J. Phys. Chem. C.* **126** 13840-13846 (2022); also in arXiv.2205.09792 (2022).

DOI = 10.1021/acs.jpcc.2c03987

https://pubs.acs.org/doi/10.1021/acs.jpcc.2c03987

This work was done in collaboration with the groups of Prof. Adam Wei Tsen (Chemistry, Institute for Quantum Computing, UW) and Prof. Yuqing Sun (Key Laboratory of Materials Physics, Chinese Academy of Sciences). The single crystal of $1T'$-$MoTe_2$ was grown by Prof. Sun's group. The thin flakes were prepared by Prof. Tsen's group. The Si_3N_4 windows were fabricated by Dr. Ariel A. Petruk (Chemistry, UeiL, UW). I carried out femtosecond transient absorption measurements with Gicala, Rivas, and Pichugin. I performed data analysis with Spyder. I interpreted the results and wrote the manuscript with Sciaini, who directed this work.

2. M. Cheng, S. Zhong, N. Rivas, T. Dekker, A. A. Petruk, P. Gicala, K. Pichugin, F. Chen, X. Luo, Y. Sun, A. W. Tsen, G. Sciaini,"Photoinduced interlayer dynamics in T_d-

$MoTe_2$: a broadband pump-probe study". *Appl. Phys. Lett.* **120**, 123102 (2022); also in arXiv:2201.04961 (2022).

DOI = 10.1063/5.0084986

https://doi.org/10.1063/5.0084986

This work is a continuation of the previous study ("Persistent photogenerated state attained by femtosecond laser irradiation of thin T_d-$MoTe_2$"). I carried out femtosecond transient reflectivity measurements. I performed data analysis with Spyder. I interpreted the results and wrote the manuscript with Sciaini, who directed this work.

Portions of Chapter 4:

3. M. Cheng, K. Pichugin, A. Maas, M. Schleberger, G. Sciaini, "Out-of-plane longitudinal sound velocity in SnS_2 determined via broadband time-domain Brillouin scattering". *J. Appl. Phys.* **132**, 075107 (2022); also in arXiv.2207.06488 (2022).

DOI = 10.1063/5.0103224

https://doi.org/10.1063/5.0103224

This work was done in collaboration with the group of Prof. Marika Schleberger (University of Duisburg Essen). The sample was purchased from HQ Graphene and characterized by XPS and Raman spectroscopy in Schleberger's group. I carried out femtosecond transient reflectivity measurements. I performed data analysis with Spyder. I interpreted the results and wrote the manuscript with Sciaini, who directed this work.

4. P. Gicala[#], M. Cheng[#], T. S. Lott, K. Du, S-W. Cheong, A. A. Petruk, K. Pichugin and G. Sciaini, "Time-resolved broadband impulsive stimulated Brillouin scattering in single

crystal hematite" (#equal contributions). *Appl. Lett. Phys.* **118**, 264101 (2021).

DOI = 10.1063/5.0057604

https://doi.org/10.1063/5.0057604

This work was done in collaboration with the group of Prof. S-W. Cheong, who prepared a single crystal of Hematite. P. Gicala performed femtosecond transient reflectivity measurements. I carried out data analysis with Spyder. I interpreted the results and wrote the manuscript with Sciaini, who directed this work.

5. N. Rivas, T. Dekker, S. Zhong, A. A. Petruk, Patrick Gicala, M. Cheng, F. Chen, X. Luo, Y. Sun, K. Pichugin, A. W. Tsen and G. Sciaini, "Generation and detection of coherent longitudinal acoustic waves in ultrathin $1T'$-$MoTe_2$". *Appl. Phys. Lett.* **115**, 223103 (2019); also in arXiv.1911.05789.

DOI = 10.1063/1.5125862

https://doi.org/10.1063/1.5125862

This work was done in collaboration with the groups of Prof. Tsen and Prof. Sun. The single crystal of $1T'$-$MoTe_2$ was grown by Prof. Sun's group. The thin flakes were prepared by Prof. Tsen's group. The Si_3N_4 windows were fabricated by Dr. Ariel A. Petruk (Chemistry, UeiL, UW). I carried out femtosecond transient absorption measurements with Gicala, Rivas, and Pichugin. I performed data analysis with Spyder. I interpreted the results and wrote the manuscript with Sciaini and Rivas, who directed this work.

There are two additional published manuscripts that I have co-authored and which are not presented in my thesis:

1. D. Shen, H. Yang, C. Spudat, T. Patel, S. Zhong, F. Chen, J. Yan, X. Luo, M. Cheng, G. Sciaini, Y. Sun, D. A. Rhodes, T. Timusk, Y. N. Zhou, N. Y. Kim, and A. W. Tsen, "High-Performance Mid-IR to Deep-UV van der Waals Photodetectors Capable of Local Spectroscopy at Room Temperature". *Nano Lett.* **22**, 34253432 (2022); also in arXiv:2202.00049.

DOI = 10.1021/acs.nanolett.2c00741

https://doi.org/10.1021/acs.nanolett.2c00741

This work was done in collaboration with Prof. Tsen. I carried out the testing of the photodetector quantum efficiency in the deep-UV region with Daozhi Shen (Chemistry, Institute for Quantum Computing, UW).

2. M. Cheng[#], N. Rivas[#], S. J. Lim[#], K. Pichugin[#], A. A. Petruk, A. Klinkova, R. Smith, W. S. Hopkins, and G. Sciaini, "Trapping a Photoelectron behind a Repulsive Coulomb Barrier in Solution" ([#]equal contributions). *J. Phys. Chem. Lett.* **10**, 57425747 (2019).

DOI = 10.1021/acs.jpclett.9b01712

https://doi.org/10.1021/acs.jpclett.9b01712

This work was done before my direct transfer from the MSc to the Ph.D. program. I led all the experimental work and related data analysis. This work was done in collaboration with the groups of Prof. Scott Hopkins, Prof. Anna Klinkova, and Prof. Rodney Smith (Chemistry, UW). I carried out femtosecond transient absorption measurements with Rivas

and Pichugin. I performed spectroelectrochemistry measurement and data analysis with Spyder. I interpreted the results and wrote the manuscript with Hopkins and Sciaini, who directed this work.

Abstract

Layer transition metal dichalcogenides (TMDCs) have attracted great attention due to their unique electronic and optical properties. Specifically, single layer semiconducting TMDCs with their direct band gaps in the visible to near-infrared wavelength show great promise in boosting several applications in electronics, spintronics, optoelectronics, energy harvesting, etc. Different from the most famous monolayer material, graphene, they have more than one crystal structure, providing a tantalizing platform to investigate structural phase transition and possible photoinduced hidden phases. In this dissertation, we use femtosecond (fs) pump-probe techniques to explore the laser-induced phenomena in semimetal T_d-$MoTe_2$, as well as characterize the elastics properties of $MoTe_2$ and $2H$-SnS_2 single crystal. Moreover, we also investigate the exciton emission properties and dynamics in the bilayer of MoS_2/WS_2 heterostructure. This thesis is organized as follows:

Chapter 1 provides a general introduction to the structure and electronic properties of common TMDCs and the compounds studied in this thesis; i.e., $MoTe_2$, SnS_2, WS_2 and MoS_2. Chapter 2 describes the methodology employed, the principles of pump-probe spectroscopy, and the most commonly observed transient processes. Specifically, photo-induced dynamics in condensed matter and related time-resolved (tr) techniques that are applied for the study of the layered materials presented herein; i.e. time-resolved broadband transient absorption (tr-bb-TA) and time-resolved broadband transient reflectivity (tr-bb-TR) spectroscopy and femtosecond photoluminescence upconversion (fs-PLup) spectroscopy. Experimental results are presented and discussed in Chapter 3, 4 and 5. Chapter 3 and 4

have been adapted from our published work and manuscript(s) in preparation (see Statement of Contributions).

Chapter 3 involves tr-bb-TA and tr-bb-TR measurements performed on thin flakes and a bulk crystal of the semi-metallic $MoTe_2$ system, respectively. We investigated the photoinduced interlayer shear dynamics as a means to monitor a previously acclaimed ultrafast photoinduced phase transformation; i.e., a transition from the low temperature T_d state to the high-temperature $1T'$ phase that was reported to complete in only 700 fs[1]. In contrast, we found that photoexcitation of a single crystal of T_d-$MoTe_2$ leads to a transiently hot T_d-like state that dissipates the excess of energy into the bulk before having sufficient time to structurally transition to the $1T'$ phase. Moreover, this transiently hot T_d state was encountered to develop into a persistent strained state in thin flakes of T_d-$MoTe_2$, which present a much slower cooling rate owing to their semi free-standing geometry.

Chapter 4 illustrates the use of tr-bb-TR and tr-bb-TA techniques to characterize the elastic properties of bulk and thin-film 2D-transition metal dichalcogenides (2D-TMDCs), respectively. We were able to generate and detect coherent acoustic waves (CAWs) in thin-film $MoTe_2$ and in a bulk single crystal of SnS_2, and determined the longitudinal sound velocities in these materials. In the case of the bulk SnS_2 crystal, which is transparent in the probed wavelength range, the detection mechanism relies on Brillouin scattering (BS) and we derived the relevant formulae based on simple ray tracing.

Chapter 5 introduces the design, development, and implementation of our homemade fs-PLup instrument, which we applied to investigate the electron-hole recombination dy-

namics in semiconducting single- and few-layer 2D-TMDCs. Some preliminary results are presented and discussed in this chapter.

Finally, chapter 6 provides the general conclusions of our work and my future outlook.

Acknowledgements

I want to thank all the people without whom the research presented in this thesis would not have been possible. First, I would like to thank my Ph.D. supervisor, Dr. Germán Sciaini, for his guidance, mentorship, and encouragement during my journey. Back in 2017, I joined the UeIL group as a Master student, who had no experience in ultrafast spectroscopy. Dr. Sciaini not only taught me fundamental concepts about ultrafast spectroscopic but also led me to a new world where ultrafast spectroscopic techniques can be used to study the dynamics of materials in an extremely short time scale. I was amazed by what I learned and felt grateful to have his supervision. I then decided to transfer to the Ph.D. program and continue my academic pursuit under his supervision. During my Ph.D. journey, he also guided the project about investigating exciton dynamics in semiconducting 2D materials via femtosecond fluorescence spectroscopy and provided me with the experimental components. He also pointed out the key steps to solve the difficulties I faced during my academic research. I cannot thank him enough for his support, guidance, and encouragement during my graduate life.

I am also very fortunate to have an outstanding committee. Dr. Adam Wei Tsen, Dr. Micheal Pope, and Dr. Scott Hopkins. I'm grateful for their support and valuable feedback. Special thanks to our best collaborators from other groups. Prof. Tsen group at the University of Waterloo helped us exploit and transfer thin flakes of $MoTe_2$ on the special nano-fabricated substrates, and Prof. Sun group at the Key Laboratory of Materials Physics, Chinese Academy of Sciences provided us with the high-quality single crystal of

$MoTe_2$. Prof. Marika Schleberger group at the University of Duisburg Essen, and Prof. Andrei Vescan group at RWTH Aachen University provided us single layer and bilayer heterostructure TMDCs samples.

I am also grateful to all the past and current members of the UeIL. When I first came to the group, I knew very little about optical experiments, and it is Dr. Nicolas Rivas who is always kind and patient to train me to build up optical measurements and answer my questions. He also taught me how to use Python to analyze time-resolved data. I also want to express my thanks to our researcher associate, Dr. Kostyantyn Pichugin, who designed all software for time-resolved measurements and solve any issues with our electronic equipment. I also would like to thank Dr. Ariel A. Petruk, who is proficient in nano-fabrication, and prepared the specially nano-fabricated substrates for transient absorption measurements for nm-thick samples. I also want to thank all graduate student members, including Tyler Lott, Sam Netzke, Ruofei Zhang, Nicolette Adrienne Shaw, and Patrick Gicala, for their kind help in not only work but also in daily life.

Last but not least, I would like to thank my parents, sister, brother, and my boyfriend for their love and support all this time.

Dedication

To my parents, Jiangong Cheng and Lingru Zhang.

To my boyfriend, Yuan Chen.

To those years at UeiL.

– Meixin Cheng

Table of Contents

List of Figures

List of Abbreviations

2D two-dimensional

2D-TMDC 2D-transition metal dichalcogenide

BBO beta-barium borate

BGR bandgap renormalization

BS Brillouin scattering

CAW coherent acoustic wave

CB conduction band

CCD charge coupled device

CMOS complementary metal oxide semiconductor

CVD chemical vapor deposition

CWT continuous wavelet transform

DFT density functional theory

ESA excited state absorption

FED femtosecond electron diffraction

FFT fast Fourier transform

FS fused silica

fs femtosecond

fs-PLup femtosecond photoluminescence upconversion

FT Fourier transform

FWHM full width at high maximum

GSB ground-state bleaching

h-BN hexagonal boron nitride

IRF instrumental response function

ISBS Impulsive stimulated Brillouin scattering

ISRS impulsive stimulated Raman scattering

MOCVD metallo-organic CVD

ns nanosecond

OAP off-axis parabolic

OKE optical Kerr effect

OPA optical parametric amplifier

PIPT photoinduced phase transition

PL photoluminescence

pm picometers

PMT photomultiplier tube

ps picosecond

SBS stimulated Brillouin scattering

SE stimulated emission

SFG sum frequency generation

SHG second harmonic generation

SNR signal-to-noise ratio

SPM strain propagation model

STFT short-time Fourier transform

TA transient absorption

THz Terahertz

TMDC transition metal dichalcogenide

TR transient reflectivity

tr time-resolved

tr-ARPES time- and angle-resolved photoelectron spectroscopy

tr-bb-TA time-resolved broadband transient absorption

tr-bb-TR time-resolved broadband transient reflectivity

tr-PL time-resolved photoluminescence

tr-SHG time-resolved second harmonic generation

VB valence band

vdW van der Waals

WL white light

YAG Yttrium aluminum garnet

List of Tables

Chapter 1

Introduction

Following the great success of graphene regarding its novel electronic properties, it has also been equally impressive that other layer materials have been developed that can form atomically thin layers with remarkable properties. The family of two-dimensional (2D) materials is growing quite fast, and these include 2D-TMDCs, hexagonal boron nitride (h-BN), borophene (2D-boron), silicene (2D-silicon), germanene (2D-germanium), and MX-enes (2D-carbides/nitrides)[2]. 2D-TMDCs exhibit unique electrical and optical properties that evolve from the quantum confinement and surface effects that arise during the transition of an indirect band gap to a direct band gap when bulk materials are scaled down to monolayers. This tunable band gap in 2D-TMDCs is accompanied by strong photoluminescence (PL) and large exciton binding energy, making them promising candidates for a variety of optoelectronic devices, including solar cells, photo-detectors, light-emitting diodes, and photo-transistors[2].

1.1 Transition metal dichalcogenides (TMDCs)

1.1.1 Lattice structure of 2D-TMDCs

Layered TMDCs usually have the generic formula MX_2, where M stands for a transition metal (Mo, W, Ti, Nb, etc.) and X represents a chalcogen (S, Se, or Te). The typical crystal structure of 2D-TMDCs is shown in Figure 1.1. Note that TMDC materials containing group 4-10 transition metal have a layered structure; however, those with group 8-10 transition metals form, with some exceptions, non-layered structures[3]. The d orbitals of M and the p orbitals of X form a covalent bonding network within each layer, and the layers are held together by weak van der Waals (vdW) forces. The interlayer distances and the intralayer bond lengths generally increase with the size of M and X. Similar to graphene, weak vdW interlayer interactions allow the crystals to cleave easily. The metal coordination and the stacking order among individual layers define the phase of 2D-TMDCs. 2D-TMDCs are commonly presented as three main polymorphs, $1T$, $2H$ and $3R$[4]. Here, the numbers stand for the number of layers within the primitive unit cell and the letters stand for their symmetry (T-trigonal, H-hexagonal, and R-rhombohedral). The structure of these three polytypes is shown in Figure 1.2. The preferred phase that a given 2D-TMDC adopts depends predominantly on the d-electron count of M, and the relative size of M and X atoms[5]. All Group 4 transition metals have octahedral structures. Most of group 5 transition metals have octahedral structures, while some have trigonal-prismatic structures. Most of group 6 transition metals have trigonal-prismatic structures, while

some have octahedral structures. In group 7 octahedral structures are presented, but in this case, they are distorted. Finally, group 10 2D-TMDCs are all in octahedral structure[5].

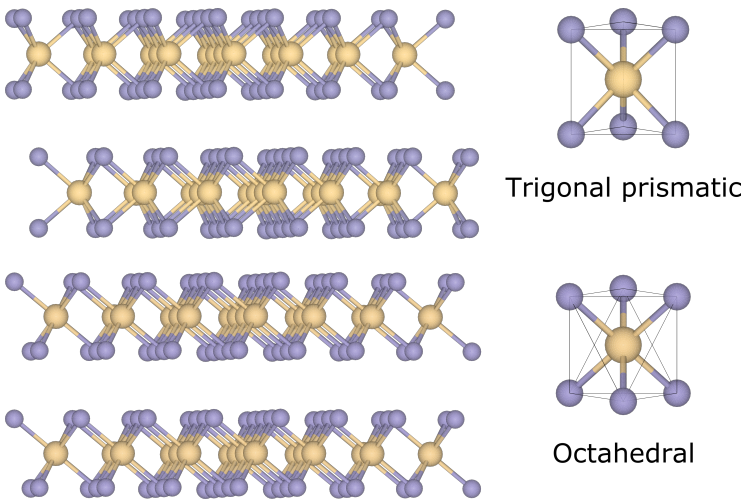

Figure 1.1: The structure of a typical layered TMDC. Left a three-dimensional representation of a typical layered MX_2 structure, with the metal atoms shown in yellow and the chalcogen atoms shown in purple. The local coordination of the metal species can be of the two types shown in the right panel, trigonal prismatic (top) and octahedral (bottom).

Monolayer TMDCs consist of 3 layers of atoms with chalcogen atoms on the top and bottom layers, forming a triangular lattice structure. The middle plane is a layer of transition metal atoms. The unit cell of a monolayer TMDC can take many forms. There are $2H$, $1T$ and $1T'$ structures. The most widely studied form is the $2H$ structure, which is the most stable phase. The atomic structure of $2H$ is shown in Figure 1.3. The $2H$ structure belongs to the D_{3h} point group and the $1T$ structure belongs to the D_{3d} point group. When preparing $2H$-single layers by dry methods such as Scotch-tape exfoliation, the yield of single layers

is normally low, but the crystal structure of the bulk-2H exfoliated layers keeps during the process. Note that the nomenclature '2'H is inconsistent with the definition mentioned above. The notation, in this case, refers to a single layer that has been obtained from a 2H-

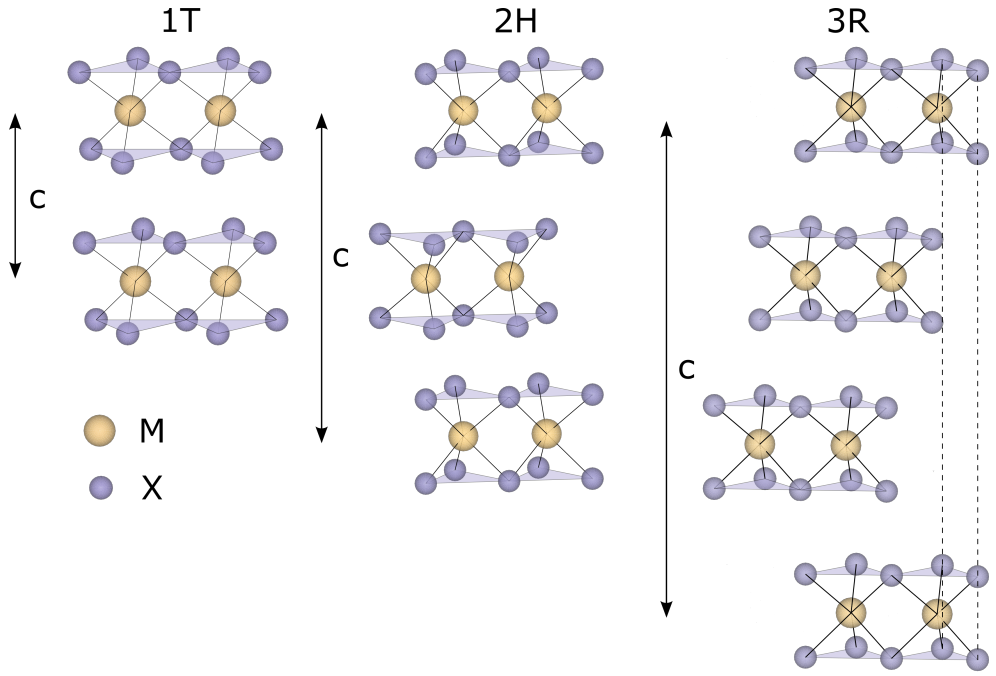

Figure 1.2: Schematics of the structural polytypes of TMDC from left to right 1T (prismatic trigonal symmetry, one layer per repeat, octahedral coordination of the metal), 2H (hexagonal symmetry, two layers per repeat, trigonal prismatic coordination) and 3R (rhombohedral symmetry, three layers per unit cell, trigonal prismatic coordination).

crystal and it is only preserved for consistency. The 1T phase is known to be metastable and undergoes a distortion with zigzag chains among the transition metal centres along the a axis, giving rise to the distorted 1T' phase as shown in Figure 1.3(c). The driving force for this distortion of the metal ions away from their ideal octahedral sites is usually discussed in terms of Peierls distortions[6,7]. Figure 1.4 shows the calculated equilibrium

relative energies of the phases ($2H$, $1T$ and $1T'$) of group 6 monolayer MX_2 using density functional theory (DFT), which are in agreement with experimental results[8]. As shown in Figure 1.4, there are energy differences among the different phases. It is straightforward to say that the feasible strategy for realizing a phase transition is to overcome the energy activation barrier, and various approaches are explored, such as alkali metal intercalation, strain, alloying, electrostatic gating, thermal treatment, etc[9]. Thus, in comparison to

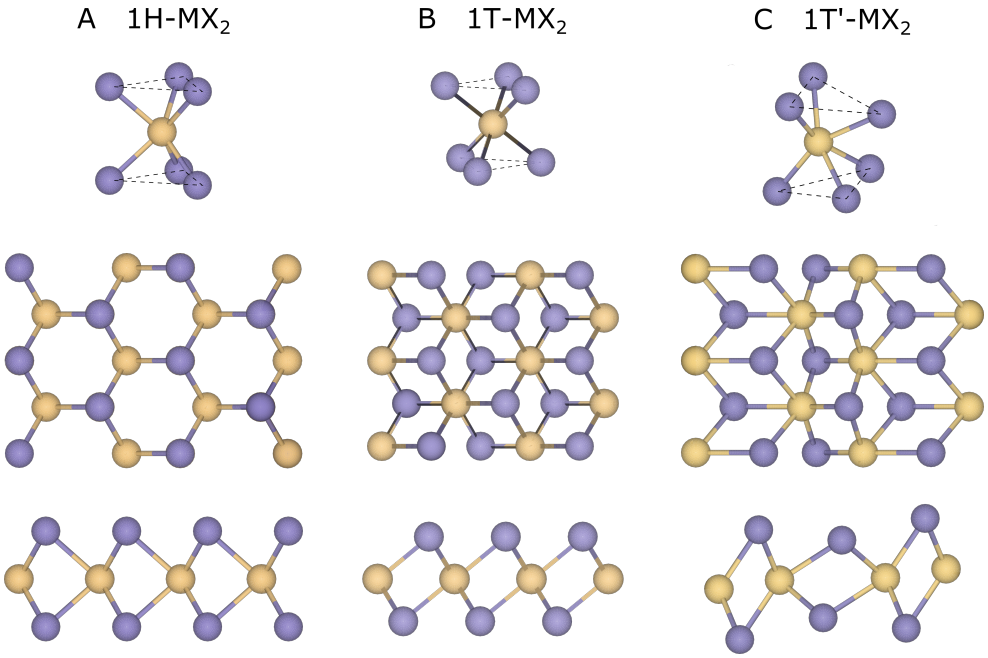

Figure 1.3: Top and side views of the three polymorphs of single layer MX_2: M stands for a transition metal and X stands for a chalcogen (Te, Se, or S). A. $1H$-MX_2, i.e., $2H$-MX_2, B. $1T$-MX_2. C. $1T'$-MX_2, distorted $1T$-MX_2

graphene, monolayer 2D-TMDCs have the attractive advantage of potentially presenting more than one crystal structure with different properties. In fact, the diversity of electronic properties has broadened the application range of 2D-TMDCs, especially within the limit

of a few layers that can provide more opportunities for flexible, low-power, and transparent electronic devices.

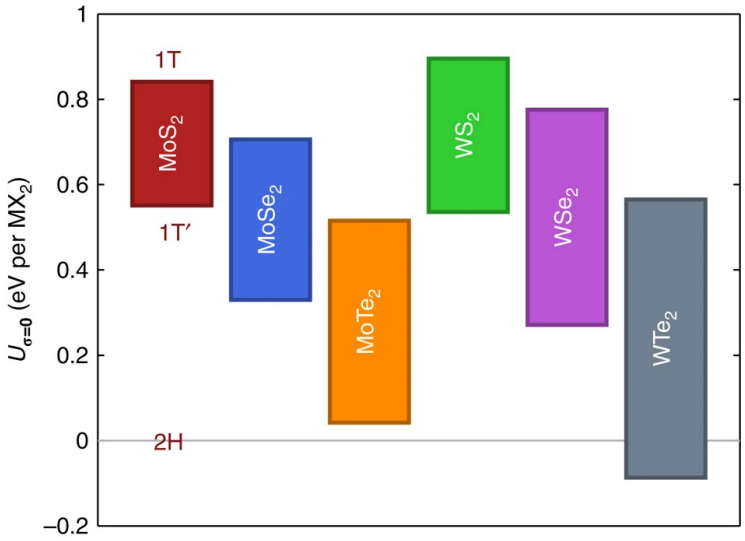

Figure 1.4: Ground-state energy differences between monolayer phases of the six studied materials. The energy U is given per formula unit MX_2 for the $2H$, $1T'$ and $1T$ phases. Its value is computed at the equilibrium (zero stress, σ) lattice parameters for each phase. Because $\sigma = 0$, these values for U are equivalent to the enthalpy H. Vibrational energy is not included in these values. Reproduced from reference[8] with permission from Springer Nature Limited.

1.1.2 Band structure of TMDCs

Most bulk crystals of TMDCs are indirect bandgap materials. Importantly, semiconducting MoS_2 and other group 6 TMDCs become direct bandgap semiconductors when the thickness decreases to a monolayer[10–12]. Here, we discuss the basic features of the band structure of MoS_2, which is the most famous semiconducting TMDC. Results from DFT calculations are shown in Figure 1.5. The critical points are located at K, Q, and Γ points[13].

Note that the Q point is located between K and Γ and was not labeled in the original plot. For bulk MoS_2, the valence band (VB) maximum is located at the Γ point, while there is a local maximum at K. For the conduction band (CB), the global minimum is located at the Q point, while there is a local minimum at the K point. Figure 1.5 (b - d) illustrates the effect of reducing the thickness of the sample. The lowest energy transition is indicated by the black arrows. These calculations clearly show that as the number of layers reduces, the energy of the VB at Γ significantly decreases whereas the energy of the CB at K remains almost intact and at Q significantly increases. Finally, when the material is thinned down to a single layer, the CB minimum shifts from Q to K, and the VB maximum also shifts from Γ to K. Therefore, single layer 2D-TMDCs are direct bandgap semiconductors with the minimum transition energy located at the K point, which is at the corner of the Brillouin zone. Such crossover from an indirect to a direct band gap material manifests as a drastic increase in the PL intensity. As presented in Figure 1.6, the PL emission from the monolayer MoS_2 is more than an order of magnitude stronger than the bilayer MoS_2. Moreover, the fact that the emission peak is blue-shifted as the layer number decreases agrees with the calculated trend.

Recall that monolayer $2H$-MX_2 has the honeycomb lattice structure shown in Figure 1.3, and it has different atoms in the neighbor site. Hence, the nearest neighbor K points are inequivalent in momentum space (see Figure 1.7 (a)), and therefore they are named K and K′. Carriers (electrons or holes) in K and K′ valleys have opposite momentum k and $-k$ due to the broken inversion symmetry, but with the same energy due to the time-reversal

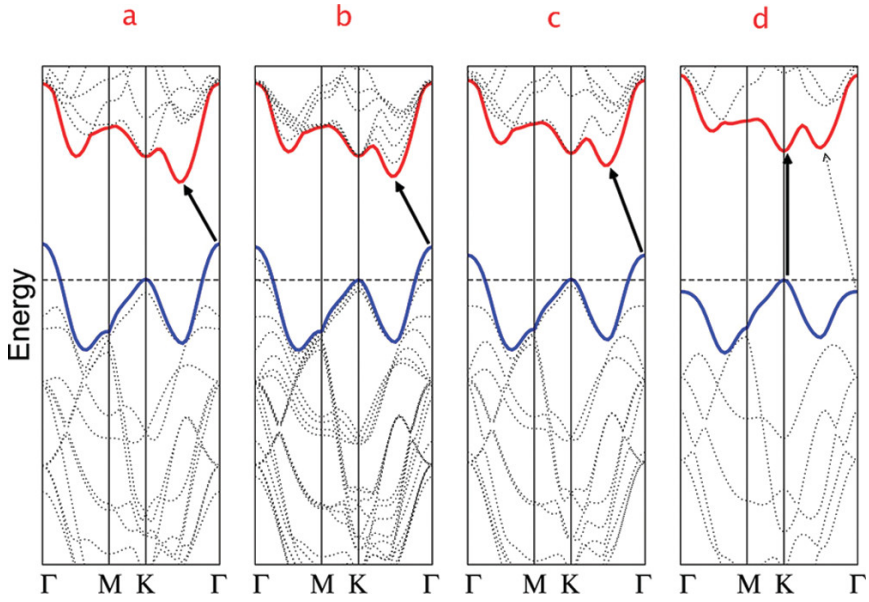

Figure 1.5: Calculated band structures of (a) bulk MoS_2, (b) quadrilayer MoS_2, (c) bilayer MoS_2, and (d) monolayer MoS_2. The solid arrows indicate the lowest energy transitions. Bulk MoS_2 is characterized by an indirect bandgap. The direct excitonic transitions occur at high energies at the K point. With reduced layer thickness, the indirect bandgap becomes larger, while the direct excitonic transition barely changes. For monolayer MoS_2 in d, it becomes a direct bandgap semiconductor. This dramatic change of electronic structure in monolayer MoS_2 can explain the observed jump in monolayer PL efficiency. Reproduced from reference[13] with permission from the American Chemical Society.

symmetry. Therefore, the K and K′ valleys can be taken as pseudospin indices. Valley pseudospin is accompanied by a valley-dependent selection rule for optical excitation with circularly polarized light: interband transition in the K valleys (with momentum k) couples to left circularly polarized light and interband transition in the K′ valleys (with momentum $-k$) couples to the right circularly polarized light[14]. Experimentally, valley polarization in the monolayer of MoS_2 was first reported by three groups in 2012 and 2013[15–17]. They illuminated monolayer $2H$-MoS_2 with right and left-hand circularly polarized light and

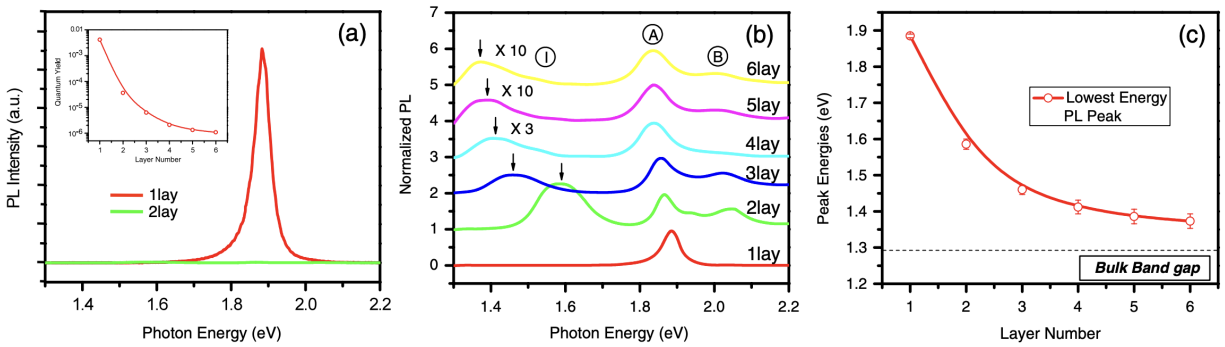

Figure 1.6: PL spectra for mono- and bilayer MoS_2 samples in the photon energy range from 1.3 to 2.2 eV. Inset: PL quantum yield of thin layers for N=1-6. (b) Normalized PL spectra by the intensity of peak A of thin layers of MoS_2 for N=1-6. The spectra are normalized by the intensity of peak A and are displaced for clarity. (c) Band gap energy of thin layers of MoS_2, inferred from the energy of the PL feature for N=2-6 and from the energy of the PL peak A for N=1. The dashed line represents the (indirect) band gap energy of bulk MoS_2. Reproduced from reference[10] with permission from American Physical Society.

detected the degree of polarization of the resulting PL to measure the degree of valley polarization. As expected, a high degree of valley polarization was observed. These experiments suggest a new direction of research with implications in valleytronics on monolayer $2H$-MoS_2 and other 2D-TMDCs. Two parameters, the valley lifetime and the valley exciton coherence time are extremely important in the control of valley polarization. Time-resolved PL and other pump-probe techniques[14], could reveal the dynamics of exciton intervalley coupling[18–20] and other depolarization effects.[19,20] The photo-emission study of these types of materials was the driving force behind the development of our fs-PLup apparatus (see chapter 5)

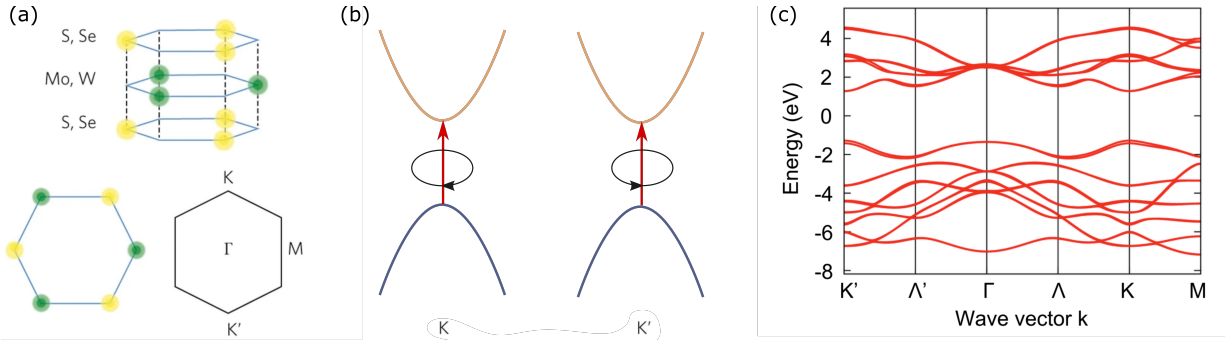

Figure 1.7: Electronic and optical properties of 2D-TMDCs. a, Trigonal prismatic structure of monolayer TMDCs. The honeycomb lattice structure with broken inversion symmetry and the first Brillouin zone with the high-symmetry points are shown. b, Electronic bands around the K and K' points, and the valley-dependent optical selection rules are illustrated. c, Calculated band structures of monolayer MoS_2. The direct band gap is located at K (K′). a, Reproduced from reference[21] with permission from Springer Nature Limited. c, Reproduced from reference[22] with permission from the American Physical Society.

1.2 TMDC materials studied in this thesis

1.2.1 $1T'$ $MoTe_2$

$MoTe_2$ has three stable crystalline phases $2H$, $1T'$ and T_d, as shown in Figure 1.8. These structures have different nuclear configurations, electronic and optical properties. The $2H$ phase has a central symmetric lattice structure and is semiconducting. The $1T$ phase is absent in $MoTe_2$ due to the spontaneous structural distortion that leads to the formation of the $1T'$ phase[7]. The structural difference between $2H$ and $1T'$ phases arises from the spatial arrangement of Te atoms. $1T'$-$MoTe_2$ presents a slight band overlap near the Fermi level, and therefore semimetallic behaviour[23].

$MoTe_2$ is considered to be the most promising TMDC material for phase engineering due

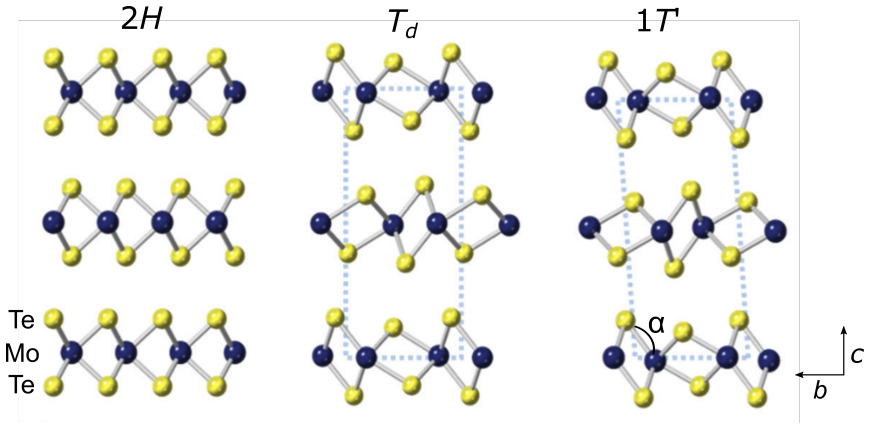

Figure 1.8: Structure of different phases of $MoTe_2$

to the relatively small energy difference ($\Delta E < 50$ meV) between its metallic $1T'$ and its semiconducting $2H$ structures[7,8,24]. To date, the $2H$-to-$1T'$ phase transition in few-layer $MoTe_2$ has been achieved through laser irradiation[25,26], strain engineering[27], electrostatic doping[28], and controlled chemical vapor deposition (CVD) growth[29]. However, it should be noted that the laser-induced $2H$-to-$1T'$ phase transition was achieved under high fluence irradiation conditions for the thickness of $MoTe_2$ to be reduced as a consequence of material ablation[25,26]. Their work indicated that it is hard to accomplish the photoinduced phase transition (PIPT) in this system, and high enough laser power is needed to drive the system to the ablation threshold. Later on, Zhang et. al. reported the discovery of an ultrafast $T_d \rightarrow 1T'$ PIPT of $MoTe_2$ that happens in only ~ 700 fs[1,30]. In this thesis, to better understand the effects of photoexcitation on T_d-$MoTe_2$ we cooperated with groups of Prof. Tsen at the University of Waterloo and Prof. Sun at Key Laboratory of Materials Physics, Chinese Academy of Sciences, and performed tr-bb-TA and tr-bb-TR experiments in thin flakes and a single crystal, respectively (see chapter 3). We have also performed

experiments on the $2H$ phase at increasing incident fluence and have not observed any evidence that could indicate a possible PIPT.

1.2.2 $2H$-SnS_2

Recently, tin disulfide (SnS_2) has attracted much interest because it is recognized as an earth-abundant, relatively cheap, and low-toxic material. Additionally, it has been shown to have high on/off current ratios in field effect transistors[31,32], and have been integrated as an active material in fast[33] and flexible[34] photodetectors, gas sensors[35], and photovoltaic cells[36]. The most common form of SnS_2 is the $2H$ phase. It should be noted that in the literature, SnS_2 with a structure identical to that of $1T$-MoS_2 as shown in Figure 1.3(b) is called $2H$-SnS_2[37–39], which should not be confused with the structure of $2H$-MoS_2 as shown in Figure 1.3(a). Note that such nomenclature doesn't follow the rules mentioned above. In $2H$-SnS_2, M is octahedrally coordinated by sulfur atoms, whereas M in $2H$-MoS_2 possesses trigonal prismatic coordination. Monolayers of $2H$-SnS_2 are stacked exactly on top of one another to form the $2H$-polytype of bulk SnS_2. Unlike most 2D-TMDCs, $2H$-SnS_2 remains an indirect bandgap semiconductor for all thicknesses, with the band gap ranging between 2.18 eV (bulk) and 2.41 eV (monolayer).[40] However, despite the large body of structural and electronic studies carried out in $2H$-SnS_2[38,39,41–43], there is scarce experimental information in regards to its acoustic or elastic properties[44–48]. This is likely due to its low Pugh or B/G ratio that makes $2H$-SnS_2 quite brittle[45]. However, its transparency in the visible-near infrared makes it an ideal candidate to be investigated

by our non-invasive all-optical pump-probe approach (see chapter 4).

1.2.3 MoS_2 and WS_2

Monolayers of group 6 TMDCs have a direct bandgap of $\sim$ 1-2 eV with remarkably strong light-matter interactions, and vdW heterostructures of these semiconducting MX_2 layers are optimal for optoelectronic and light-harvesting applications[49,50]. The calculated DFT band structures of group-6 hetero-bilayers of MoX_2/WX_2 (with X = S, Se) reveal indirect

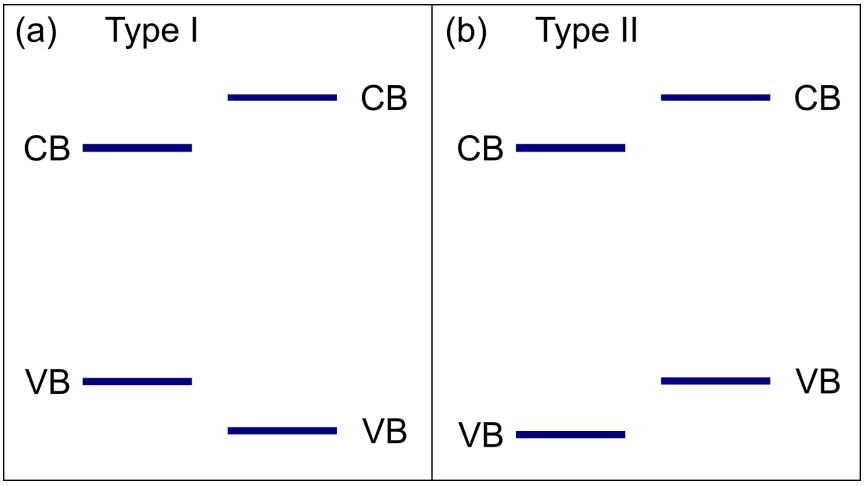

Figure 1.9: Type I (a) and Type II (b) band alignment at the hetero-bilayer interface.

band gaps due to the interaction of the antibonding p_z orbitals from chalcogenide atoms of the composing TMDC monolayers[51]. As a result, the VB maximum is located at the Γ point and the CB minimum is located at the K point. The VB maximum at the K point shows contributions only from d orbitals of W, and the CB minimum at K only from d orbitals of Mo[51]. This leads to a type-II band alignment (see Figure 1.9). The

type-II alignment of TMDC hetero-bilayers means that the absorption of photons in either of the constituent monolayer can lead to the separation of the photo-generated electron and hole. For example, light absorption in MoX_2 leads to the injection of holes into WX_2, and light absorption in WX_2 leads to the injection of electrons into MoX_2[52]. Interesting photoinduced dynamics phenomena have been observed in the type-II aligned TMDC hetero-bilayers, such as the ultrafast charge transfer[53,54] and the formation and relaxation of interlayer excitons[55–57]. Here, we decided to study the MoS_2/WS_2 bilayer system to directly investigate the electron-hole recombination dynamics by fs-PLup (see chapter 5). This work has been carried out in collaboration with the groups of Andrei Vescan (RWTH, Aachen University) and Marika Schleberger (University of Duisburg Essen).

Chapter 2

Methodology

In this chapter, I will introduce the experimental methodology implemented for the study of ultra-thin and bulk TMDCs, and the data analysis protocols. The fundamental timescales of scattering processes in condensed matter vary from fs to picosecond (ps) and can be monitored in real-time by ultrafast spectroscopy. Time-resolved techniques are employed to investigate carrier and phonon relaxation dynamics, excitonic effects, and electron-electron and electron-phonon thermalization processes. In this thesis, we have developed and applied tr-bb-TA, tr-bb-TR and fs-PLup spectroscopies. In addition to these techniques, it has been crucial to developing both sample preparation methods and efficient data analysis strategies. These will be introduced below, and details about specific data analysis protocols can be found in the Appendix A.

2.1 General principle of pump-probe spectroscopy

Pump-probe spectroscopy is one of the most powerful time-domain techniques to investigate ultrafast dynamical phenomena relevant to the fields of physics, chemistry, and biology[58]. In condensed matter, pump-probe techniques are widely used to study not only the dynamics of charges, spins and atoms but also the formation of unusual photo-induced hidden phases and PIPTs. Here, I will briefly describe the pump-probe method and introduce the general processes that are observed following photoexcitation. Various pump-probe schemes have been developed since Abraham and Lemoine pioneered the pump-probe technique in 1899[59]. Nowadays, all-optical pump-probe techniques span over a very broad spectral range (from the infrared to the hard X-ray regime). Here, I will limit the discussion to the most commonly used approach, which is known as tr-fs-transient reflectivity (TR)/transient absorption (TA) spectroscopy.

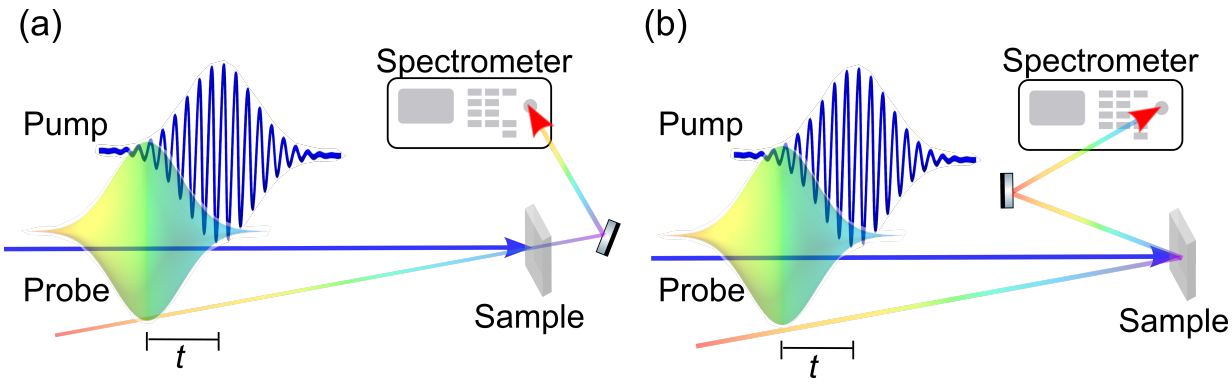

Figure 2.1: A simple illustration of the pump-probe experiment. (a) tr-bb-TA spectroscopy, (b) tr-bb-TR spectroscopy. The pump (blue) induces dynamics in the sample, and the change in transmission/reflection over time is probed by the delayed probe (rainbow).

In pump-probe spectroscopy, a pump pulse excites the sample, and the absorbance or the reflectivity is recorded as a function of time by measuring the transmitted or reflected intensity of a second (probe) pulse. Figure 2.1 shows a simplified depiction of the pump-probe experimental setup. The pump (blue) excites and brings the sample out of equilibrium. Pump-induced changes in the transmission and/or reflection of a time-delayed probe pulse (rainbow) are then recorded as a function of time delay (t). A retro-reflector installed on a linear motorized translation stage is used to control the timing between the pump and probe pulses. Light propagates with a velocity of $\sim 3 \times 10^{10}$ cm s^{-1} in air (or vacuum), which corresponds to ~ 1 mm in 3.3 ps. The temporal resolution of pump-probe spectroscopy is usually determined by the temporal widths of the light pulses, which depend on the laser system and can be less than 100 fs.

If the probe pulses present a broad spectrum or bandwidth, a dispersive spectrometer with a linear array detector could be implemented to record the full spectrum of the probe beam. This variation is referred to as broadband probing to differentiate it from single color approaches. The transient signal corresponds to the difference in the spectrum with and without the presence of the pump. This is obtained as explained below as a function of t and often averaged over several thousand to millions of pairs of pump and probe pulses to improve the signal-to-noise ratio (SNR).

The pump-probe signal in the transient absorption configuration corresponds to the differential absorption ($\Delta A/A$) of the probe beam as a function of t, which can be written

as:

$$\frac{\Delta A(t)}{A} = \frac{A_p(t) - A_0}{A_0} \tag{2.1}$$

Where A_p and A_0 are the absorptions of probe pulse with and without the pump pulse, respectively. In the reflective configuration, Equation 2.1 can be re-written as:

$$\frac{\Delta R(t)}{R} = \frac{R_p(t) - R_0}{R_0} \tag{2.2}$$

To monitor ($\frac{\Delta A}{A}$) or ($\frac{\Delta R}{R}$), the pump pulse is modulated by an optical chopper. The optical chopper is an electro-mechanical instrument that periodically interrupts the pump beam.

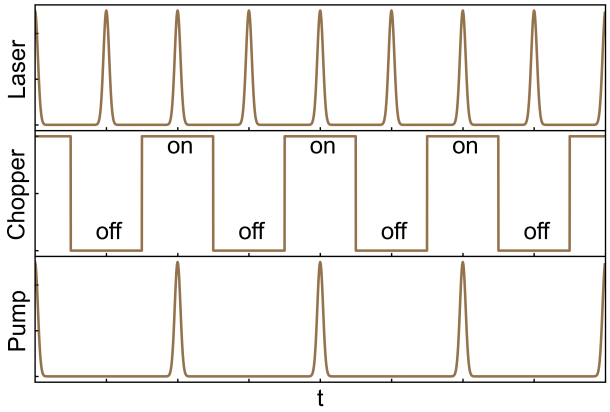

Figure 2.2: An example of pulse modulation in pump-probe spectroscopy. Pulses of lasers before optical choppers (top), the output signal of the optical chopper (middle), and the pump signal after optical chopper (bottom).

Figure 2.2 shows the general working principle of an optical chopper in the limit of one pump pulse per sector. In this case, the frequency of the chopper is selected as half of the

frequency of the laser system. The laser pulse train with high frequency f_1 is shown in the top panel, and the square wave is the output of the chopper and represents the sectors that enable and block the pump transmission, which is synchronized with the laser system and is set to $f_1/2$. Finally, the pump pulse train after the optical chopper is shown at the bottom. Since the probe pulse is monitoring the sample without passing through the optical chopper, we will obtain subsequent probe pulses with pump ($I_{\text{probe+pump}}$) and without pump excitation (I_{probe}). Therefore, we can obtain the differential absorption/reflection ($\frac{\Delta A}{A}$ or $\frac{\Delta R}{R}$) from $I_{\text{probe+pump}}$ and I_{probe} as follows,

$$\frac{\Delta X}{X}(\lambda) = -log(I(\lambda)_{\text{probe+pump}}/I(\lambda)_{\text{probe}}) \tag{2.3}$$

with $X = A$ or R, and therefore I represents the transmitted or reflected intensity, respectively.

Since each pair of pump and probe pulses originate from the same laser pulse, they are well-synchronized and also preserve their relative phase information. The optical chopper, the spectrometer, and the laser system are typically synchronized via a digital delay generator.

Major processes observed in pump-probe measurements

In tr pump-probe techniques, there are three major processes that are often discussed when studying molecular systems in the solution or gas phase, and they are shown in Figure 2.3 for a hypothetical system comprised of five 3-level identical molecules. These processes include excited state absorption (ESA), ground-state bleaching (GSB) and stimulated emission (SE), and they depend on the probed spectral region. Figure 2.3(a) displays

the state of the system at the arrival of the pump pulse. The five molecules are in the ground state (S_0). Figure 2.3(b) illustrates the same ensemble of molecules after excitation by the pump pulse in resonance with S_0 and the first excited state (S_1). In the figure, two of five molecules have been excited. The possible processes that the probe may undergo are illustrated by arrows. When the probe pulse is resonant with the transition from S_1 to the 2$^{\text{nd}}$ excited state (S_2), those molecules in S_1 may absorb light, and therefore lead to a decrease in the transmission of the probe beam, i.e., $\Delta A = A_p - A_0 > 0$; this process is called ESA.

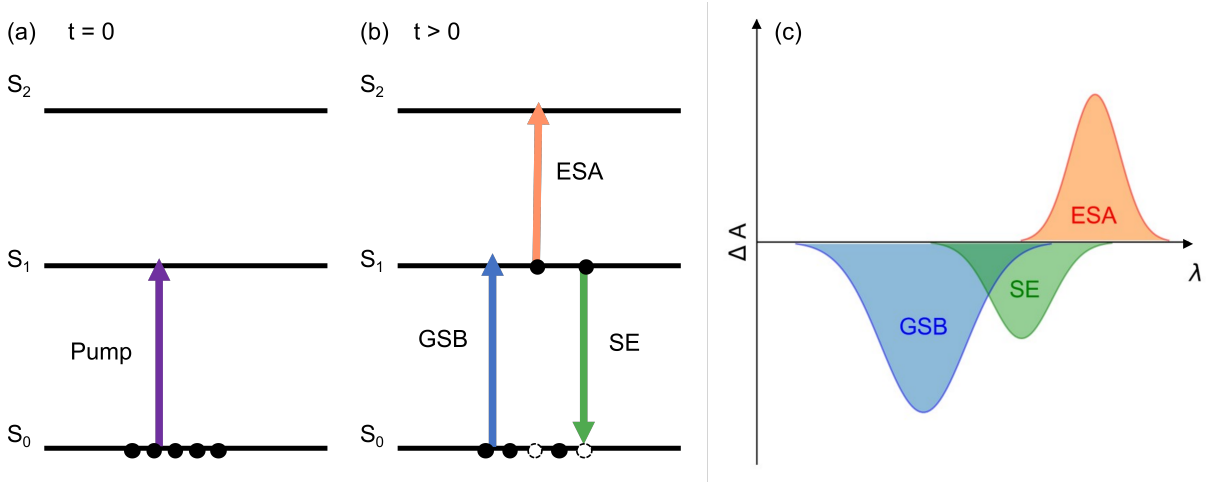

Figure 2.3: The illustration of major dynamical processes (a) The state of the system at the time zero. (b) The origins of the pump-probe signal: GSB, ESA and SE. (c) Both GSB and SE contribute to negative differential absorption signal while the excited-state absorption offers a positive signal.

When the probe wavelength matches the transition from S_0 to S_1, then the probe transmission is enhanced by the reduction in the population of the ground state, i.e., $\Delta A = A_p - A_0 < 0$; this is called GSB. The probe can also stimulate the decay of population from

S_1 to S_0, a process is known as SE. In SE the emitted photons follow the same direction as the probe photons, so the intensity of the probe is enhanced, i.e., $\Delta A = A_p - A_0 < 0$. The above processes are well understood in the study of molecules in the solution or gas phase, where molecular states are well-defined and localized within each molecular entity. In crystalline condensed matter systems, these phenomena are not so well defined since the transitions occur between bands, e.g., the VBs and the CBs, and the electronic wavefunctions are highly delocalized. A brief discussion of the processes in a crystalline condensed matter model system involving two bands is introduced below.

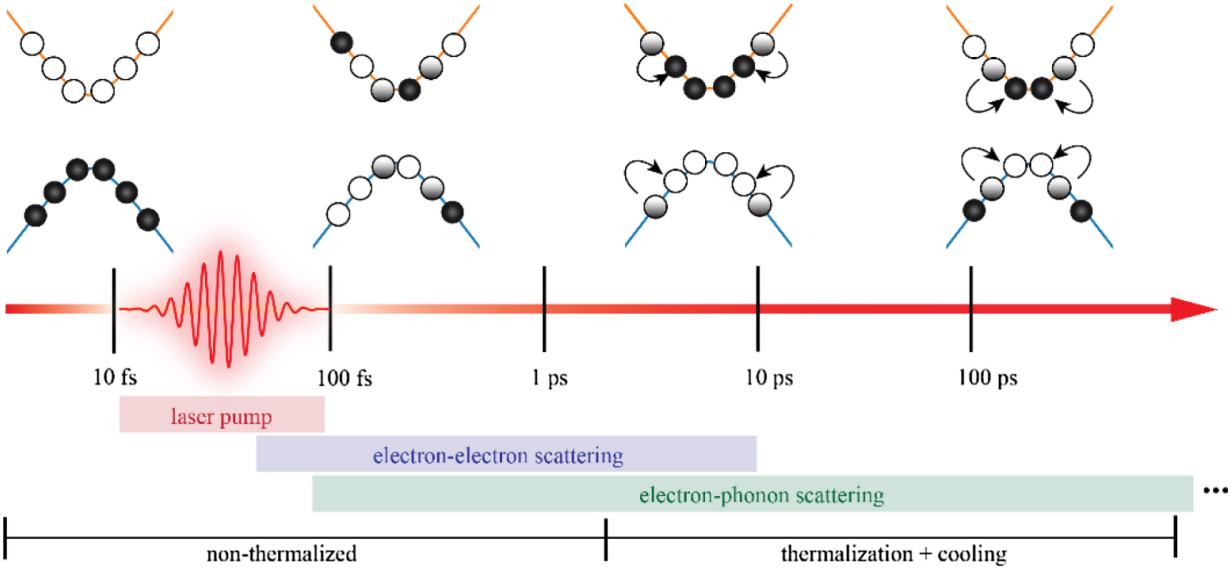

Figure 2.4: Schematics of electron-electron and electron-phonon scattering after laser excitation during a transition to a thermalized regime, and their respective approximate time scales. Reproduced from reference[60] with permission from IOP publishing.

In the Figure 2.4, we show the photon-induced dynamics in the condensed matter. The carrier relaxation after being excited by an ultrafast pulse could be separated into three

temporal overlapping regimes: non-thermal regime, hot carriers regime, and iso-thermal regime[61]. In the non-thermal regime, the carrier distribution is not thermalized and cannot be represented by a Fermi-Dirac distribution with a characteristic electronic temperature (T_e). The investigation of this regime could provide information about processes such as carrier-carrier or exciton-exciton scattering, that bring the non-thermal distribution to a hot thermalized distribution (hot-carrier regime). In the hot-carrier regime, the distribution of carriers could be characterized by Fermi-Dirac distribution, and T_e is usually much higher than the lattice temperature (T_l). Investigation of this hot carrier regime focuses on the rate of cooling of carriers to the lattice temperature and provides information about various carrier-phonon, exciton-phonon, and phonon-phonon scattering processes. At the end of the hot carrier regime, carriers, phonons, and excitons can be described by the same temperature, after which excited electrons and holes recombine[61]. Some specific phenomena that are important in solid-state materials after optical pumping include Pauli blocking/state filling, dynamical bandgap renormalization (BGR)[62], Auger recombination[63], and exciton-exciton annihilation[64].

Here, I will introduce a tr-bb-TA experiment performed in single layer $2H$-MoS_2 as an example about BGR. The BGR effect is due to the many-body interactions of photo-induced carriers affecting the energetics of the material. A strong reduction of the bandgap energy was observed by Pogna et.al.[65], who combined tr-bb-TA measurements with DFT calculations. Their absorption spectrum was characterized by three main peaks of excitonic nature at 1.9, 2.04, and 2.9 eV, the so-called A, B, and C excitons, respectively. Fig-

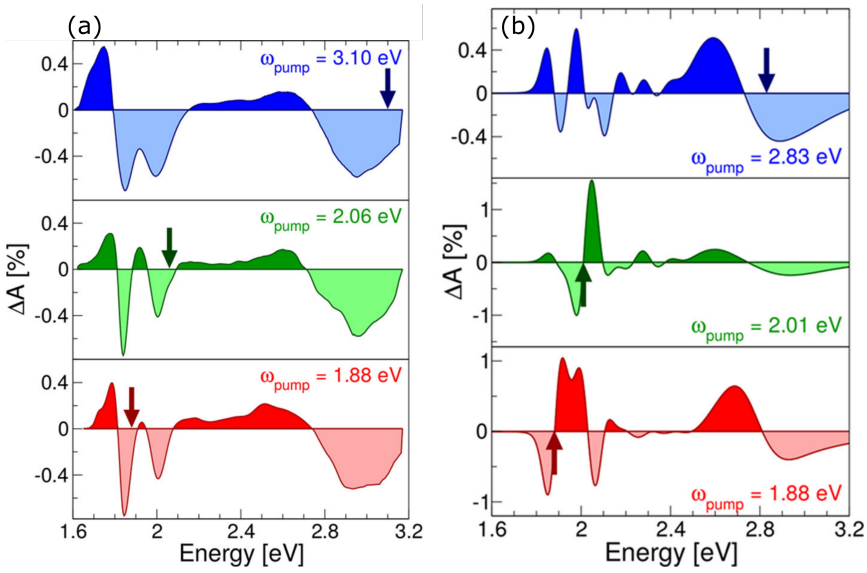

Figure 2.5: TA spectra of 1L-MoS_2 for three pump photon energies, and the pump photo energy is indicated by the arrow in each panel. (a) TA spectra of 1L-MoS_2, recorded at fixed pump-probe delay $t = 300$ fs, for three pump photon energies, i.e., in resonance with the A ($E_{\text{pump}} = 1.88$ eV) and B ($E_{\text{pump}} = 2.06$ eV) excitons, and out of resonance with C ($E_{\text{pump}} = 3.10$ eV). (b) Calculated transient absorption spectra of 1L-MoS_2 for three pump photon energies, i.e., 1.88 eV, 2.01 eV, and 2.83 eV. The first two energies correspond to the excitation of the system in resonance with the A and B excitons; the higher energy is 0.1 eV above the theoretical position of the C peak. The results were obtained by including the effect of the BGR and excitonic binding energies. Reproduced from reference[65] with permission from the American Chemical Society.

ure 2.5(a) presents their TA spectra of monolayer MoS_2 at $t = 300$ fs. Three pump photon energies were selected, which correspond to the A exciton ($E_{\text{pump}} = 1.88$ eV), the B exciton ($E_{\text{pump}} = 2.06$ eV), and off-resonance near the C exciton ($E_{\text{pump}} = 3.10$ eV). Figure 2.5(b) shows the first principle modeling results of the TA spectra for three pump photon energies ($E_{\text{pump}} = 1.88$, 2.01, and 2.83 eV). The calculated TA spectra were obtained by including all the modifications induced by the photoexcited carrier population, i.e., additional screening channel and the charge density variation of excited-state carriers[65]. After con-

sidering these modifications, the calculated result was found in good agreement with the experimental spectra. They estimated an overall band gap shrinkage of the order of a few tens millielectronvolts. Strong electronic renormalization effects are also observed in our tr measurements of 2D-TMDCs (see Figure 3.3 in chapter 3).

Exponential decay model

It is generally assumed that the relaxation process of excited carriers follows exponential decays[66,67]. Depending on the system under study, multiple exponential decays can be included in the fitting function as shown in Equation 2.4.

$$S(t) = u(t) \sum_{i=1}^{n} A_i \exp(-\frac{t}{\tau_i}) \tag{2.4}$$

where $u(t)$ is a unit step function, which is equivalent to 0 for t $<$ 0 and 1 for t $\geq$ 0. A_i are the amplitudes of each temporal component. One can assign many exponential decays to find a well-represented fitting result, and another trick is to conduct Singular Value Decomposition to determine the significant time-dependent components of a multi-dimensional signal. Considering a real $M \times N$ matrix X of observations which may be decomposed as follows:

$$X = USV^T \tag{2.5}$$

Where S is a diagonal matrix (i.e., a matrix where all elements outside the diagonal are zero) of size $m \times n$ containing the singular values, $U(l, ..., m, k)$ contains the traces in the time domain (the left singular vectors), and $V(l, ..., m, k)$ the spectral domain (the right

singular vectors) that correspond to singular value $S(k,k)$[67,68]. The evaluation of temporal data in Spyder is given in section A.3.

Based on the nature of our study and the timescale of the phenomenon under investigation, I implemented different data analysis protocols. For the tr-bb-TA and tr-bb-TR measurements in 2D-TMDCs discussed in this thesis we focus on the study of coherent phonon dynamics, spanning from $t \approx 1$ ps to hundreds of ps. The dynamics right after the photoexcitation will not be analyzed since there is fast electron relaxation decay which complicates the data analysis. The discussion about data processing of tr-bb-TA/TR signals is presented in section 2.3. For this part, it was not necessary to perform a deconvolution to account for this instrumental response function (IRF), which for the most part could have been represented by a Gaussian function with a full width at high maximum (FWHM) of 100 fs.

However, our fs-PLup measurements reveal PL dynamics progressing on the sub-ps timescale, and therefore we needed to account for the instrument response of our fs-PLup setup. Here, I will briefly introduce the deconvolution of a raw transient signal to isolate the response of the sample right after the excitation. The observed tr signal, $I(t)$, is regarded as the convolution between the IRF $R(t)$ and the sample response function $S(t)$:

$$I(t) = \int R(t-t')S(t')dt' \tag{2.6}$$

Suppose the temporal resolution of our instrument is represented by a Gaussian function

with a FWHM of σ:

$$R(t) = A\exp(-\frac{t^2}{2\sigma^2}) \tag{2.7}$$

A single exponential decay with one characteristic lifetime (τ) is shown as an example for clarity. Based on Equation 2.4, a single-exponential decay trace is simulated in Figure 2.6(a).

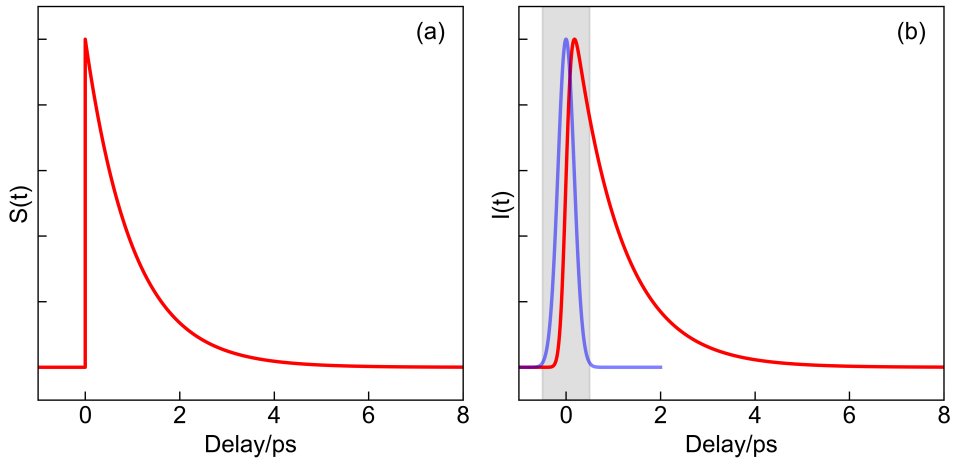

Figure 2.6: The illustration of time traces without (a) and with (b) the convolution with Equation 2.7. Both are related to a single exponential decay and can be simulated from Equation 2.4. The shadow area shows the excitation region and the blue curve represents a laser pulse.

Figure 2.6(b) is the raw transient signal which includes the instrument response limitation and a rising signal due to the excitation by the optical pulse (see the shadow region)[69]. The convolution integral is

$$I(t) = \exp(\frac{\sigma^2}{2\tau^2} - \frac{t}{\tau})(1 - erf(\frac{\sigma^2 - t\tau}{\sqrt{2}\sigma\tau})) \tag{2.8}$$

where *erf* is the error function. When accounting for an amplitude A and an offset I_0 Equation 2.8 becomes,

$$I(t) = I_0 + A\exp(\frac{\sigma^2 - 2t\tau}{2\tau^2})(1 - erf(\frac{\sigma^2 - t\tau}{\sqrt{2}\sigma\tau})) \tag{2.9}$$

A similar equation can be used for multiple exponential decays. After fitting with this model, we obtain the decay constant τ along with the width σ of the Gaussian function. In addition, σ could be obtained by auto-correlation or cross-correlation methods as explained later in section 5.2 of chapter 5.

2.2 Femtosecond transient absorption/reflectivity

The working principle of the pump-probe technique and the major processes following optical excitation were introduced in section 2.1. In this section, I will provide more technical details about our homemade tr-bb-TA/TR spectroscopic setup. Our instrument employs supercontinuum probe pulses that provide a detectable wavelength range of about 540 nm to 950 nm, which covers the resonance region of excitons, bi-excitons, and trions in many semiconducting 2D-TMDCs[64,70–73].

2.2.1 Transient absorption/reflectivity setup

The schematics in Figure 2.7 shows the basic principle of the quasi-collinear TA instrument in our lab. A laser pump beam with a relatively higher intensity and larger spot size than the probe beam excites the sample. A broadband or supercontinuum white light (WL) probe pulse is utilized to monitor the photoinduced changes introduced by the pump pulse. In a quasi-collinear configuration as seen in Figure 2.7, there is a small angle $\sim 10°$ between pump and probe. After the sample, the pump beam is blocked to avoid safety issues. The probe beam passes through the sample and is finally collected by a convergent lens and sent into a dispersive spectrometer.

Our laser system is from Light Conversion, model Pharos SP and delivers a maximum average power of 6 W and maximum pulse energy of 1 mJ in pulses of ~ 170 fs in length and centered at the fundamental wavelength of 1030 nm ($E = 1.2$ eV). The maximum repetition rate of our system is 200 kHz and tr-bb-TA/TR experiments were performed, depending on the studied sample, between 1 kHz and 20 kHz. The initial 1030 nm beam splits into two beams. A beam carrying out 200 μJ of 1030 nm is sent to the optical table. Most of this portion is used as the gate in our fs-PLup instrument (details in subsection 2.5.3), and a small portion is used to generate the WL probe beam for our tr-bb-TA/TR setup (see Figure 2.8). The remaining portion energizes an optical parametric amplifier (OPA) system. Our OPA (ORPHEUS, Light Conversion) is followed by nonlinear systems LYRA I and LYRA II (for differential frequency generation, second harmonic generation (SHG) and fourth harmonic generation) to extend the wavelength range of the output beam from

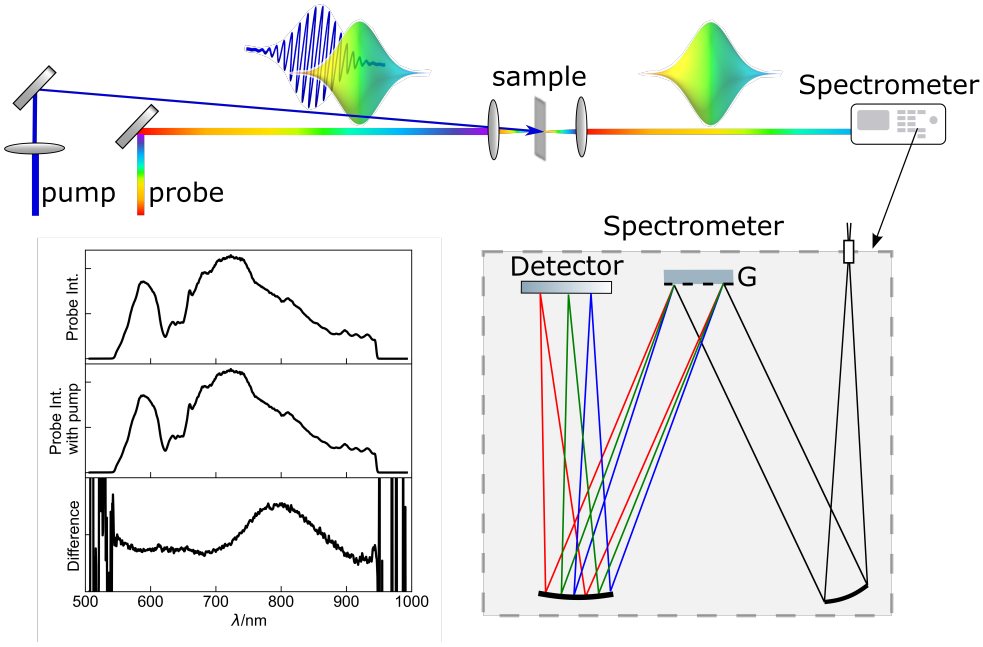

Figure 2.7: A schematic showing the principle of quasi-collinear transient absorption spectroscopy. The top part indicates the pump and probe beams paths which are quasi-collinear. Both are focused into a sample, and the probe beam passes through it and is detected by a spectrometer. The bottom part shows the working principle of a spectrometer where an optical diffraction grating is utilized to divide the supercontinuum light into quasi-monochromatic light with different wavelengths. The light is then detected by a charge coupled device (CCD) inside the spectrometer.

250 nm to 4700 mn. The output of this OPA system is used as the pump beam in our fs-PLup and tr-bb-TA/TR measurements.

The duration of pulses from the OPA system is in the range of $\sim$ 100-200 fs depending on the selected wavelength. The choice of pump photon energy depends on the sample under study, and owing to our completely automated OPA, we can easily vary the pump wavelength with the PC and mount the required mirrors(s) (frequency separator(s)) at the exit of the LYRA(s) unit(s). As shown in Figure 2.8, the pump beam intensity is

tuned by a linear variable filter (VF) to obtain different incident pump fluences, followed by modulation via an optical chopper. Besides using the variable filter, the incident pump fluence could also be varied through the combination of a half-wave plate and a polarizer. This configuration offers precise control of the pump intensity. As for the probe pulse, a small portion of the 200 μJ of the 1030 nm beam ($\sim$ 10 μJ) transits the delay stage and a continuously variable filter to reduce the intensity of 1030 nm to the required level for WL generation. The 1030 nm beam is focused onto a sapphire or Yttrium aluminum garnet (YAG) crystal with a thickness of 3 mm to generate WL, which has a wavelength region from $\sim$ 540 nm to $\sim$ 950 nm. Experimentally, $\sim$ 0.5 - 1 μJ of 1030 nm is used to generate a stable WL probe in our setup. After the sapphire or YAG crystal, the WL probe beam is collimated by a 90°-off-axis parabolic (OAP) mirror. The actual spectra range of supercontinuum WL is wider than $\sim$ 540 nm - $\sim$ 950 nm; however, several short-pass filters are used to block the residual 1030 nm beam, which follows the sample probe samples, and therefore should hit the sample and reach the spectrometer. Just before the sample two metallic mirrors direct the pump and WL probe beam to the sample and are used to optimize the spatial overlap between these two beams. As shown in Figure 2.7, these two mirrors are set relatively far from the sample to provide a quasi-collinear layout. The two quasi-collinear beams are then focused onto the sample. The probe pulse is focused with a short focal length lens that confers $\sim$ tens of μm in FWHM, and the pump pulse is focused with a longer focal length lens, which gives $\sim$ hundreds of μm in FWHM. The transmitted pump beam is blocked immediately after the sample, while the transmitted or reflected WL probe beam is collected by a 50 mm focal lens and sent into a dispersive spectrometer.

Differential tr-bb-TA/TR spectra are obtained by modulating the pump beam with a mechanical chopper operating at a specific frequency (half of the acquisition frequency). An optical delay stage is used to control the time delay between pump and probe pulses. The tr-bb-TA/TR spectra are recorded using a synchronized dispersive spectrometer.

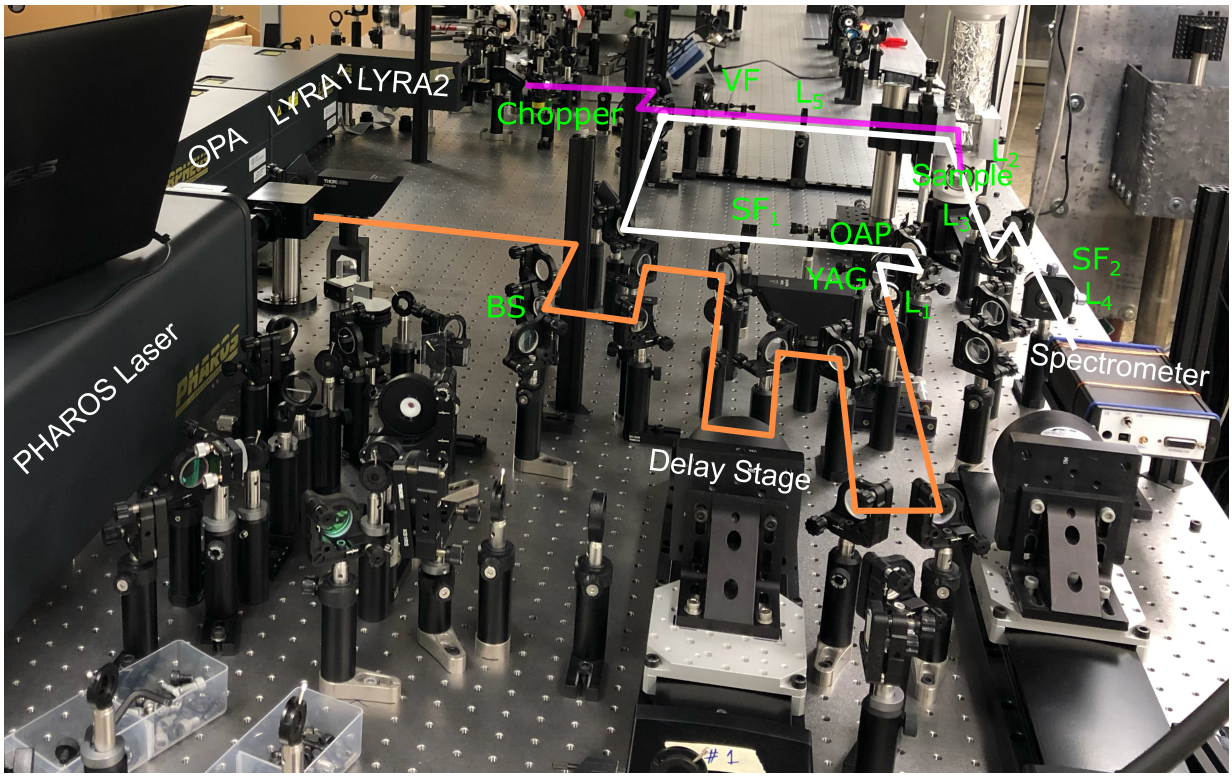

Figure 2.8: The photograph of the spectra- and time-resolved transient absorption spectroscopy setup at UeIL. BS: beam splitter, L: lens, SF: shortpass filter, and VF: variable beam filter. 1030 nm pulse (orange), supercontinuum WL (white), and pump beam (purple).

2.2.2 Time-resolved signal

The tr-bb-TA/tr-bb-TR measurements proceed as follows: the time delay (stage position) between the pump and probe pulses is fixed duration data collection. As shown in Figure 2.2, the optical chopper modulates the pump beam such that the detector collects the intensity of the probe pulses in the presence and in the absence of sample photoexcitation, $I(\lambda)_{\text{probe+pump}}$ and $I(\lambda)_{\text{probe}}$, respectively. The readout of the spectrometer is therefore synchronized with the 'on' and 'off' sectors shown in Figure 2.2. Here, the PC stores the $I(\lambda)_{\text{probe+pump}}$ and $I(\lambda)_{\text{probe}}$ spectra for further analysis. Then the differential absorption signal is obtained according to Equation 2.3. This process is repeated at varying time delays following selected stage positions. Note that normally 10^3-10^4 sectors per time point will be averaged to improve the SNR. Equation 2.3 is helpful for conducting data analysis, and the python script used for analysing tr-bb-TA and tr-bb-TR data is included in section A.1. Note that during real-time data collection, the spectrometer could not tell us which spectrum is the probe without a pump signal and which one is the probe with a pump signal. To determine the sign of transient signal we usually use the small leakage of pump pulse that enters the spectrometer. The pump leakage is also used to adjust the phase of the chopper to warrant proper synchronization. The phase of the optical chopper is adjusted via the chopper controller. The laser, the chopper, and the spectrometer are synchronized via an electronic delay generator.

Chirp correction

The collected supercontinuum WL probe carries a significant positive chirp owing to the

dispersive optical components in the beam path, such as the filter for the residual 1030 nm and the fused silica (FS) lens used to focus the beam onto the sample. As a result, different probe wavelengths λ will arrive at slightly different times with respect to the arrival of the pump pulse as shown in Figure 2.9(a). The amount of chirp (λ) is proportional to the thickness of the dispersive material in the beam path, the group velocity dispersion (λ), and the spectral bandwidth. Therefore, one should avoid adding dispersive materials to the optical path. If not excessive, the chirp could be corrected via a second-order polynomial function $t_{\text{corr}} = a + b\,t_0 + c\,t_0^2$ as the parabola shown in Figure 2.9. Figure 2.9(b) shows a tr-bb-TA spectra after chirp correction.

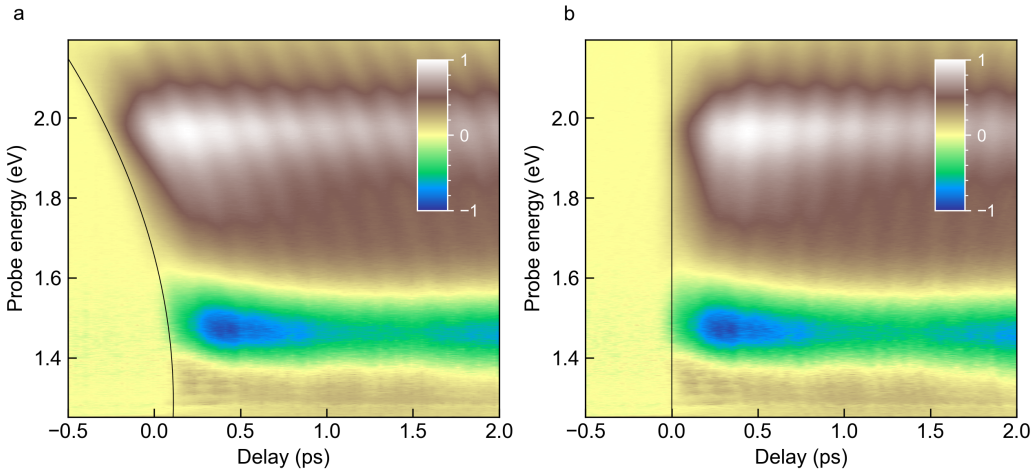

Figure 2.9: Chirp correction procedure. (a) Raw tr-bb-TA spectra of 40-nm thick T_d-$MoTe_2$ flake at 74 K. (b) Chirp-corrected tr-bb-TA spectra. The broadband probe pulses carry positive chirp since they transverse some dispersive materials (e.g. lenses, cryostat window, etc.) before reaching the specimen. The chirp was corrected by fitting a polynomial to the TA-signal onset and time-shifting each probe energy cross section to match the same origin or time zero. The thin solid black lines represent the time-zero curve before a and after b chirp correction.

2.3 Analysis of coherent phonons

Raman spectroscopy is a powerful characterization tool that can be used to determine Raman-active vibrational modes of molecules in solution as well as solid-state materials[74,75]. Although there exist THz-Raman systems[76], most Raman spectrometers are designed to detect molecular/phonon frequencies > 150 cm^{-1}. In contrast, time-domain methods are best suited to detect low-frequency phonon modes. Tr-bb-TA/tr-bb-TR techniques can be applied to investigate not only hot carrier relaxation processes but also the dynamical behaviour of coherent phonons[77,78]. The raw transient data may contain different phonon modes. It is, therefore, crucial to be able to separate each component and there are different methods to attain this goal[79].

Removal of the dynamic electronic background. The first step in the analysis of vibrational coherences is to remove the dynamic electronic background. Different fitting procedures were carried out to remove the dynamic background signal arising from carrier relaxation processes from the tr-bb-TA and tr-bb-TR time traces in our studies of bulk and thin flakes of $MoTe_2$ (see section 3.1 and section 3.2). We generated residuals for the analysis of coherent phonons. To avoid arbitrariness and enable the automation and the analyses of large data sets, we decided to fit temporal traces by an exponential or a linear trend for time delays, $t > 1.5$ ps. Figure 2.10 illustrates the removal of the electronic background from a typical time trace obtained from the tr-bb-TA spectrum of a thin $MoTe_2$ flake. For t > 1.5 ps electronic-driven changes of the TA signal have reached a quasi-steady state and time-dependent modulations are mostly governed by coherent phonon

oscillations. Both fitting functions delivered very similar results, and the fitting results obtained with these two functions and their respective residuals are shown in Figure 2.10.

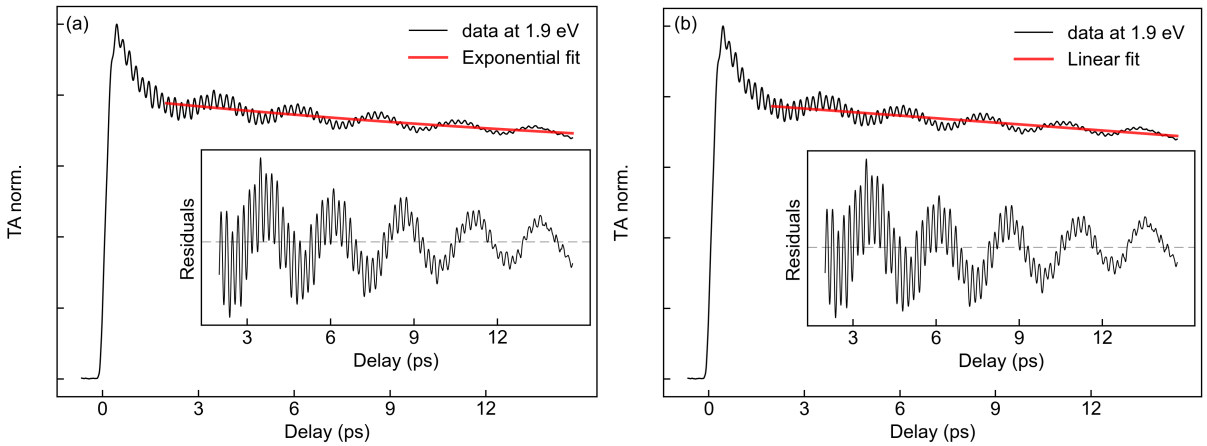

Figure 2.10: Examples of an automated fitting procedure via (a) exponential, and (b) linear functions. A time trace (black) at $E_{\text{probe}} = 1.9$ eV is fitted within the time delay interval t = +2 ps − +14 ps. The result from the fitting is in red. Sample, 40-nm thick T_d-$MoTe_2$; temperature = 74 K. The residual trance is shown in the inset.

Figure 2.11 shows a series of data processing protocols that can be applied to extract information from a typical tr-bb-TA measurement in thin film $MoTe_2$. A Fourier spectrum could be computationally generated via a conventional FFT of the residuals. In order to better visualize the Fourier spectrum, zero-padding can be applied, which relies on appending zeros to the end of the input signal. Zero padding allows one to produce a longer FFT vector which has more frequency bins. This results in a smoother-looking spectrum and provides more accurate amplitude values of resolvable frequency components, but will not improve the frequency resolution.[80] The python script for FFT is included in the

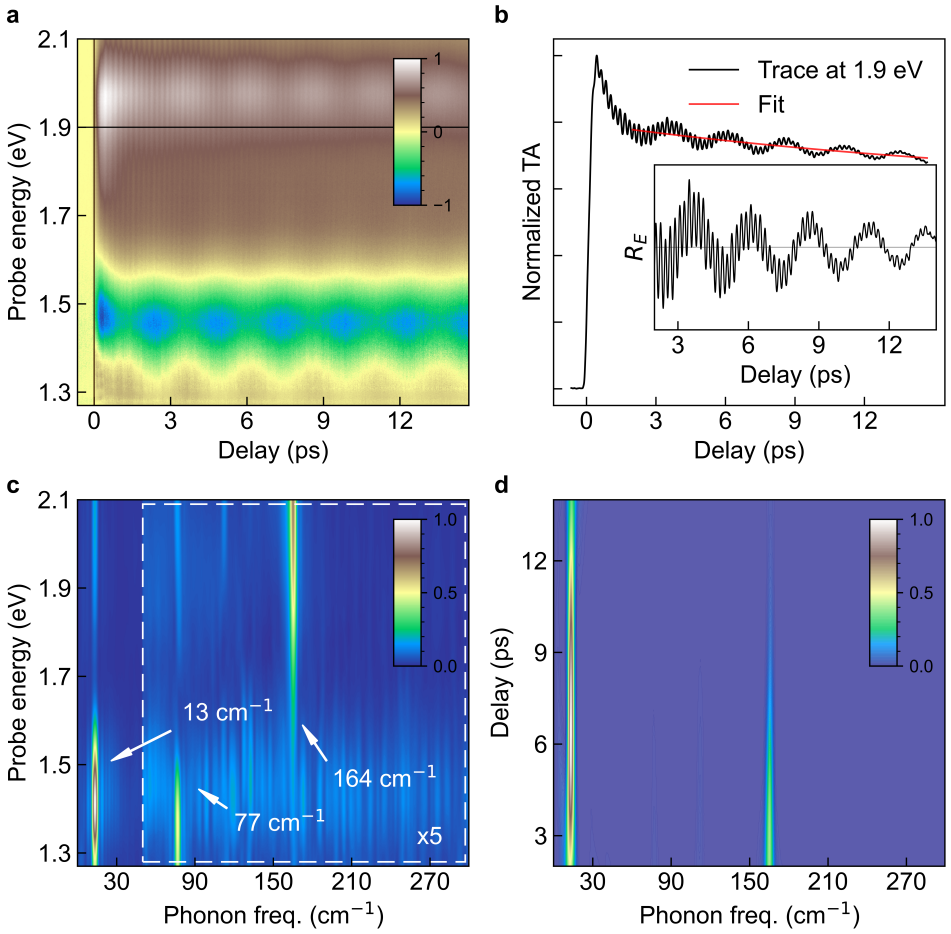

Figure 2.11: Example of data analysis scheme implemented in the photoinduced interlayer phenomena study of a 40-nm thick T_d-$MoTe_2$ flake at 74 K by tr-bb-TA. (a) Chirp-corrected tr-bb-TA spectra recorded as a function of time delay (delay or t). The vertical solid line depicts time zero. Higher and lower frequency coherent phonon oscillations are observable well beyond the noise floor. (b) Black, temporal trace or slice at $E_{\text{probe}} = 1.9$ eV (horizontal black line in panel a); red, exponential fit performed within the interval t = +2 - +14 ps. Inset: residual, R_E, obtained after removal of the electronic background, i.e. difference between black and red traces. (c) Fourier power spectrum via fast Fourier transforms (FFTs) of the vibrational coherences. The most intense modes of T_d-$MoTe_2$ found in this work are indicated by arrows. Data within the dashed rectangle has been rescaled by $\times 5$ for clarity. (d) Computing a short-time Fourier transform (STFT) of the signal averaged for $E_{\text{probe}} = 1.9$ - 2.1 eV, we are able to construct a spectrogram for 74 K.

appendix section A.2. However, a conventional FFT of a residual time trace at given λ will miss time-dependent information. Therefore, we use different methods to decode the raw signal. In the insert plot of Figure 2.10 there are multiple oscillatory components. The aim is to separate these frequency components and explore their time dependency. Besides separating each coherent vibrational mode, it is also important to monitor the amplitude of coherent phonons as a function of the probe photon energy (E_{probe}) or λ and t. The plot of Fourier amplitude(s) as a function of t is called 'spectrogram' and is calculated through STFT. STFT applies a moving temporal window to conduct Fourier transforms (FTs) by segments. The plot of Fourier amplitudes as a function of E_{probe} is known as 'Fourier Power Spectra'. In regards to separating frequency components, we mainly utilized continuous wavelet transform (CWT) analysis. CWT enables the separation of time-dependent frequency components in bins that are related to the temporal width of a 'continuous' function of the frequency and time called the wavelet.[81]. More details about the spectrogram and CWT approaches will be discussed below.

Spectrogram

STFT is an extension of the FT which is based on a sequence of FTs of a windowed signal. The discrete FT of a signal can be calculated by[82]:

$$X_k = \sum_{n=0}^{N-1} x_n \cdot e^{-2i\pi nk/N} \tag{2.10}$$

where x_n is the current sample of a time-dependent residual (at a given E_{probe}), X_k is the Fourier transformed signal in the frequency domain, N is the number of samples (the

length of a time-dependent residual), n is the current sample ($n = 0, 1, ..., N$), and k is the current frequency ($k = 0, 1, ..., N-1$). STFT provides time-localized frequency information for time-varying signal frequency components, while standard FT provides frequency information averaged over the entire signal time interval. The discrete-time STFT is given by[82]:

$$X(m, \omega) = \sum_{n=-\infty}^{\infty} x(n)\, W(n-m)\, e^{-i\omega n} \tag{2.11}$$

where $x(n)$ is the time-dependent signal which corresponds to R_E in our situation, m and ω are two variables, time and frequency, for the STFT of $x(n)$, and W is a window function (here we use a Hamming window). The magnitude squared of the STFT results in the spectrogram. In the STFT, a narrow-width window results in a better time resolution but generates a poor resolution in the frequency domain and vice versa. However, the CWT overcomes this limitation of the STFT.

Continuous wavelet transform

While the FT creates a representation of the time-dependent signal in the frequency domain, the wavelet transform creates a representation of the signal in both the time and frequency domains, thereby allowing efficient access of localized information about the signal. To assess the validity of our data analysis protocol we performed a rigorous test using a dummy signal that mimics the time-dependent oscillatory behavior of the major spectroscopic features observed in our study of thin film $MoTe_2$ samples. As expected, the key requirement for the analysis procedure is its ability to recover the inherent properties of the original components, which in our case are the frequencies of the phonon modes

and their damping characteristics. Thus, the CWT was selected as a well-known powerful mathematical tool suitable for the analysis of time-varying spectral components[83]. Figure 2.12 demonstrates the main steps implemented in this test.

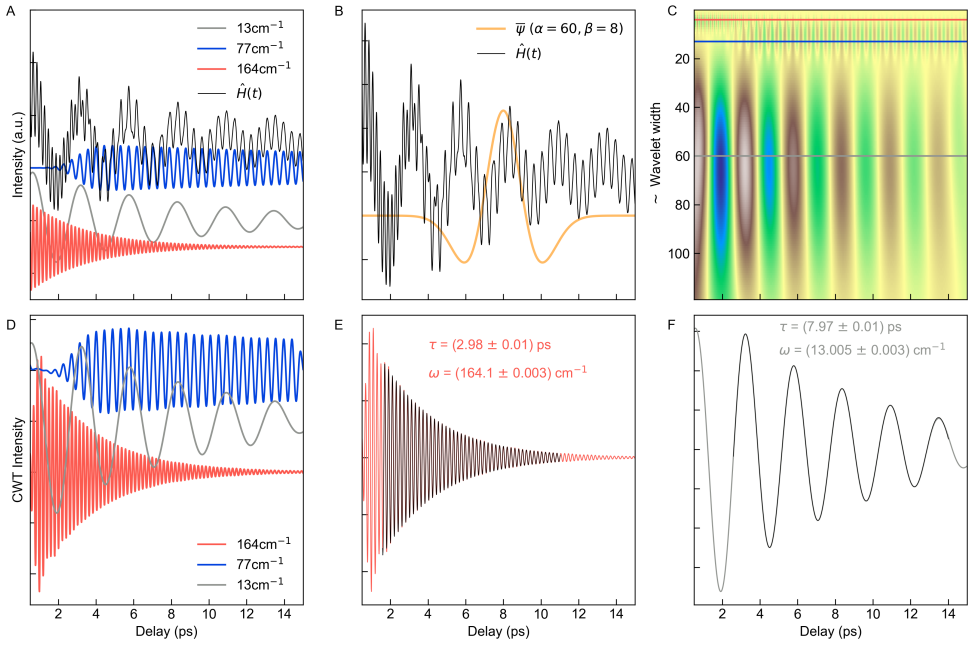

Figure 2.12: Continuous wavelet transform analysis. (A) Dummy signal, $\widehat{H}$(t), constructed to imitate three major spectroscopic features found in our tr-bb-TA data. Red: 164-cm^{-1} phonon mode with 3-ps dumping time; Gray: 13-cm^{-1} phonon mode with 8-ps dumping time; Blue: 77-cm^{-1} phonon mode with abrupt rise and slow damping time constant. Random noise was added to the dummy signal for a more realistic representation. (B) Enlarged view of dummy signal (black) overlaid with the Ricker function (orange) used as the mother wavelet in CWT. (C) A colour map generated from CWT output for various values of scale (α) and position (β) parameters. Red, blue, and grey horizontal lines represent cross-sections for the spectral components of interest. (D-F) Recovered major signal components from selected slices in C. The frequencies and time constants are closely matching those of the original spectral components despite the added random noise and artifacts (edge effects, signal leakage) inherent of the CWT method.

The dummy signal consisted of three constituents with the frequencies of 13 cm^{-1}, 77 $^{-1}$

and 164 $^{-1}$ found in our $MoTe_2$ samples. Damping times of 3 ps and 8 ps for the first two signals were chosen arbitrarily as well as the abrupt rise time for the third signal to investigate a possible fast change in the oscillatory behavior. As a last touch, random noise was added to render a more realistic model signal. The dummy signal generation step is illustrated in Figure 2.12(A). The shape of the Ricker function used as the mother wavelet in our CWT is depicted in Figure 2.12(B). A 2D array of spectral values, shown as a colormap in Figure 2.12(C), is obtained by computing CWT over the grid defined by scale (α) and position (β) parameters

$$X_{\mathrm{w}}(\alpha,\beta) = \frac{1}{|\alpha|^2}\int x(t)\phi^*(\frac{t-\beta}{\alpha})dt \tag{2.12}$$

where X_{w} is the CWT of the input signal in the time domain, $x(t)$, and ϕ^* is the complex conjugate of the mother wavelet. Unique constituents, outlined by red, blue, and grey cross-section lines in Figure 2.12(C) were selected by carefully inspecting the 2D CWT pattern. The data series obtained is directly related to the original spectral components in the dummy signal. The exact frequencies of the recovered signals can be evaluated with the FFT. Moreover, the symmetry and the magnitude of the frequency peak profile from FFT can be used to determine the best position (α value) for the cross-section (frequency) of interest. Separating components with similar frequencies can be tricky as CWT tempts to blend those. To a good degree of success, the "leakage" issue can be solved by applying a bandpass filter, e.g. the Butterworth filter or performing several recurring CWTs.

The recovered signals are shown in Figure 2.12(E,F). Note that despite known edge arti-

facts, which tend to reduce the CWT amplitude (at t = 0 ps and +15 ps in this case); in general, there is an excellent agreement between the corresponding parameters of modelled and recovered constituents, which gives a fair amount of confidence in the selected strategy to analyze our tr-bb-TA/tr-bb-TR data.

Besides using these methods, more direct fitting procedures applied to the raw time traces were found sufficient for the interpretation of tr-bb-TR data in some situations. For instance, we implemented a conventional fitting method when analyzing our SnS_2 data in order to get the frequency arising from a CAW (see subsection 4.2.1). In this case, there is only one frequency value for a given E_{probe} or λ. The fitting function of a transient signal is given below:

$$S(t) = \sum_{i=1}^{2} A_i \exp(-\frac{t}{\tau_i}) + A_f \exp(-\frac{t}{\tau_f}) \sin(2\,\pi f\, t + \varphi) + C \tag{2.13}$$

where A_i and A_f are amplitudes, τ_i and τ_f are time constants, f and φ are the frequency and the phase shift of oscillatory component, and C is an offset. Note that from similar fitting procedures to Equation 2.13 one can obtain the phase shift for a vibrational coherence.

2.4 Pump-probe measurements at low temperature

Solid-state crystalline materials may present thermally driven phase transitions that can lead to different states with distinct physical properties[15,84,85] Therefore, the ability to control the base temperature has been critical, in particular for our study of coherent

phonon dynamics in $MoTe_2$. We would like to thank Professor David Cory (U. Waterloo) for lending us the Oxford cryostat which was coupled to our pump-probe setup and applied on several occasions. The Oxford cryostat is shown in Figure 2.13, and here I will discuss some details related to the operation of this cryostat duringtr-bb-TA and tr-bb-TR measurements at low temperature.

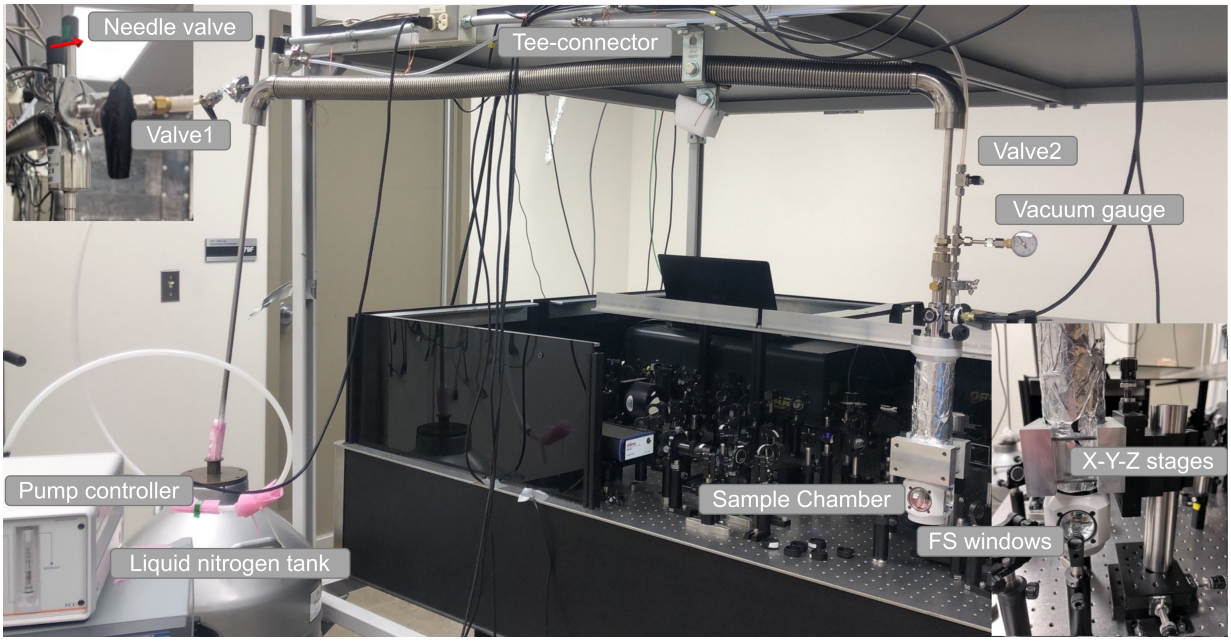

Figure 2.13: Low temperature measurement setup at UeIL. The red arrow in the top left insert indicates that the needle valve should be fully open when the green label on it faces the same direction as the red arrow.

The general steps when measuring ultrafast dynamics at low temperature are listed below:

1. **Mounting of the sample.** The sample chamber is surrounded by four FS windows which allow optical access. To mount the sample, remove one of these windows. Secure to sample to the cold finger using by a metallic holder frame with four screws. These

screws should be mildly tightened to avoid the rapture of the sample (or substrate) when the temperature goes down owing to thermal compression. Finally, after mounting the sample, place back the FS window. Each window seals against the body of the cryostat through the use of rubber o-rings.

2. **Set Vacuum environment.** Connect the vacuum line to the T connector and open valve 2. Wait $\sim$ 30 minutes for vacuum to build up and check the vacuum level through the vacuum gauge. Then close value 2 and remove the vacuum line from the T connector.

3. **Remove moisture inside the pump system.** Connect the nitrogen gas line to valve 1 and open it to let the nitrogen gas pass through the long needle value to the liquid nitrogen tank. Wait $\sim$ 15 minutes. Close the needle valve and valve 1, then remove the nitrogen gas line.

4. **Filling of the liquid nitrogen tank and switching on the pump.** Fill the tank with liquid nitrogen. Adjust the pump flow on the pump controller and open the needle valve. Set temperature on the temperature controller. Wait until the system temperature reaches the setting point.

Note that the flow rate can be controlled by the pump controller and the needle valve. Normally, adjusting the needle value could help the system to reach stable conditions when the temperature fluctuates a lot. The temperature controller is based on a proportional-integral-derivative (PID) controller which provides great temperature stability of $\pm$ 0.01 K. Since the sample is attached to the cold finger of the cryostat, the signal will be sensitive to the sample motion caused by the contraction or expansion of the cold finger arm upon

cooling or warming, respectively. In addition, any gas line attached to the system should be removed to avoid sources of vibration. Once, stable temperature conditions are attained, the sample position is adjusted via an X-Y-Z stage that holds the cryostat in position.

2.5 Time-resolved photoluminescence measurements

Instead of using a probe pulse to monitor the photoinduced changes introduced by the pump, one could also monitor the emitted light or PL signal that originates from the radiative decay of photoexcited electrons (or electron-hole pair recombination in solid-state materials). Therefore, tr fluorescence spectroscopy is also widely employed to understand the photoinduced dynamics of hot carriers and the recombination mechanisms in semiconductors 2D-TMDCs. For time-resolved photoluminescence (tr-PL), there are several famous techniques.

The most common approach is based on the use of ultrafast streak cameras. A pulsed beam photoexcites the sample and the subsequent fluorescence is monitored as a function of time after excitation. The streak camera is an electronic device that transforms the intensity of temporal light into a spatial profile of electrons on the detector. In Figure 2.14, its working principle is presented schematically.[86] The photocathode converts the incoming stream of photons (PL signal) into photoelectrons, and the photoelectrons are accelerated by a high-voltage before entering the deflection system. Then electrons are deflected by the time-varying high voltage between two plates. Finally, the electron beam hits on a phosphor screen and produces emitting trace on the screen, which can be recorded, e.g., by

a CCD detector. Here, the tr signal is converted into a spatial dependent signal along the sweeping axis. The type of photocathode used in a streak camera determines its spectral range. The typical time resolution of optoelectronic streak cameras is a few of ps. The time resolution for the fastest instruments can be as low as 200 fs. However, to achieve such great time resolution the streak camera should work in single-shot mode, and thus requires a high light intensity at the device input. In repetition mode, the time resolution is > 1 ps which is limited by trigger jitters of the control electronics.[87] As a result, the single-shot mode with such high time resolution is most beneficial for materials with a high emission efficiency. For semiconducting 2D-TMDCs, the quantum yield of PL is typically low and less than 10%[10,88,89], so it is difficult to record their tr-PL with a streak camera via single-shot mode.

Fluorescence lifetimes related to the recombination of electron-hole pairs across the semiconductor bandgap and or from trapped states typically occur in timescales ranging from several hundreds of fs to nanosecond (ns)[14]. Therefore, the development of other tr-PL techniques that can overcome the limited time resolution offered by streak cameras is critical to monitoring ultrafast (sub-ps) light emitting processes. Femtosecond optical Kerr effect (OKE) and PL up-conversion are powerful techniques applied in biology and chemistry to monitor the ultrafast fluorescence dynamics with a time resolution of a couple of hundreds of fs[90,91]. We developed and implemented both approaches and found out that PL up-conversion is more sensitive than OKE for the study of monolayer and bilayer TMDCs. These techniques are introduced below tr-PL in subsection 2.5.1 and subsection 2.5.2 and

some preliminary results obtained by PL up-conversion are shown in section 5.2.

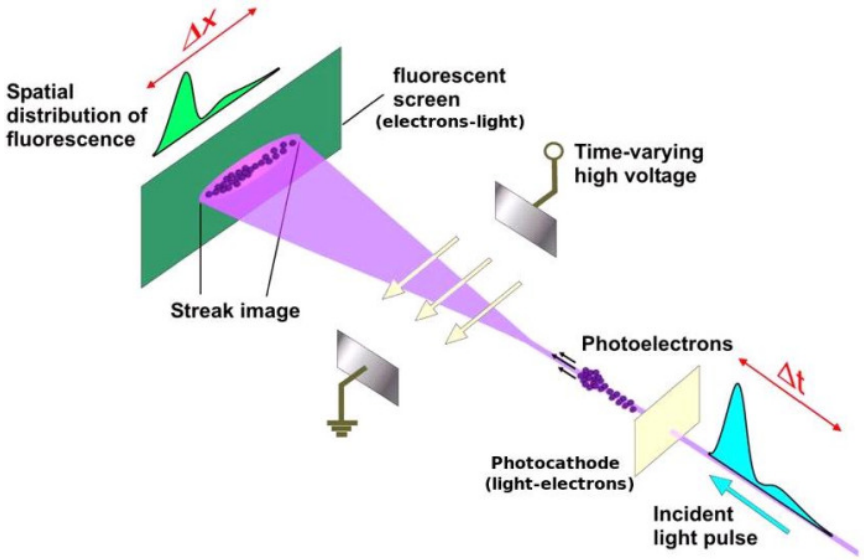

Figure 2.14: The working principle of the streak camera. Reproduced from reference[86] with permission from IPAC.

2.5.1 Ultrafast optical Kerr effect

The OKE is a nonlinear process that occurs when the strong optical pulse (electric field) interacts with a Kerr material (e.g. a piece of glass) and induces changes in the refractive index of a material. This induced birefringence can be employed to change the polarization state of another incident beam (the fluorescence signal). Therefore, with the combination

of two crossed polarizers before and after the Kerr material, the fluorescence signal can be gated and its decay detected by collecting the 'leakage' of the fluorescence signal as a function of the time delay between the gate pulse and the pump pulse as illustrated in Figure 2.15(b). Since the birefringence leads to polarization effects that influence all wavelengths, this technique provides a wide spectral range (within the transparent spectral window of the Kerr material and the implemented polarizers). The time resolution is usually limited by the response time of the Kerr medium, which could be a cuvette with CS_2, a quartz plate, or any suitable medium with large optical third-order susceptibility.[92–94] FS is a good Kerr material that could provide $\sim$ 200 fs, and therefore allow the investigation of the ultrafast emission dynamics of semiconducting 2D-TMDCs. However, we found that this technique is not very suitable to monitor low-intensity signals owing to a relatively important background level arising from the steady state PL leakage through the two crossed polarizers, which overlaps with the tr signal. After the unsuccessful implementation of tr OKE in the study of a bilayer TMDC heterostructure, we therefore decided to develop and implement fs-PLup, which provides background-free detection and similar time resolution to tr OKE.

2.5.2 Femtosecond photoluminescence up-conversion

Fluorescence up-conversion or fs-PLup allows recording of fluorescence with very high time resolution, basically limited by the temporal width of the laser pulses being used and the group velocity dispersion introduced by the nonlinear crystal. Thanks to the chirped

pulse amplification technique[95], commercial fs-laser systems are well-developed and widely applied in tr measurements.

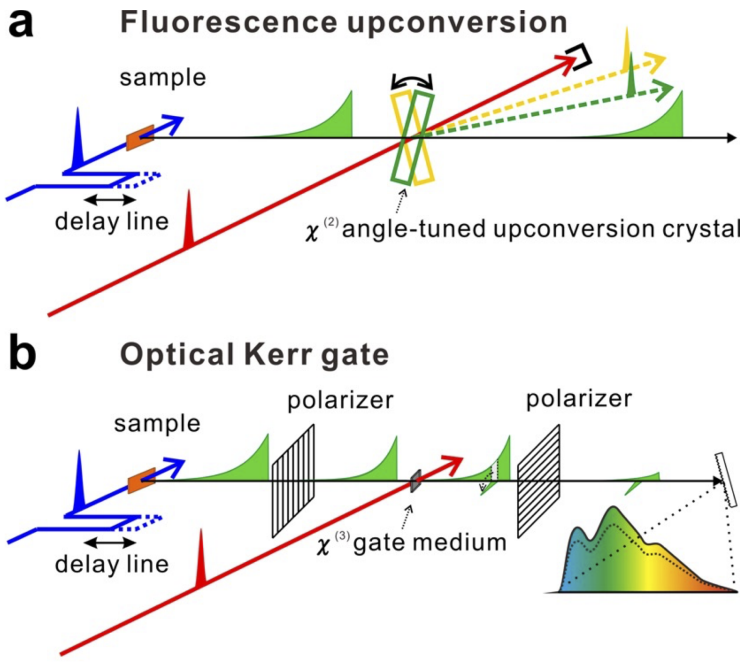

Figure 2.15: Schematic diagram showing the basic principles of the fs-PLup technique (a) and OKE (b) Reproduced from reference[96] with permission from the American Chemical Society.

Fluorescence up-conversion is a variant of sum frequency generation (SFG), which is one of the second-order nonlinear processes. The nonlinear process happens only when the laser light is sufficiently intense to modify the optical properties of materials. The induced polarization $\widetilde{P}(\mathrm{t})$ of a material depends on the strength of the applied optical field $\widetilde{E}(\mathrm{t})$

and can be written as[97],

$$\begin{aligned}\widetilde{P}(t) &= \epsilon_0[\chi^1\widetilde{E}(t) + \chi^2\widetilde{E}^2(t) + +\chi^2\widetilde{E}^3(t) + \cdots] \\ &\equiv \widetilde{P}^{(1)}(t) + \widetilde{P}^{(2)}(t) + \widetilde{P}^{(3)}(t) + \cdots\end{aligned} \tag{2.14}$$

The quantities $\chi^{(n)}$ are the n-order optical susceptibilities, and therefore $\widetilde{P}^{(n)}(t)$ is the n-order polarization. Here, only the second-order nonlinear polarization will be discussed which is related to the up-conversion process of interest. The laser electric field as the form $\widetilde{E}(t) = Ee^{-i\omega t} + cc$, where cc indicates the complex conjugate. When two electric fields with distinct frequency components interact in a second-order nonlinear optical medium the second-order nonlinear polarization results[97],

$$\begin{aligned}\widetilde{P}^{(2)}(t) = \epsilon_0\chi^{(2)}[&E_1^2e^{-2i\omega_1 t} + E_2^2e^{-2i\omega_2 t} + 2E_1E_2e^{-i(\omega_1+\omega_2)t} \\ &+ 2E_1E_2^*e^{-i(\omega_1-\omega_2)t} + c.c] + 2\epsilon\chi^{(2)}[E_1E_1^* + E_2E_2^*]\end{aligned} \tag{2.15}$$

Here, the term $\epsilon_0\chi^{(2)}2E_1E_2e^{-i(\omega_1+\omega_2)t}$ corresponds to the SFG process. From this expression, we could see that the efficiency of SFG increases with the increase of the $\chi^{(2)}$ of the nonlinear optical crystal.

The process must obey energy conservation,

$$\omega_s = \omega_1 + \omega_2 \tag{2.16}$$

as well as momentum conservation or phase matching condition,

$$\vec{k_s} = \vec{k_1} + \vec{k_2} \tag{2.17}$$

The up-conversion process is efficient only when Equation 2.17 is satisfied[98]. In the above equations ω_s and $\vec{k_s}$, and ω_i and $\vec{k_i}$ (with $i = 1, 2$) correspond to the angular frequency and wavevector of the SFG signal and the two interacting electric fields, respectively. In the particular case of the fs-PLup technique, ω_s and $\vec{k_s}$ represent the up-converted signal, ω_1 and $\vec{k_1}$ the PL signal, and ω_2 and $\vec{k_2}$ the fs optical pulse that is known as the 'gate' pulse. Since $\omega_s > \omega_1, \omega_2$ the use of a bandpass filter and a spectrograph provides background-free detection. Such a 'background-free' feature is one of the reasons that we determine to build this technique. Another benefit of up-conversion techniques is the detected signal is that $\omega_s > \omega_1$, and therefore allows us to measure fluorescence signals in the near- to mid-infrared via the implementation of a more conventional detector.

The principle of fs-PLup technique is illustrated in Figure 2.15(a). We could see that the time resolution of this technique is related to the pulse duration of the gate pulse since the up-converted signal is only produced under the presence of the gate pulse.

The working concept of this technique is straightforward; however, at the experimental level, there are several important considerations to enable the efficient generation of up-conversion.

1. **Phase matching**

The up-conversion process will efficiently happen only when the phase-matching condition

is met, and this depends on the phase-matching angle of the SFG crystal and the incident pulses[98]. There are two types of SFG crystal. One is the type I phase matching SFG crystal in which the two incident beams have the same polarization and the SFG beam is perpendicular to the incident beams. The other one is type II phase matching SFG crystal in which the two incident beams are with different polarization. In order to meet the phase-matching condition, we need to adjust the beam polarization, and then the angle of the SFG crystal according to the SFG crystal applied.

2. **Quantum efficiency for up-conversion**

The quantum efficiency for phase-matched up-conversion, η, can be expressed as[98]:

$$\eta = \frac{2\pi^2 d_{\text{eff}}^2 L^2 (P_{\text{gate}}/A)}{c\epsilon_0^3 \lambda_{\text{SFG}} \lambda_{\text{PL}} n_{\text{gate}} n_{\text{PL}} n_{\text{SFG}}(\theta_m)} \tag{2.18}$$

where P_{gate} is the power of the gate pulse, A is the area of the gate pulse, d_{eff} is the effective nonlinear coefficient of the crystal, c is the speed of light, ϵ_0 is the free-space permittivity, n is the refractive index at appropriate wavelengths λ, and L is the thickness of the SFG crystal. Here the d is the second-order nonlinear susceptibility tensor which equals $1/2\ \chi^{(2)}$. Experimentally, the strength of $\chi^{(2)}$ can depend both on material properties and operating conditions; therefore, d_{deff} is used for specific crystal and operating conditions to estimate the SFG quantum efficiency. From the equation, we could find that the quantum efficiency increases with the increase of the effective nonlinear coefficient of the crystal, the crystal thickness, and the gate pulse fluence. The typical quantum efficiency of up-conversion is $\sim 10\%$ which is similar to the OKE[99–101].

3. **Group velocity mismatch**

The group velocity mismatch between the gate and the PL or fluorescence signal reduces the ultimate temporal resolution that can be achieved using this technique. The broadening of the IRF introduced by group velocity mismatch is proportional to the thickness of the SFG crystal, and therefore the use of thinner nonlinear crystals is essential if the high temporal resolution is desired at the expense of lower η[98].

In the following subsection 2.5.3, I will introduce the fs-PLup setup developed at UeIL and the data acquisition protocol.

2.5.3 Femtosecond photoluminescence up-conversion setup

Figure 2.16 shows the layout of our up-conversion setup at UeIL. The excitation pulse for the generation of the PL signal comes from our OPA system see subsection 2.2.1. The pump beam traverses first a Berek's variable waveplate (Newport), which operates in the wavelength range of 200-1600 nm and can be used to modify the polarization state of the pump beam. Depending on the excitation wavelength we can adjust retardance from 0 to π. Then the excitation beam transits a telescope to have a collimated and tiny beam (FWHM $\approx$ 200 μm) shine on the sample. Fluorescence from the sample is collected by a 76.2 mm in diameter, 90°-OAP mirror with a 76.2 mm focal point. Since the fluorescence from the sample is like a point laser source, the sample will lie on the focal point of this 90°-OAP mirror. After this mirror, the fluorescence is collimated in a 76.2 mm diameter beam. Then this large beam is focused onto the SFG crystal by another 76.2 mm in diameter,

30°-OAP mirror with 272.23 mm focal length, and the beam diameter of fluorescence is a few mm at the focal point. The excitation beam after the sample is blocked by a tiny block placed between two OAP-mirrors, since the pump beam size is much smaller than that of the PL signal the losses are negligible. The gate pulse is the fundamental beam of our PHAROS laser system with a wavelength of 1030 nm. This beam transits a delay stage which controls the relative time between the gate and the excitation pulses. The intensity of the gate pulse is adjusted by a circular neutral density filter and its plane of linear polarization is controlled by a half-wave plate. Finally, the gate pulse passes through a telescope to obtain a collimated and tiny beam (FWHM $\approx$ 500 μm) and meets with the fluorescence signal at a type I β beta-barium borate (BBO) crystal. The BBO crystal has lateral dimensions 5 mm $\times$ 5 mm and a thickness $L = 0.4$ mm. The nonlinear crystal was purchased from Newlight Photonics, it has broad transmission and phase matching range and a high damage threshold. The angle between the gate beam and PL beam is $\sim 5°$. By adjusting of the gate beam path, the two pulses can temporally and spatially overlap, and if the phase-matching condition is satisfied the SFG signal will present. The SFG signal is collected by the Horiba Spectrometer (iHR550) which has two types of gratings for different wavelength ranges and spectral resolution and two detectors, a photomultiplier tube (PMT) and a complementary metal oxide semiconductor (CMOS) camera. For the up-conversion measurements, we use the 1800 grooves/mm plane holographic grating and the R928 PMT (Hamamatsu) with a spectral range from 185 nm-900 nm. The best wavelength resolution provided by this configuration is ~ 0.025 nm. The implementation of this setup and some preliminary results are presented in chapter 5.

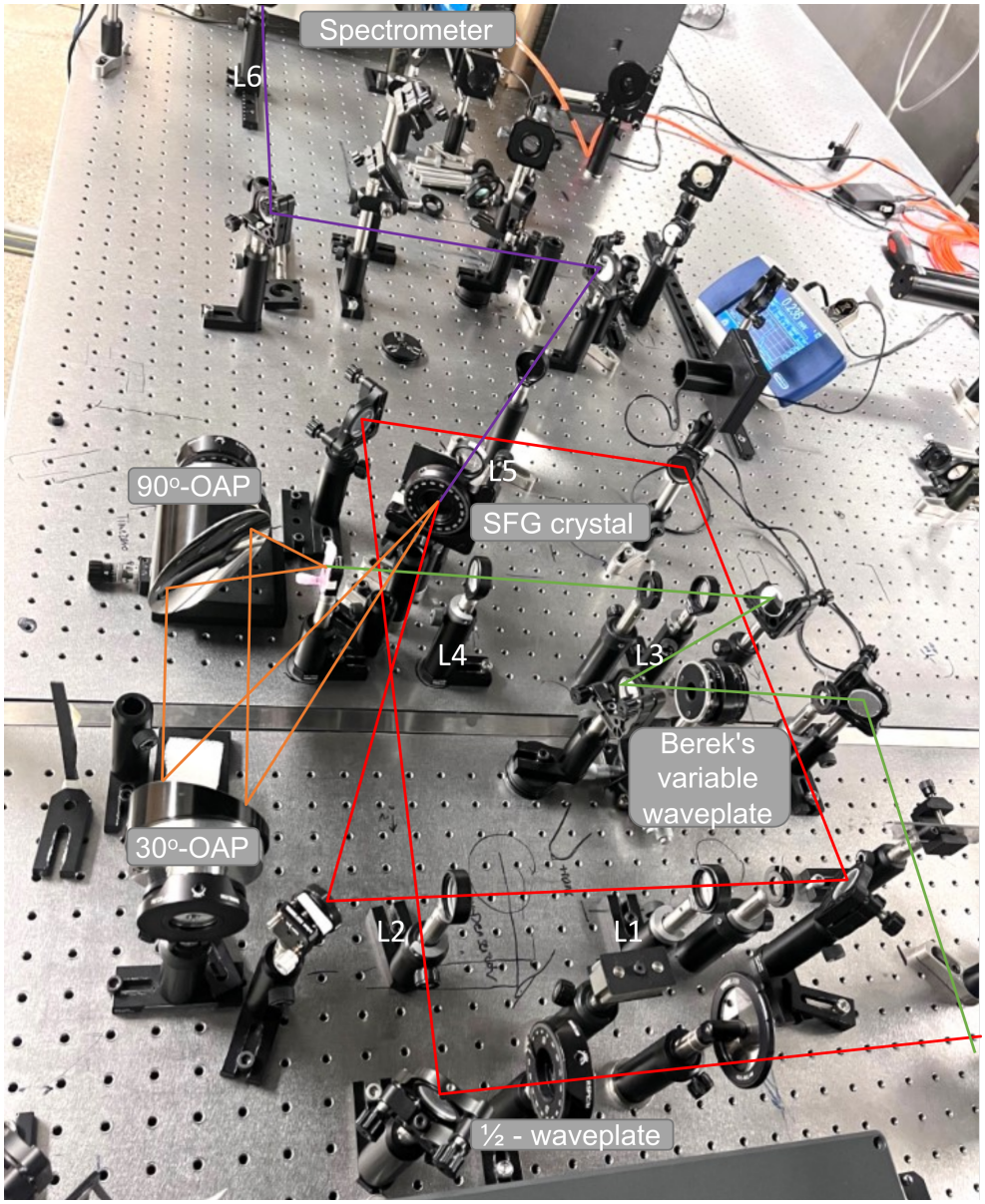

Figure 2.16: A photograph of the fluorescence up-conversion setup at UeIL. L: lens. 1030 nm beam (red), excitation pulse (green), PL beam (orange), and up-converted beam (purple).

Chapter 3

Photoninduced interlayer phenomena in $MoTe_2$

In chapter 2, I provided a general introduction about TMDCs, including their crystalline and electronic band structures, as well as a description of the implemented experimental techniques for probing photoinduced dynamics. In this chapter, I will present and discuss photoinduced interlayer phenomena observed in a bulk crystal and ultrathin flakes of T_d-$MoTe_2$, which were studied by tr-bb-TR (section 3.1) and tr-bb-TA (section 3.2), respectively.

3.1 Photoinduced interlayer dynamics in single crystal T_d-$MoTe_2$

3.1.1 Introduction

$MoTe_2$ is one of the few 2D-TMDCs that presents different polytypes with phase transitions that can be further controlled by temperature[104], alloying[105], strain[24], electrostatic gating[28], and dimensionality[106]. Relevant to this thesis is the non-centrosymmetric T_d state[107–109], which is purported to be a Weyl semimetallic phase[107–109] and displays an orthorhombic unit cell with a c-axis inclination angle (α) of 90° with respect to the plane of the layer. Above a critical temperature of $T_c \sim 250$ K[104], T_d-$MoTe_2$ undergoes the displace-

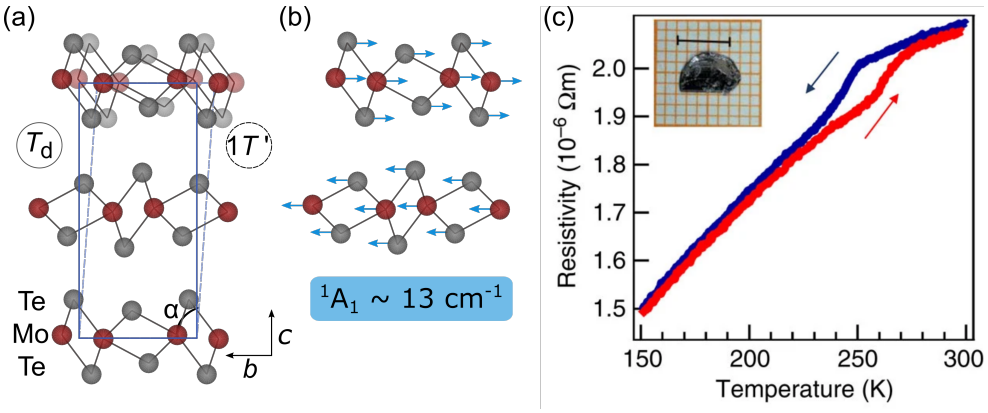

Figure 3.1: T_d and $1T'$ $MoTe_2$ unit cells and characteristic sample. (a, b) Unit cells of both $1T'$- and T_d-phases showing the change of c-axis tilt angle of $\Delta\alpha \approx 4°$[102]. Light blue arrows in (a) represent the atomic motions involved in the $^1A_1$ interlayer shear phonon mode. (c) Resistivity measurement shows a temperature-induced phase transition. The inset shows a photograph of the high-quality single crystal; scale bar, 5mm. Reproduced from reference[103] with permission from Springer Nature Limited.

ment of adjacent Te-Mo-Te layers to transition to the centrosymmetric $1T'$ phase, that is characterized by a monoclinic unit cell with $\alpha = 93.92°$ (see Figure 3.1(a)). Such breaking of inversion symmetry in T_d-$MoTe_2$ causes the appearance of a low-frequency Raman-active $^1A_1 \sim 13$ cm^{-1} interlayer shear mode (see Figure 3.1(b)). This interlayer shear mode has been exploited as a parameter to follow the aforementioned first-order thermal phase change[106,110,111] as well as possible PIPTs[1,6,30,112]. In fact, in a detailed investigation based on tr single color transient reflectivity and time-resolved second harmonic generation (tr-SHG) measurements, Zhang et al.[1,30] reported that the ultrafast photoinduced $T_d \rightarrow 1T'$ phase transition proceeds in only ~ 700 fs. This time constant is in agreement with the the sub-ps electron relaxation decays observed by time- and angle-resolved photoelectron spectroscopy (tr-ARPES)[113] in the study of the T_d phase, as well as the electron-lattice equilibration rate determined by femtosecond electron diffraction (FED)[114,115] experiments performed in the $1T'$ state[116]. Such efficient electron-phonon scattering rates varying from few hundreds of fs to several ps is not unique to $MoTe_2$ and have been reported in other TMDCs[117–121]. Furthermore, the use of FED has recently revealed that photoexcitation of the T_d-$MoTe_2$ state, in the visible and mid-infrared spectral regions, leads to an interlayer shear displacement of only few picometers (pm)[6], which is much smaller than the actual displacement necessary for the complete transition to the $1T'$ phase $\cong 19$ pm[6]. This finding is also consistent with the partial interlayer shear motion of $\cong 8$ pm observed via relativistic FED in the analogous T_d-WTe_2 compound following intense Terahertz (THz) excitation[122]. Additionally, the laser-induced $2H \rightarrow 1T'$ phase transition in $MoTe_2$ was found to require high laser power to bring the specimen to the ablation threshold, highlighting the difficulty

for photoinducing this type of interlayer-related phase transformations[25,26].

In order to investigate the effects of fs laser photoexcitation of this Weyl semimetal candidate T_d-$MoTe_2$[107–109], we carried out tr-bb-TR studies on a bulk single crystal of $1T'$-$MoTe_2$. Our high-quality broadband transient data allowed the observation of carrier and phonon dynamics over a wide range of photoexcitation levels and enabled the analyses of the dynamical behavior of the coherent $^1A_1$ interlayer shear phonon. Our studies in the bulk crystal indicate that the displacement efficiency of coherent $^1A_1$ phonons decreases with increasing photon carrier density. Furthermore, we found no signature of the ultrafast $T_d - 1T'$ PIPT.

3.1.2 Methodology

$1T'$-$MoTe_2$ crystals were grown in the group of Prof. Sun at Key Laboratory of Materials Physics, Chinese Academy of Sciences following the recipe of Zeum et al.[7], and characterized via Raman and transport measurements[106,123]. In order to have a flat and even surface, the top layer of the crystal was removed by the Scotch tape exfoliation. The single crystal was pasted onto an 8 mm × 8 mm silicon substrate which fits in the vacuum sealed compartment of the Oxford optical cryostat as shown in the Figure 3.2(a), which controls the temperature from 75 K to 500 K. During the experiment, the temperature of cryostat was set to 77 K for the single crystal of $MoTe_2$ to be in T_d phase and far from $T_c \sim 250$ K. Due to the induced motion of the sample caused by temperature changes in the cryostat, temperature-dependent measurements were not taken.

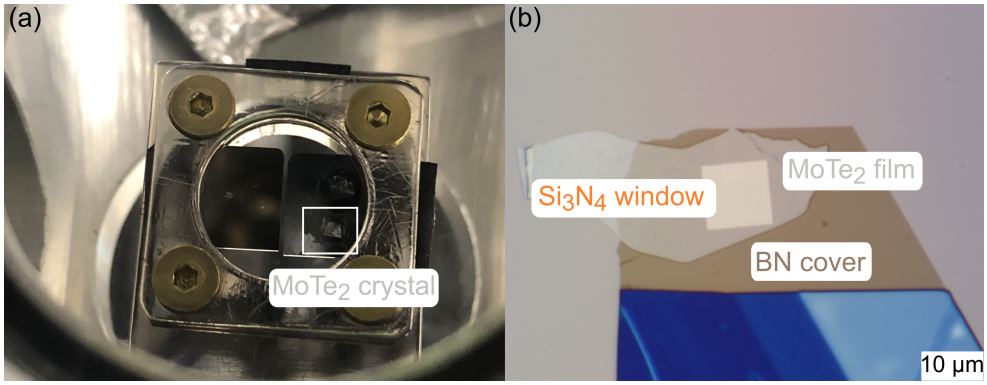

Figure 3.2: Characteristic samples of single crystal and ultra-thin $MoTe_2$. (a) Photograph of a single crystal of $MoTe_2$ mounted in the cryostat. (b) Photograph of a 40-nm thick $1T'$-$MoTe_2$ film obtained by mechanical exfoliation. The 50-nm thick 10 μm $\times$ 10 μm silicon nitride (Si_3N_4) square window (light brown), the $1T'$-$MoTe_2$ flake (silver), and h-BN protective film (brown) are clearly discernable.

The experimental layout of the tr-bb-TR was introduced in section 2.2. Here, the specific settings for these measurements will be mentioned. In our tr-bb-TR experiments $\approx$ 100-fs pump pulses centered at a photon excitation energy of $E_{\text{pump}} = 1.2$ eV (wavelength of $\lambda = 1030$ nm) were implemented to drive the electron gas and the phonon bath out of equilibrium. A small angle of 10° between pump and probe beams guaranteed that the reflected probe beam could escape from the cryostat and be collimated by a convergent lens. The probe beam and pump beam spot sizes at the crystal's surface were approximately 50 μm and 400 μm FWHM, respectively. The repetition rate of the laser system was 6 kHz and tr-bb-TR spectra were obtained by modulating the pump beam with a mechanical chopper at 500 Hz. We also minimized the collection time to avoid sample drift during the filling of liquid nitrogen, and excessive exposure to pump pulses. In this work, high-quality tr-bb-TR data were collected at gradually increasing incident fluence (F). We found that

the samples behave reversibly up to (at least) the maximum F explored in this study roughly 5 mJ·cm^{-2}.

3.1.3 Results and discussion

Figure 3.3 illustrates some characteristic results obtained at $F = 1.90$ mJ·cm^{-2}. The tr-bb-TR spectrum presented in Figure 3.3(b) reveals several key features. The strong and long-period oscillation corresponds to the coherent $^1A_1$ interlayer shear phonon mode (≈ 13 cm^{-1}), whereas the weaker ones arise from the $^2A_1$ (≈ 77 cm^{-1}) and the $^5A_1$ (≈ 164 cm^{-1}) vibrational coherences[103]. In addition, there are clear spectral weight shifts and broadening that develop on the sub-ps timescale following photoexcitation and are highlighted by the dashed rectangle in Figure 3.3(b). The characteristic time for these spectral changes is in agreement with the 300-fs decay time observed for the suppression of the intralayer distortion[6] as well as the electron-electron and electron-phonon energy relaxation rate constants determined by tr-ARPES in T_d-$MoTe_2$[113].

Figure 3.3(c) shows a slice of the tr-bb-TR spectrum at $E_{probe} = 1.42$ eV. This time trace was fitted to remove the electronic background signal and generate a residual for further FFT analysis. We limited our evaluations to $t > +1.5$ ps to circumvent the observed initial spectral changes and enable the automated fitting routine of large data sets. At $t > +1.5$ ps, electronic effects have reached a quasi-steady state, i.e., hot electrons have transferred most of their excess energy to the lattice via electron-electron and electron-phonon scattering processes within the conduction band. Therefore, the time-dependent

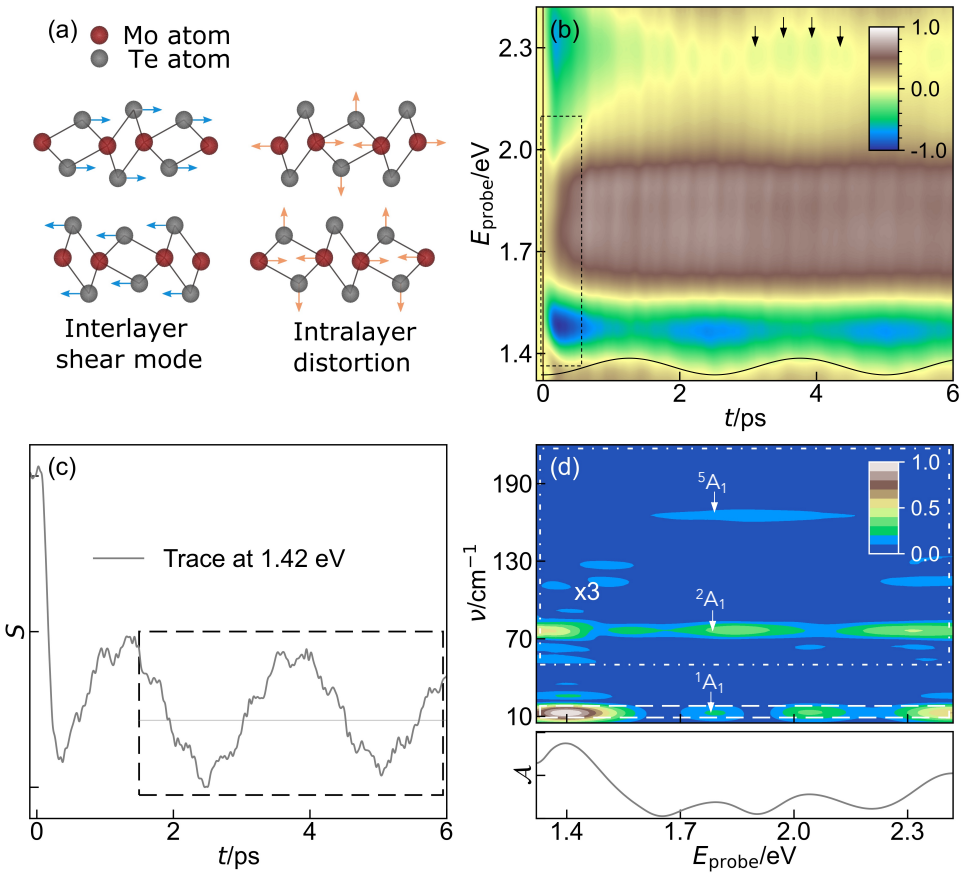

Figure 3.3: Characteristic tr-bb-TR results obtained for T_d-$MoTe_2$ at T = 77 K and F = 1.9 mJ·cm^{-2}. (a) Illustration of the interlayer $^1A_1$ shear phonon mode (left) and the atomic displacements involved in the suppression of the intralayer distortion (right). (b) Chirp-corrected tr-bb-TR spectrum. The vertical solid line indicates time zero. The sinusoidal trace and arrows were introduced to guide the eye. The former illustrates the spectral amplitude modulation introduced by the coherent $^1A_1$ ≈13 cm^{-1} phonon mode oscillation, which follows a cosine or displacive type of coherent phonon excitation. The latter pinpoints the period of the $^2A_1$ ≈ 77 cm^{-1} vibrational coherence. The dashed elongated rectangle highlights the observed spectral changes occurring at early times. (c) Temporal trace at E_{probe} = 1.42 eV. The dashed rectangle indicates the portion of the trace employed to carry out further FFT analysis. (d) Fourier intensity map obtained from residuals as the one shown in panel c. The weaker FFT-amplitudes of the characteristic $^2A_1$ (77 cm^{-1}) and $^5A_2$ (164 cm^{-1}) phonons of the T_d phase are also shown with their intensities scaled by a factor of 3 as indicated by the dash-dotted rectangle.

reflectivity changes at $t > +1.5$ ps are mostly governed by the oscillatory dynamics of coherently excited phonons. This procedure was applied at each value of E_{probe}, yielding the Fourier intensity map displayed in the top panel of Figure 3.3(d). The bottom panel of Figure 3.3(d) exhibits the values of the FFT-amplitude of the $^1A_1$ vibrational coherence ($\mathcal{A}$) as a function of E_{probe}, which were obtained through averaging along the small frequency interval specified by the dashed rectangle shown in the top panel of Figure 3.3(d). We were able to determine the effects of increasing F on the TR spectrum (S), $\mathcal{A}$, and the central frequency (ν_c) of the coherent $^1A_1$ phonon. These findings are summarized in Figure 3.5.

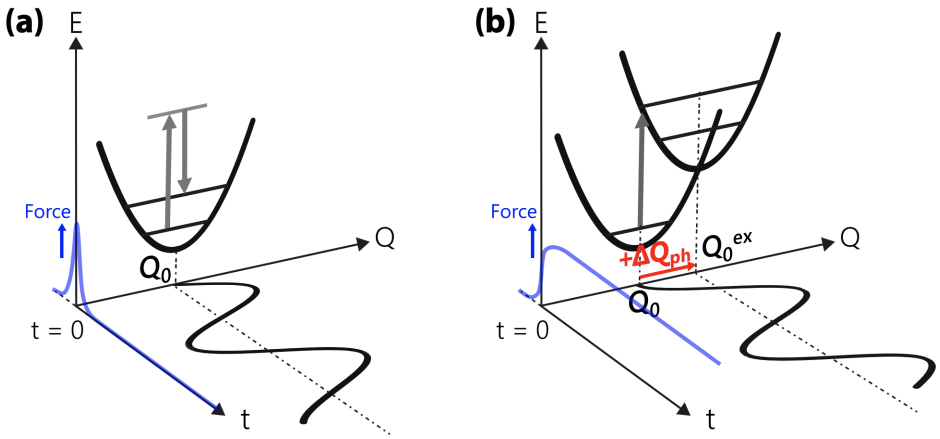

Figure 3.4: Generation mechanisms of coherent oscillations. Whereas the impulsive stimulated Raman scattering does not alter the average lattice coordinates, a displacive excitation can cause a shift of the coordinates in the excited state (from Q_0 to Q_0^{ex}). There should be light absorption to generate the displacive oscillations, while the impulsive ones require no absorption. Reproduced from reference[124] with permission from the American Physical Society.

Different theories have been put forward to explain the mechanism for the generation of coherent A_1 phonons in simple semimetals and semiconductors, asserting the challenges

involved in describing the driving force responsible for launching such coherent nuclear motion[125–134]. The sinusoidal curve in Figure 3.3(b) pinpoints the phase of the $^1A_1$ vibrational coherence relative to time corresponding to a cosine function. This fact suggests the displacive[125,132] or resonant impulsive stimulated Raman scattering (ISRS)[129] mechanisms are responsible for the generation of the coherent $^1A_1$ phonon mode. Moreover, the phase of $^2A_1$ vibrational coherence with respect to time zero corresponds to a sine function. Therefore, the non-resonant ISRS process governs the production of the $^2A_1$ vibrational coherence. The assignment of the phase of the $^5A_2$ phonon mode was not possible due to the limited temporal resolution of our pump-probe instrument $\approx$ 100 fs. Figure 3.4 illustrates the displacive type and non-resonant ISRS mechanisms for the generations of coherent phonons. In optically transparent materials, ISRS dominates, and as shown in Figure 3.4(a) the resulting oscillation is a sine function of time (zero amplitude at time zero). In absorbing materials, both mechanisms may take place. The displacive excitation involves a sudden modification of the carrier density or electronic temperature induced by the intense pump pulse, modifying the potential energy surface and triggering the motion of the ions, which follow a cosine-like oscillation as shown in Figure 3.4(b).

Figure 3.5(a) and (b) display the changes of F-normalized spectra (S/F) as a function of F for the T_d and $1T'$ phases, respectively. The broadband-TR spectra were obtained by averaging data in the time domain between $t \approx +$ 2.5 ps and +5 ps. This temporal interval corresponds approximately to one period of the coherent $^1A_1$ phonon oscillation, see Figure 3.3(c) and inset in Figure 3.5(a), and this procedure was done to wash out

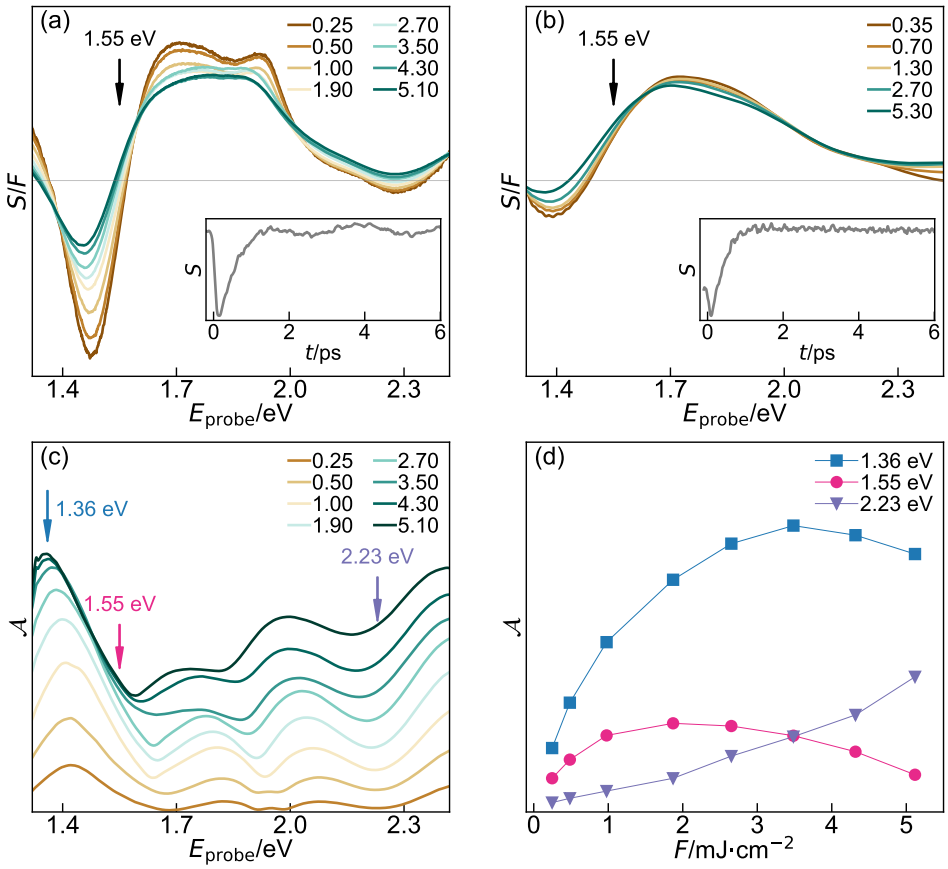

Figure 3.5: Fluence dependent tr-bb-TR results obtained for T_d-$MoTe_2$ at T = 77 K and $1T'$-$MoTe_2$ at T = 295 K. (a), (b) Fluence-normalized transient spectra (S/F) for the T_d (a) and $1T'$ (b) phases. The traces were time-averaged between $t \approx 2.5$ ps - 5 ps (one $^1A_1$ phonon oscillation period). The traces in panel b were scaled by a factor of 2 with respect to those in panel a. The insets show the characteristics temporal traces obtained at E_{probe} = 1.55 eV (arrows) and F = 1.90 mJ·cm^{-2} (a) and F = 2.70 mJ·cm^{-2} (b). (c) $^1A_1$ Fourier intensity spectra as a function of F. The arrows indicate the values of E_{probe} selected to plot the fluence dependence of FFT-intensities in panel d.

the oscillatory effect caused by the vibrational coherences on the TR signal. It is often expected for S to scale approximately proportionally with F, or in other words to remain constant when normalized by F. This is indeed the case for the optical response of the $1T'$ phase, which is illustrated in Figure 3.5(b). In contrast, the dielectric response of the T_d state presents deviations near $E_{\text{probe}} = 1.45$ eV. In addition, it is worth to mention that the TR spectra in Figure 3.5(b) has been rescaled by a factor of 2 with respect to those shown in Figure 3.5(a). These weaker TR signals can be explained by the higher baseline temperature of the $1T'$ phase, which leads to a higher population of thermal carriers, and therefore a relatively smaller change arising from the additional photo-generated electron-hole pairs. The interpretation of the observed TR spectral changes is rather challenging since our E_{probe} range involves high-energy interband transitions[135].

Figure 3.5(c) exhibits $^1\text{A}_1$ Fourier intensity spectra as a function of F. The most noteworthy observation is the progressive red-shift of spectral features with increasing F. This indicates that the interband transitions that are dielectrically susceptible to the coherent $^1\text{A}_1$ phonon displacement experience a large degree of renormalization due to electronic and/or thermally induced effects, and this is likely the cause for the deviations observed in the F-dependence of S/F in Figure 3.5(a). Figure 3.5(d) shows the F-dependence of $\mathcal{A}$ at three selected E_{probe} values. Our result at $E_{\text{probe}} = 1.55$ eV is in reasonable agreement with that obtained by Zhang et at.[1,30], which shows a maximum at $F \approx 1.5$ mJ·cm^{-2}. However, our broadband data reveal no abrupt or threshold-like behavior that could indicate the progression of a sub-ps photoinduced nonthermal $T_d \rightarrow 1T'$ phase transition[1]. It also

becomes clear that the F-behavior of $\mathcal{A}$ is strongly dependent on E_{probe}; at $E_{\text{probe}} = 1.36$ eV $\mathcal{A}$ reaches a maximum at $F \sim 3.5$ mJ·cm^{-2} whereas at $E_{\text{probe}} = 2.23$ eV $\mathcal{A}$ increases monotonously with F. These distinct changes are a consequence of the overall red-shift and sublinear evolution of $\mathcal{A}$ with increasing F.

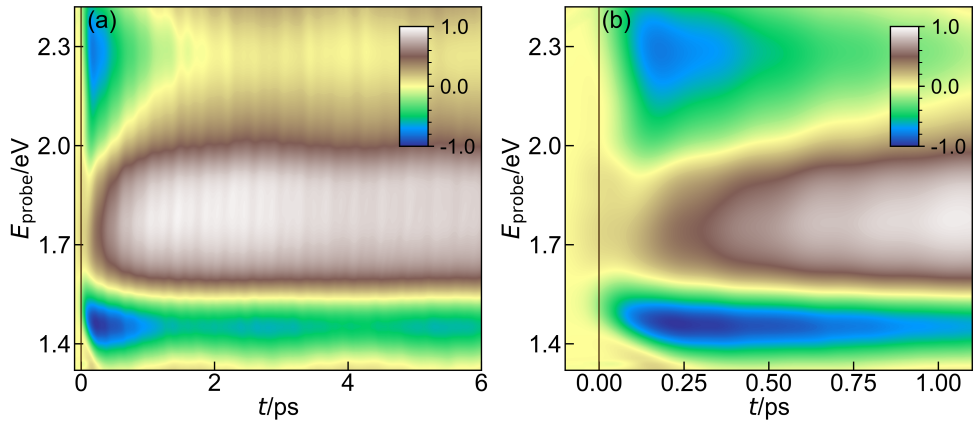

Figure 3.6: Characteristic tr-bb-TR results obtained for T_d-$MoTe_2$ at T = 77 K and F = 5.1 mJ·cm^{-2}. (a) Chirp-corrected tr-bb-TR spectrum of T_d-$MoTe_2$ recorded at T = 77 K and F = 5.1 mJ·cm^{-2}. (b) Close-up view of the first ps following photoexcitation highlighting the smooth continuity of $^1A_1$ and $^2A_1$ coherences.

Furthermore, as can be discerned by eye inspection of Figure 3.6, there is a clear continuity of the amplitudes of the $^1A_1$ and $^2A_1$ coherent phonon modes even at $F = 5.1$ mJ·cm^{-2}. This fact also disagrees with the occurrence of a phase transformation, which is expected to lead to the sudden disappearance of vibrational coherences[136]. At this photoexcitation level and according to the energy balance, $\int_{77K}^{T_{l,m}} C_p(T)\, dT = \frac{F\,(1-R)\,M}{\rho\,\delta}$, the lattice should transiently reach a maximum temperature $T_{l,m} \approx 480$ K, which is well above T_c (C_p is the heat capacity of $MoTe_2$[137], F is the incident fluence, $\delta \approx 50$ nm is the optical absorption

depth at $E_{\text{pump}} = 1.2$ eV[138], $M = 351.1$ g·mol^{-1}, $\rho = 7.78$ g·cm^{-3}, and $R \approx 0.4$ is the reflectivity at the crystal-vacuum interface[135]). We assumed that the latent heat for the $T_d \rightarrow 1T'$ phase transition is smaller than or of the order of the one for the transformation between $2H$ and $1T'$ polytypes (16 meV)[24]. This represents a small fraction (≈ 0.1 mJ·cm^{-2}) of the absorbed fluence (≈ 3.1 mJ·cm^{-2}) and can be then neglected. Hence, we found no evidence for an ultrafast photoinduced $T_d \rightarrow 1T'$ phase transition, neither nonthermal[1] nor thermal.

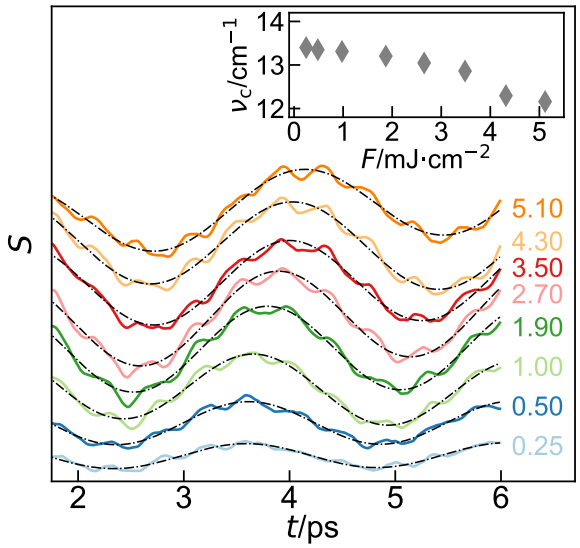

Figure 3.7: Temporal evolution of the $^1A_1$ vibrational coherence with increasing F. The traces were taken at $E_{\text{probe}} = 1.4$ eV (a region of high signal to noise ratio) and vertically shifted for clarity. The dot-dashed traces are fits of the data with a sine function to extract the phonon frequency (ν_c). The extracted values of ν_c as a function of F are shown in the inset. The values on the right of each trace correspond to fluences in mJ·cm^{-2}.

Figure 3.7 shows the time evolution of the coherent $^1A_1$ phonon mode as a function of F.

Fittings of these traces reveal the decrease of the $^1A_1$ frequency with increasing F. This manifests the weakening of interlayer transverse cohesive forces, which is likely caused by thermal effects[139,140]. We, therefore, hypothesize that the observed time-resolved changes and phonon dynamics are characteristic of a hotter metastable T_d-like phase.

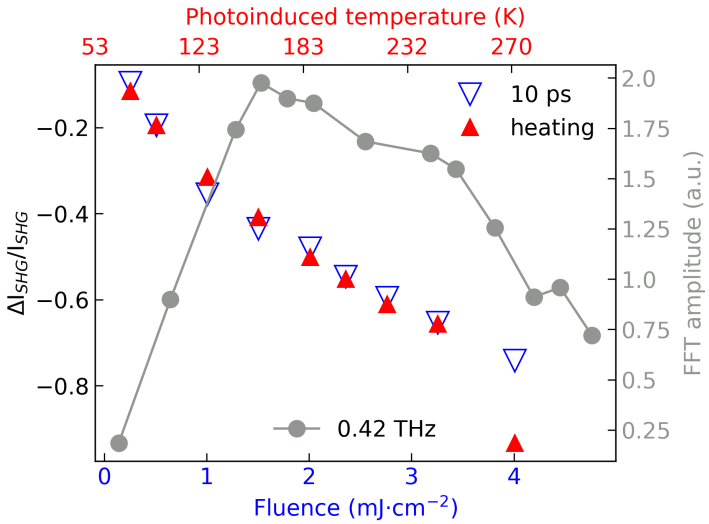

Figure 3.8: Combined data from Figure 3(d) and Figure 4(c) from reference[30]. The grey trace corresponds to the amplitude of the $^1A_1$ shear mode (0.42 THz, 13 cm^1) determined by impulsive fs-TR at a temperature of 4 K. The pump and probe photon wavelengths were 800 nm. The solid red symbols correspond to SHG measurements as a function of temperature with SHG signal at 10 K taken as a reference. The open blue symbols correspond to tr-SHG measurements (at t = + 10 ps and a temperature of 10 K) as a function of incident laser fluence (bottom axis) and calculated photoinduced temperature by the authors (top axis).

Our findings contradict the claims of Zhang et al.[1,30] and made us reconsider the requirements for a PIPT to proceed on the sub-ps timescale. In the following paragraphs, I will present a different interpretation of their results. In Figure 3.8, the grey symbols represent data obtained by Zhang et al. The authors also found a threshold at $F \sim 1.5$ mJ·cm^{-2}

(λ_{pump} = 800 nm) from which there is a clear decrease of the amplitude of the $^1A_1 \sim 13$ cm^{-1} shear phonon mode. The red symbols in the figure correspond to the change of SHG signal from the crystal as a function of the sample temperature with the signal at 10 K as a reference. The open blue symbols correspond to the tr-SHG signal measured at t = + 10 ps following optical excitation of the crystal at a base temperature of 10 K. The authors also calculated the photoinduced lattice temperature (top axis) as a function of the incident fluence (bottom axis). The very good correspondence between the thermal and photoinduced changes indicates that the observed tr-SHG decay is caused by thermal effects. In addition, if T_d would transition to $1T'$ the values at T > 250 K (last data points, red and blue) should coincide. Instead, a clear monotonic decrease suggests that laser excitation does not change the non-centrosymmetric character of the initial phase. We believe that the observed fast decay in their tr-SHG measurements are due to the already known fast electron-phonon equilibration process[113] that would lead to an increase of the lattice temperature on the sub-ps timescale.

Our tr-bb-TR measurements in the single crystal are comparable to their work. The difference is that we were conducting with a WL probe which could explore the dynamics from 540 nm to 950 nm. A similar trend of the amplitude of the $^1A_1$ shear mode was observed (see the grey trace at E_{probe} = 1.55 eV in Figure 3.8 and the magenta trace at E_{probe} = 1.55 eV in Figure 3.5). From our tr-bb-TR measurements, we observed the red shift of the maximum of the $^1A_1$ shear mode which presented the decreasing of the Fourier amplitude at E_{probe}=1.55 eV. We didn't not perform tr-SHG measurements. The use of the

SHG in the study of single- to multi-layer 2D-TMDCs[141–145] has gained attraction owing to the fact that the second-order nonlinear susceptibility, $\chi^{(2)}$, vanishes in centrosymmetric systems. However, a discrepancy seems to exist between the conclusions drawn from the interpretation of structural data arising from FED[6,122] experiments and those attained via tr-SHG measurements[1,30,122]. The latter appears to indicate the near disappearance of the noncentrosymmetric character of T_d-MTe_2 (M = Mo, W), and therefore a complete transformation to a $1T'$-like phase. Notice that, unlike most commonly employed nonlinear optical crystals, the $\chi^{(2)}$ of 2D-TMDCs has shown to be strongly dependent on strain[141–144] and temperature[1,30,145] complicating the analysis of tr-SHG[1,6,30,122] signals, and thus justifying this apparent controversy.

3.1.4 Conclusions

The success of known reversible ultrafast photoinduced phase transformations[118,136,146–154] rests on the ability of the sample to return to its original ground-state configuration before the next pair of pump and probe pulses excite and interrogate the system again. We would like to emphasize that the actual atomic rearrangements in crystalline systems capable of withstanding billions of photoexcitation cycles are well localized within the frame of an arbitrary unit cell. In contrast, the $T_d \rightarrow 1T'$ phase transition comprises the relative displacement of adjacent Te-Mo-Te layers. This process concerns many rigidly connected atoms that must respond collectively over the extent of a microscopic domain, and therefore it is unlikely to complete on the sub-ps timescale. Such a barrierless picture does not

account for local variations in energy barriers and the degree of electronic delocalization. In fact, we believe that photoexcitation leads to a transiently hot T_d-like state that dissipates the excess of energy into the bulk before having sufficient time to structurally transition to the $1T'$ phase.

Our results agree with the scenario of the photoinduced formation of a metastable hot T_d-like state with weaker cohesive interlayer forces, in which the suppression of the intralayer distortion[6], i.e. a localized atomic rearrangement, and the presence of domain walls in the $a-b$ plane and along the stacking c-axis[155] may progressively facilitate a small shear displacement[6,122]. Photoinduced phase transitions are playing an increasingly important role in quantum materials and devices designed to confer properties on demand[156]. We hope that our discussion will bring a better understanding of the requirements for structural phenomena to be able to proceed on ultrafast time scales.

3.2 Persistent photogenerated state attained by femtosecond laser irradiation of ultrathin T_d-$MoTe_2$ flakes

3.2.1 Introduction

In this section we investigate the effects of intense fs laser irradiation on $\approx$ 30 nm to 40 nm thick flakes of T_d-$MoTe_2$. We will show persistent fs-laser induced changes affecting the

dynamical behavior of the coherent $^1A_1$ interlayer shear phonon as monitored by tr-bb-TA spectroscopy. This laser-driven transformation is assigned to the formation of a long-live photoinduced state, herein referred to as T^*. Figure 3.9 depicts the main findings in a simple scheme that links the pristine T_d and $1T'$ phases with the photogenerated T^* state, illustrating the observed fs-laser induced transformations that are depicted by laser pulse arrows.

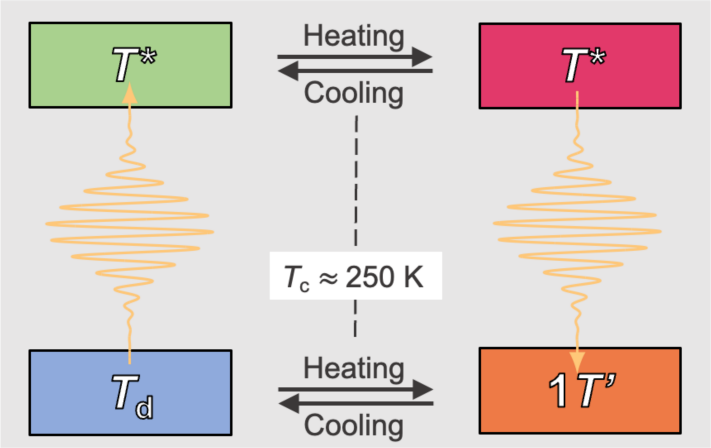

Figure 3.9: Simple scheme depicting the observed fs-laser irradiation processes. There is the formation of the T^* state via irradiation of the T_d phase at low temperature, and its conversion to $1T'$ by irradiation at room temperature.

3.2.2 Methodology

Ultrathin flakes were obtained by mechanical exfoliation of a $1T'$-$MoTe_2$ single crystal inside a nitrogen-filled glove box and transferred onto specially nano-fabricated substrates with a 10-μm × 10-μm Si_3N_4 windows. $MoTe_2$ films prepared by mechanical exfoliation of

a single crystal are known to be of high crystalline quality and have been previously shown to retain their metallic properties down to low temperatures[106,123]. The freestanding Si_3N_4 windows served to spatially overlap the beams and to ensure that the entire transmission of the probe beam passed through the $MoTe_2$ film of interest. It was essential to assure the whole window was covered by the flake under study. H-BN was used to cap the $1T'$-$MoTe_2$ for protection against air moisture[6] as shown in the Figure 3.2(b). An atomic force microscope was used to determine the $1T'$-$MoTe_2$ flake thickness underlying h-BN. Samples were prepared by the team of Prof. Adam W. Tsen (University of Waterloo).

The experimental layout of tr-bb-TR and a detail of our transient spectroscopic setup is introduced in section 2.2. We utilized pump pulses with $E_{\text{pump}} = 2.4$ eV ($\lambda = 515$ nm) to perform all tr-bb-TA in flakes. This E_{pump} was outside the E_{probe} window and facilitated the alignment of the pump beam by monitoring the transmission of green light through the body of each flake deposited onto each small 10-μm x 10-μm Si_3N_4 window. The probe beam spot size at the sample was about 20 μm (FWHM) whereas the pump beam spot size was set to 350 μm (FWHM). TA spectra were obtained by modulating the pump beam with a mechanical chopper at 42 Hz. The main challenge in our tr-bb-TA studies has been to achieve high SNR in transient spectra attained from such small, probed volumes, and for thicker flakes owing to the poorer probe beam transmittance of samples that are semimetallic in nature. This limited the total timespan in our tr-bb-TA experiments to about 15 ps. However, this experimental configuration guaranteed the characterization of a well-defined body, reproducible positioning of the flake, and enabled the performance of

sequential studies, e.g. tr-bb-TA measurements as a function of base temperature, after thermal annealing, etc. on a given specimen. Note that owing to thermal expansion effects, a change of the base temperature led to sample drift, and therefore the proper repositioning of the specimen becomes crucial to succeed with comparative analyses. In addition, experiments should not last for more than a week since $MoTe_2$ is sensitive to moisture and degrades[6].

3.2.3 Results and discussion

Figure 3.10 presents some characteristic tr-bb-TA results obtained for a 40 T_d-$MoTe_2$ flake at T = 74 K. We observed that samples behave reversibly below incident pump fluences, $F \approx 1$ mJ·cm^{-2}. Therefore, experiments performed below this fluence threshold served to monitor the dynamical behavior of the coherent $^1A_1$ shear phonon following impulsive laser irradiation treatments, vide infra. It is worth mentioning that the response to impulsive photoexcitation of thin flakes was found to differ from that of a bulk T_d-$MoTe_2$ crystal[112], which showed structural reversibility up to at least $F \approx 5$ mJ·cm^{-2}. We restricted the fittings of time traces to time delays $t \geq +2$ ps (e.g., Figure 3.10(b)) to enable the automated removal of the electronic background and the generation of residuals, R_E (e.g., inset in Figure 3.10(b)), from which we could extract the phonon dynamics[112].

Figure 3.10(c) displays the Fourier power spectrum obtained from the analysis of the tr-bb-TA spectrum (Figure 3.10(a)). The Fourier amplitudes ($\mathcal{A}$) of the $^1A_1 \approx 13$ cm^{-1}, $^2A_1 \approx 77$ cm^{-1} and $^5A_2 \approx 164$ cm^{-1} Raman active modes of the T_d-phase and their

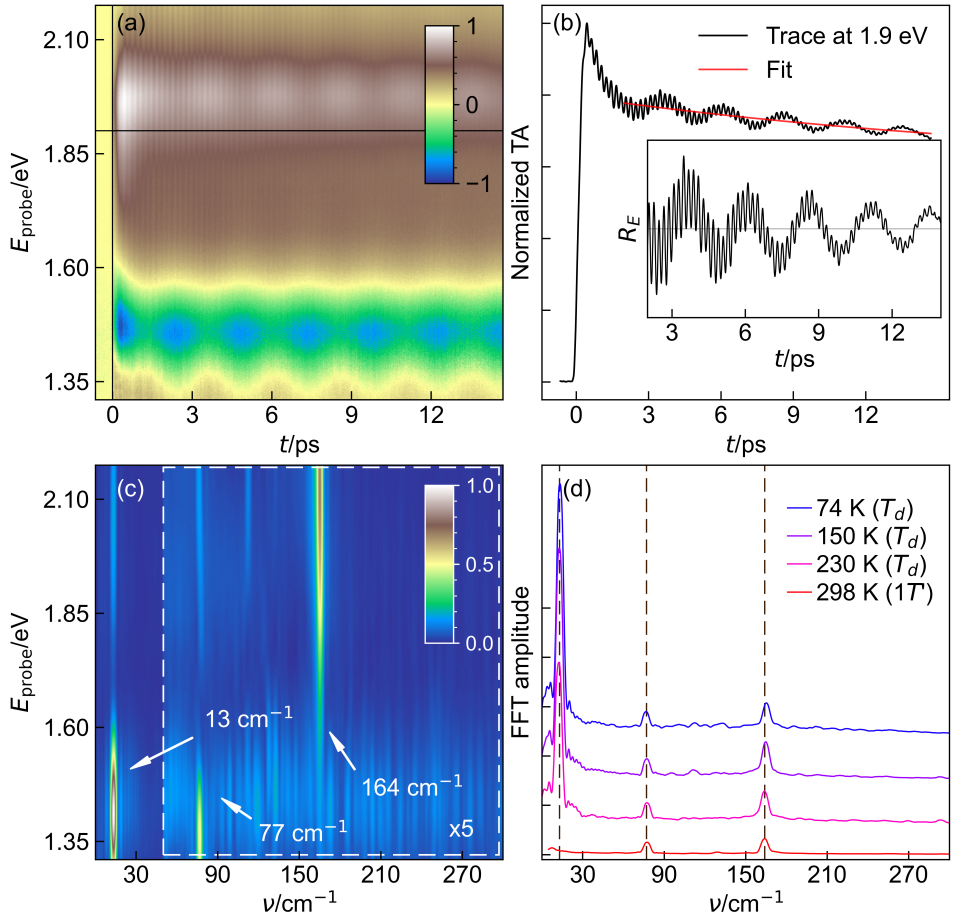

Figure 3.10: Characteristic tr-bb-TA results obtained for 40-nm thick $MoTe_2$ flake. (a) Tr-bb-TA spectrum of T_d-$MoTe_2$ recorded with $F = 0.5$ mJ·cm^{-2}, $E_{pump} = 2.4$ eV. Vibrational coherences are clearly observable as oscillatory components. (b) Black, temporal trace at $E_{probe} = 1.9$ eV (horizontal line in panel a); red, linear fit performed within the interval $t = +2$ - $+14$ ps to remove the electronic background and generate the residuals, R_E (inset), for further FFT analysis. (c) Fourier power spectrum obtained from FFT of residuals showing the characteristic frequencies of the Raman active modes of the T_d (1T'), $^1A_1 \sim 13$ cm^{-1}, $^2A_1 \sim 77$ cm^{-1} and $^5A_2 \sim 164$ cm^{-1}. (d) Fourier spectra as a function of T. These were obtained via averaging along E_{probe} Fourier power spectra as the one shown in panel c.

dependencies with E_{probe} are visible. The detection of higher frequency modes is currently limited by the temporal response function of our pump-probe setup ~ 100 fs. Figure 3.10(d) shows Fourier spectra as a function of the sample temperature. The spectrum at room temperature (298 K) reveals that the flake has transitioned to the $1T'$ phase as evidenced by the disappearance of $\mathcal{A}(^1\text{A}_1)$. Hence, the other two phonons with frequencies of ≈ 77 cm^{-1} and ≈ 164 cm^{-1} that are still present at 298 K correspond to the $^1\text{A}_g$ and the $^8\text{A}_g$ Raman active modes of the high-temperature $1T'$ state.

Figure 3.11 displays the results obtained for a 32-nm thick flake at a base temperature of 220 K (just below $T_c \approx 250$ K). In this case, tr-bb-TA measurements were performed at different F as specified chronologically from top to bottom in Table 3.1. As can be observed in Figure 3.11(b), $\mathcal{A}(^1\text{A}_1)$ decreases as the F increases for values above 1 $\text{mJ}\cdot\text{cm}^{-2}$, reaching the background level at $F \approx 2$ $\text{mJ}\cdot\text{cm}^{-2}$. After this point we assume the complete transformation of T_d into T^*. On the other hand, no substantial changes are found in the fluence-normalized and time-averaged broadband TA spectra shown in Figure 3.11(a), which indicate that the material's response scales linearly with F[112] and T^* presents a similar TA spectrum to T_d. This latter observation is expected since the linear reflectivity spectra of the T_d and $1T'$ phases are very similar in this E_{probe} region that is dominated by interband transitions[157]. Note that the decrease of $\mathcal{A}(^1\text{A}_1)$ with increasing F does not arise from sample damage, but from a structural modification that can be reverted by laser irradiation, vide infra. We have found that the fluence thresholds for damaging the films due to the laser's peak power vary from flake to flake and are usually in the range of $F_{th} \approx$

5 mJ·cm^{-2} to 7 mJ·cm^{-2}. Sample damage is characterized by clear and permanent changes in the TA spectrum as well as the Fourier amplitudes of the ≈ 77 cm^{-2} and ≈ 164 cm^{-2} phonons (see laser irradiation tests 3 listed below).

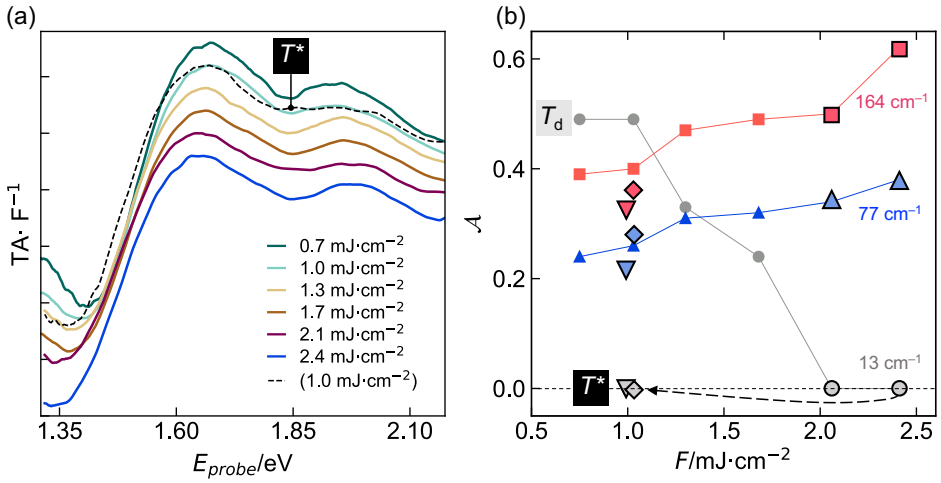

Figure 3.11: Fluence dependent measurements on a 32-nm thick T_d-$MoTe_2$ flake at a base temperature of 220 K. (a) Fluence normalized transient absorption spectra (TA·F^{-1}) as a function of F. The parentheses indicate that F was reduced to 1.0 mJ·cm^{-2} after full transformation to T^*. The TA spectra were obtained by averaging in the time domain signal between t = +2 - +14 ps to remove the effect of vibrational coherences. The spectra were offset for clarity. (b) $\mathcal{A}$ of three main coherent phonon modes. $\mathcal{A}(^1A_1)$ reaches background level at $F \approx 2$ mJ·cm^{-2}. At this point T_d fully transformed into T^*. The diamonds correspond to measurement under the same condition (i.e., 220 K) but after thermally annealing T^* at 500 K and reducing F to 1.0 mJ·cm^{-2} as indicated by the arrow. The flake remained in the T^* state. The inverted triangles correspond to a final measurement performed at 298 K and F = 1.0 mJ·cm^{-2}.

Following the formation of T^*, we performed annealing (step 8 in Table 3.1) up to 500 K the upper limit of our cryostat and found that $\mathcal{A}(^1A_1)$ does not recover (diamonds in Figure 3.11(b) and step 8 in Table 3.1). This observation indicates that T^* withstands

thermal cycling, and therefore discards the possibility for T^* to be a kinetically trapped pristine $1T'$ state at low temperature. The latter would have led, upon cooling, to the pristine T_d structure with its characteristic $^1A_1$ vibrational coherence.

Specimen: 32-nm thick flake					
F(mJ·cm^{-2})	T(K)	#scans	#shots/scan(millions)	#shots(millions)	#cumulative(millions)
0.7	220	3	290	870	870
1.0	220	3	290	870	1740
1.3	220	3	290	870	2610
1.7	220	1	290	290	2900
2.1	220	1	290	290	3190
2.4	220	1	290	290	3480
Sample was annealed at 500 K and returned to 220 K for tr-bb-TA measurements.					
1.0	220	3	290	870	4350
Sample was brought to room temperature for tr-bb-TA measurements.					
1.0	220	3	290	870	5220

Table 3.1: Measurements carry out on a 32-nm thick-flake in chronological order from top to bottom. The higher number of scans at lower F values were done to enhance the signal-to-noise ratio.

We believe that T^* reflects a laser-modified interlayer state, in which the coupling to the generation of $^1A_1$ vibrational coherences has been affected, for instance, through the formation of interlayer strain as recently observed in T_d-WTe_2 by FED[122]. We performed laser irradiation tests with a limited number of shots at a low repetition rate to study the laser-induced formation of T^*. In detail, laser irradiation tests were performed on five flakes to study the effects of laser-induced interlayer strain buildup and sample damage under controlled laser irradiation conditions. The experiments shown below are based on the exposure of thin flakes to controlled fs-laser irradiation at high F and low repetition rate (10 Hz) followed by tr-bb-TA measurements carried out within the nondisruptive F regimen < 1 mJ·cm^{-2} at 20 kHz. Given the irreversible character of T^*, the latter measurements

are used to monitor $\mathcal{A}(^1\mathrm{A}_1)$; i.e., the presence or absence of the $^1\mathrm{A}_1$ vibrational coherence. The values of $\mathcal{A}(^1\mathrm{A}_1)$ have been normalized by the maximum magnitude of the TA signal to compensate for fluctuations in laser power arising from the sudden change of the repetition rate of our laser system between successive irradiation and test measurements as well as minor sample misalignment. Three laser irradiation tests are plotted below, and two more can be found in Appendix B.

Test 1: 30-nm thick $MoTe_2$ sample – laser excitation of $1T'$ state

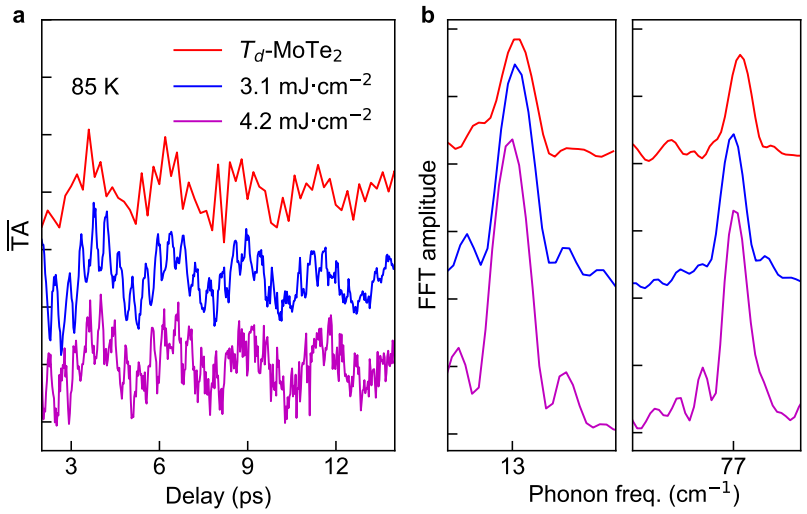

Figure 3.12: Laser irradiation test of a 30-nm thick $1T'$−$MoTe_2$ flake. (a) Persistence of the $^1A_1$ phonon mode upon increasing F (inset). The sample was irradiated at 298 K and cooled down to 85 K for measuring phonon dynamics. The time traces have been averaged within $E \sim 1.38-1.55$ eV to improve the SNR. Even at the highest irradiation level of $F = 4.2$ mJ·cm^{-2} the trace clearly shows the $^1A_1$ phonon mode characteristic of the T_d-phase. The first irradiation process was conducted for 5 minutes at 10 Hz (3000 pulses with $F = 3.1$ mJ·cm^{-2}). The second irradiation process was conducted for 10 minutes at 10 Hz (6000 pulses with $F = 4.2$ mJ·cm^{-2}). Tr-bb-TA measurements were performed at 85 K and $F = 0.5$ mJ·cm^{-2}. $E_{\text{pump}} = 2.4$ eV. The red trace corresponds to the pristine sample, and it was recorded with a coarser time step of 150 fs instead of 30 fs. (b) Frequency spectra obtained from each trace via FFT. The observed persistence of the coherent $^1A_1 \sim 13$ cm^{-1} shear phonon mode in the T_d-state suggests that the buildup of strain occurs only if the initial state is the T_d-phase.

Test 2: 35-nm thick $MoTe_2$ sample – strain buildup and release

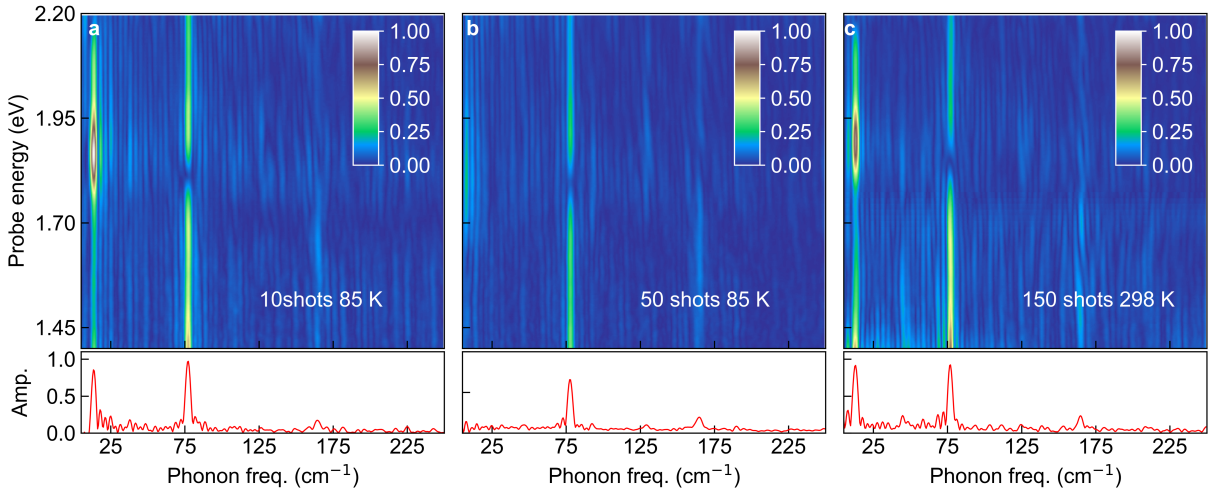

Figure 3.13: Fourier power spectra for laser irradiation test 2. (a) After laser irradiation, 10 shots at 85 K, $F = 6.5$ mJ·cm^{-2}. (b) Same specimen after a total of 50 shots at 85 K, $F = 6.5$ mJ·cm^{-2}. (c) Same specimen after additional 100 shots at 298 K, $F = 4.6$ mJ·cm^{-2}. All tr-bb-TA were performed at 85 K, $F = 0.5$ mJ·cm^{-2}. All data were normalized by the maximum Fourier amplitude obtained for the experiment shown in panel a.

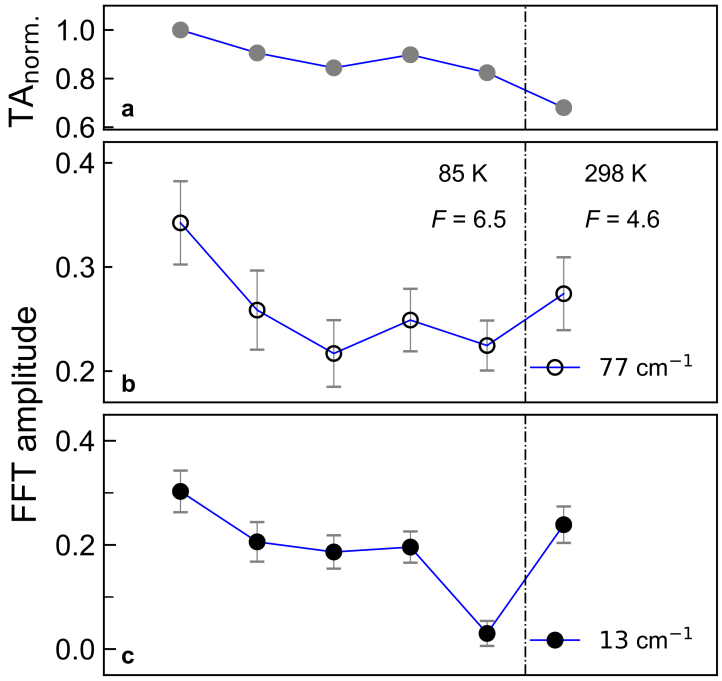

Figure 3.14: Laser induced changes as a function of the cumulative number of laser irradiation pulses for laser irradiation test 2. From left to right the number of cumulative laser shots is 10, 20, 30, 40, 50, and 150. (a) Recorded maximum magnitude of TA signal, normalized by its initial value. (b) Fourier amplitude of the 77 cm^{-1} mode. (c) Fourier amplitude of the 13 $^{-1}$ mode. The temperatures and fluences employed during laser irradiation exposures are indicated in the figure. All tr-bb-TA measurements were carried out at 85 K, $F \approx 0.5$ mJ·cm^{-2}.

Test 3: 35-nm thick MoTe2 sample – film damage

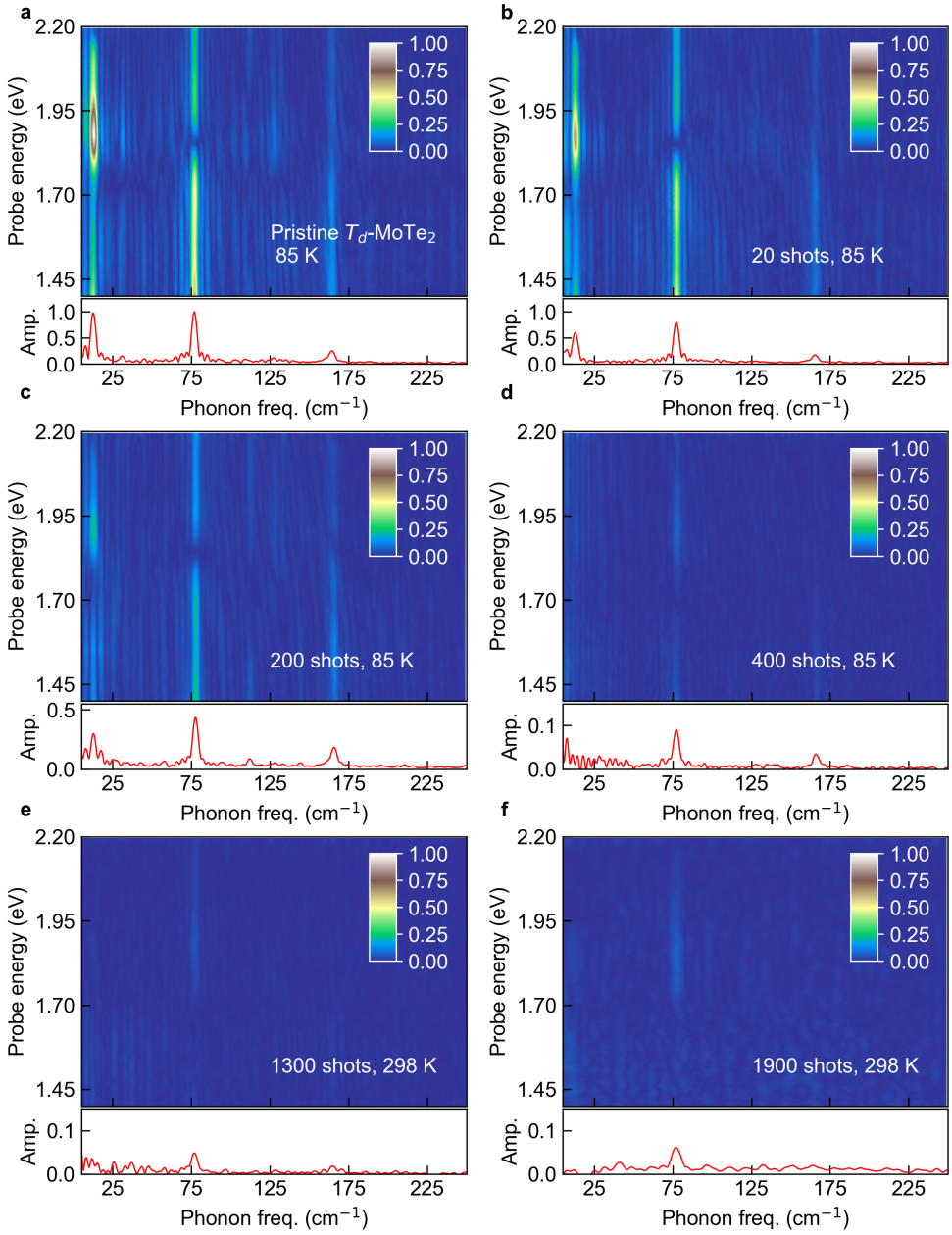

Figure 3.15: Fourier power spectra for laser irradiation test 3. (a) Pristine sample. (b-f) Same specimen following laser irradiation exposures. The temperatures and a cumulative number of laser shots employed in irradiation cycles are indicated in each panel. Irradiation exposures were carried out with $F = 4.6$ mJ·cm^{-2}. All tr-bb-TA measurements performed at 85 K, $F \approx 0.4$ mJ·cm^{-2}. There is a clear sign of sample degradation (see Figure 3.16).

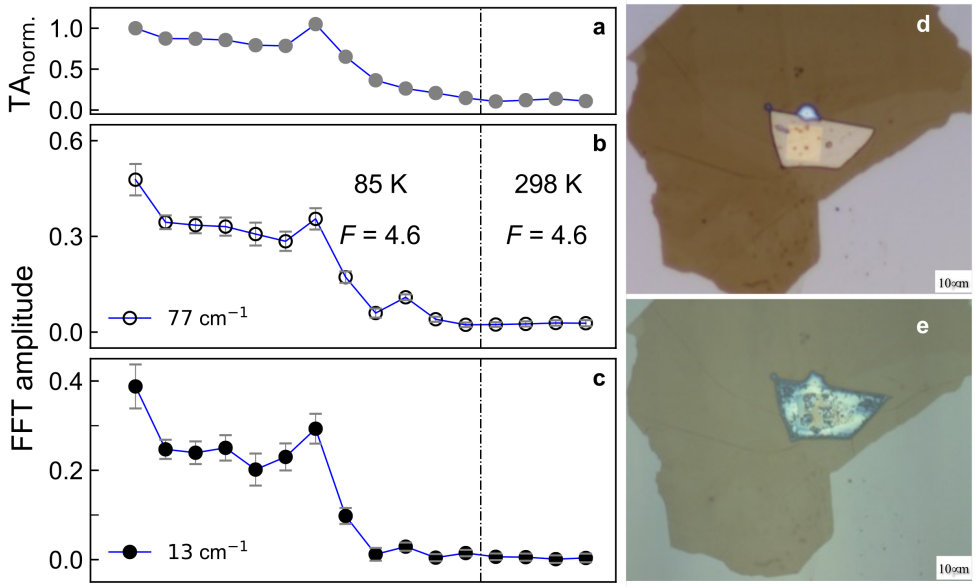

Figure 3.16: Laser induced changes as a function of the cumulative number of laser irradiation pulses for laser irradiation test 5. From left to right the number of cumulative laser shots is 0, 10, 20, 30, 40, 50, 100, 200, 250, 300, 400, 900, 1000, 1100, 1300, 1900. (a) Recorded maximum magnitude of TA signal, normalized by its initial value. (b) Fourier amplitude of the 77 cm^{-1} mode. (c) Fourier amplitude of the 13 cm^{-1} mode. The temperatures and incident fluences employed in irradiation exposures are indicated in the figure. All tr-bb-TA measurements were carried out at 85 K, $F \approx 0.4$ mJ·cm^{-2}. (d) Photograph of the pristine $1T'-MoTe_2$ film. (e) Photograph of the $1T'-MoTe_2$ film after laser damage (1900 shots).

Figure 3.17(a) exhibits an irradiation test performed on a 28-nm thick flake (See laser irradiation test A1 in Appendix B). The flake underwent several irradiation cycles while maintained at a base temperature of 200 K and at $F = 2.6$ mJ·cm^{-2}. This experiment approximately mimics the conditions for the 32-nm thick specimen in Figure 3.11 at $F \geq 2$ mJ·cm^{-2}, but in the limit of fewer laser irradiation shots. Each black dot represents an irradiation cycle, and the number corresponds to the number of cumulative laser shots. The tr-bb-TA experiments necessary to determine $\mathcal{A}(^1\mathrm{A}_1)$ were carried out at 100 K, i.e., the temperature of the sample was lowered and increased between irradiation cycles. The behavior of $\mathcal{A}(^1\mathrm{A}_1)$ reveals that the formation process of T^*, i.e., strain buildup appears to be quite stochastic in the limit of a few to several thousand shots. However, the fact that $\mathcal{A}(^1\mathrm{A}_1)$ follows a decreasing trend indicates the gradual generation of T^* with the increasing number of irradiation pulses.

Figure 3.17(b) presents the results obtained for a 35-nm thick flake exposed to a more extreme laser irradiation condition ($F = 6.5$ mJ·cm^{-2}) while maintained at a base temperature of 85 K (see laser irradiation test 2). Each of the first five irradiation cycles involved 10 laser shots. $\mathcal{A}(^1\mathrm{A}_1)$ was found to experience a decrease of $\sim 25\%$ from the first to the second irradiation round, remained nearly constant during the next three irradiation cycles, and suddenly approached the background level after the fourth exposure. We monitored the maximum magnitude of the TA signal as well as $\mathcal{A}(^2\mathrm{A}_1)$ during our tr-bb-TA experiments to discard the possibility of excessive sample damage before continuing with the next irradiation round. Note that $F = 6.5$ mJ·cm^{-2} is within the F_{th} range for film

damage. We did not observe sample degradation as evidenced in other laser irradiation tests (see laser irradiation test 3). The specimen was then warmed up to 298 K, exposed to 100 additional fs-laser shots with $F = 4.6$ mJ·cm^{-2}, and brought back to 85 K to perform tr-bb-TA measurements. The clear recovery of $\mathcal{A}(^1\mathrm{A}_1)$ not only confirms a decent level of

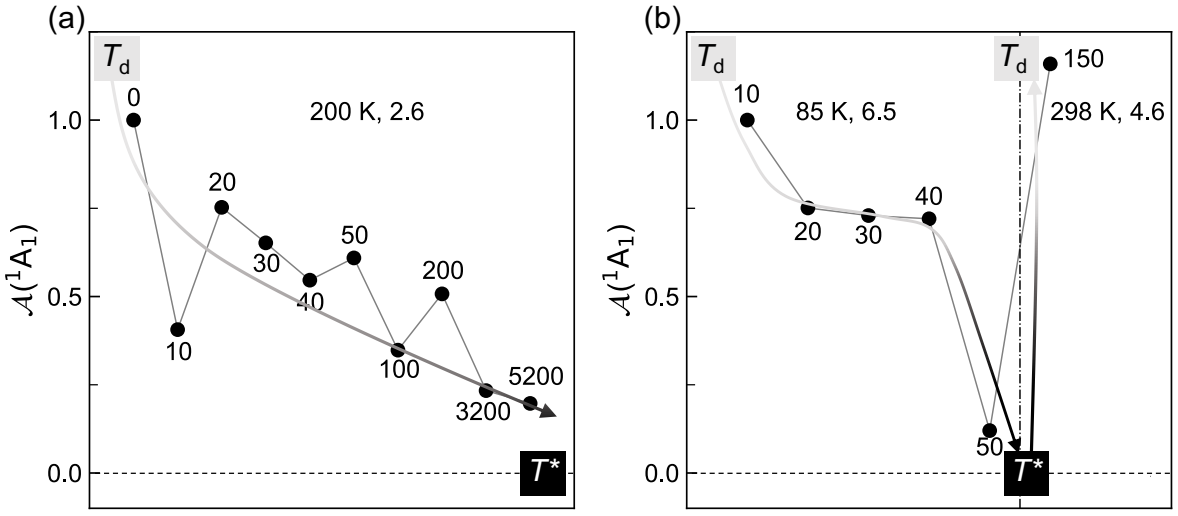

Figure 3.17: Formation of T^* under few-shots photoexcitation conditions and its reversion at room temperature to $1T'$ (i.e., T_d upon cooling). $\mathcal{A}(^1\mathrm{A}_1)$ as a function of the cumulative number of laser shots from left to right as indicated next to each data point. $\mathcal{A}(^1\mathrm{A}_1)$ has been normalized by the maximum magnitude of the TA signal, which served as an internal power reference (see Figure 3.14). (a) 28-nm thick flake irradiated at a base temperature of 200 K and $F \approx 2.6$ mJ·cm^{-2} (units of F were not included in panels). The sample was brought to 100 K after each irradiation cycle to run tr-bb-TA (b) Similar to (a) but for a 35-nm thick flake. For the first 50 shots the sample was kept at a base temperature of 85 K to perform each irradiation cycle at $F \approx 6.5$ mJ·cm^{-2}. Vibrational coherences were also measured at 85 K. The vertical dashed line indicates that the sample was brought to 298 K, irradiated by additional 100 shots at $F \approx 4.6$ mJ·cm^{-2} and cooled down to 85 K to measure again vibrational coherences at low F. Tr-bb-TA experiments were carried out at $F \approx 0.5$ mJ·cm^{-2}. The pump photon energy was $E_{\mathrm{pump}} = 2.4$ eV for both irradiation and tr-bb-TA measurements. The arrows are guides to the eye in the formation of and reversion from T^*.

sample integrity but also evidences that impulsive fs-laser irradiation at room temperature can be employed to transform T^* into the pristine-like $1T'$ phase which, upon cooling, transitions to the pristine T_d state.

Furthermore, in laser test 1 we also discovered that laser irradiation of the high-temperature $1T'$ state does not lead to the formation of T^*, see Figure 3.12. On the contrary, impulsive laser irradiation of the $1T'$ was found, in some cases, to slightly enhance $\mathcal{A}(^1\mathrm{A}_1)$, which is aligned with our hypothesis of laser-induced interlayer strain formation (see laser irradiation test in Appendix B). We think that the latter observation arises from the fact that pristine flakes carry some residual level of strain introduced during the transfer and h-BN capping processes of the $1T'$ $MoTe_2$ film. The formation of a strained state is also justified by *ex-situ* transport measurements that we performed as a function of temperature before and after laser transformation (see Figure 3.18). Measurements show that T^* experiences a hysteresis cycle comparable to that observed for the $T_d \rightarrow 1T'$ first order phase transition. This observation suggests that the structures of T^* at low and high temperatures may correspond to the strained T_d and $1T'$ phases, which can be denoted as T_d^* and $1T'^*$ respectively. However, this requires further investigation.

It is interesting to speculate about the mechanism driving the formation of T^*. Since this T^* was found to only develop upon fs-laser irradiation of the T_d state. This suggests that the process may be due to a frustrated or incomplete photoinduced $T_d \rightarrow 1T'$ phase transformation. This interpretation is in alignment with the small interlayer displacement unveiled in the same compound by FED[6] and the observation of a transiently hot

metastable T_d phase via bb-TR-spectroscopy in a bulk single crystal $MoTe_2$[112].

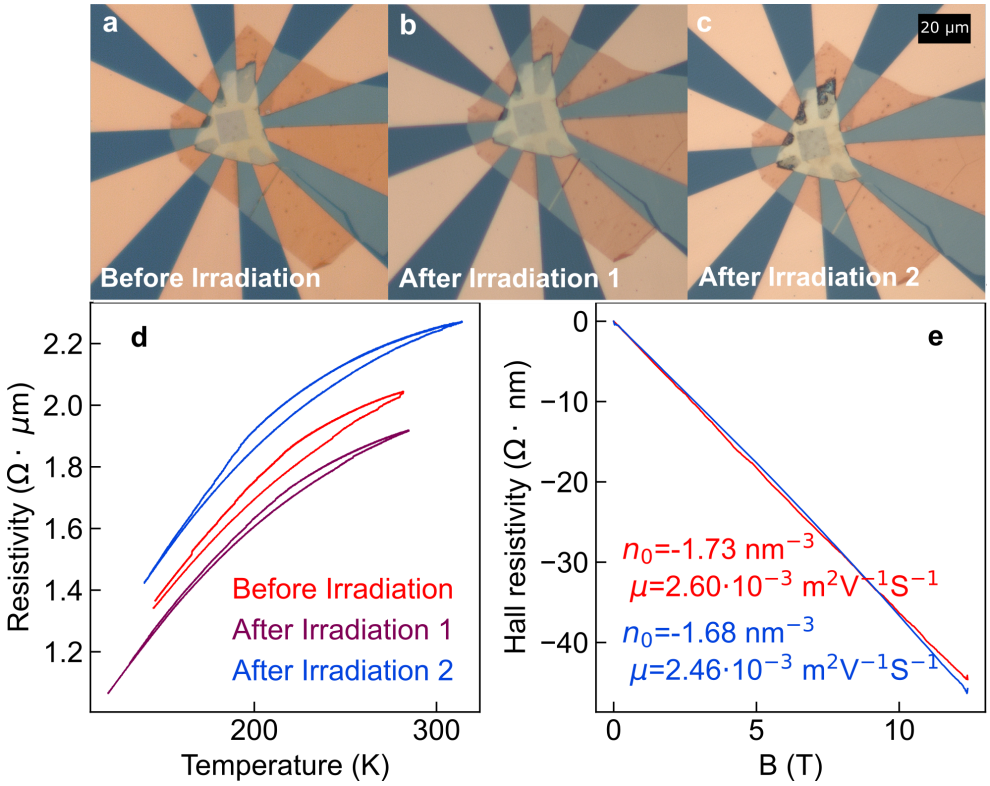

Figure 3.18: Resistivity measurements in a 30-nm thick $MoTe_2$ film supported by a Si frame with a central 10 μm × 10 μm Si_3N_4 window and Au electrodes in a star configuration. (a) Microscope image of a pristine flake. (b) Same sample as in panel a but after laser irradiation using 2.5 mJ·cm^2 at 85 K (5 minutes at 10 Hz). (c) Same sample as in panel b but after laser irradiation using 6.5 mJ·cm^2 at 85 K (5 minutes at 10 Hz). It is noteworthy to mention that small bubbles of inert gas trapped during sample preparation appear as small darker spots on the sample. In addition, some laser-induced damage to the sample on top of the Au electrodes becomes visible. This damage seems not to affect transport measurements largely. (d) Resistivity measurements were carried out in a four-wire scheme after each irradiation. (e) Carrier density (n_0) and mobility (μ) were determined by measuring the Hall resistivity at 150 K before (red) and after the third irradiation (blue). Red traces in panels d and e correspond to the pristine sample. The purple and blue traces correspond to the same flake after first laser irradiation (irrad. 1) at T = 85 K with 3000 pulses and F = 2.5 mJ·cm^2 and after second irradiation (irrad. 2) at T = 85 K, 3000 pulses and F = 6.5 mJ·cm^2, respectively.

Instead of a transient hot T_d state being observed in the photoinduced of a pristine single crystal of $MoTe_2$, such a persistent stain state in the thin film $MoTe_2$ points at the rate of cooling as a plausible reason for this distinct behavior. In both cases, a thin flake and a thick crystal, photoexcitation leads to the transient increase of the lattice temperature. In a thick crystal, this occurs from the surface and over the optical skin depth of the pump. The excess energy is quickly transferred to the underlying cold material on a timescale that often ranges from several hundreds of ns to a μs depending on thermal conductivity. In the case of our flakes, the optical penetration depth $\sim$ 30 nm ($E_{\text{pump}} = 2.4$ eV) is comparable to the $MoTe_2$ film thickness, and therefore flakes are excited quasi-homogeneously. The most important difference arises from the semi-freestanding character of the flakes, which substantially reduces the overall rate of thermal energy transfer to the substrate. Note that flakes would quickly but only partially thermalize with the thin h-BN and Si_3N_4 layers. However, the final transfer to the thick Si frame occurs along the plane of the layers (in-plane heat transfer) on a much longer timescale (i.e., typically in the order of several hundreds of μs). We believe that this extended period is necessary for the transiently hot lattice to be able to develop the observed persistent strained T^* state.

3.2.4 Conclusion

The formation of light-induced long-live states of matter and ultrafast PIPTs[158,159] are playing an increasingly important role in quantum materials and devices[26,160] designed to confer properties on demand[156]. Our study reveals that impulsive laser irradiation can be

utilized to induce or release interlayer strain that is likely arising from a frustrated (incomplete) photoinduced phase transformation. It provides the opportunity to extend such phenomenon to other 2D-TMDCs such as T_d-WTe_2 for which THz-light induced strained formation has recently shown to create a topologically distinct metastable phase[122]. Follow-up experiments could involve the implementation of THz-Raman and FED with transport measurement capabilities *in situ* to bring new perspectives for understanding the structural and electronic changes induced by impulsive laser irradiation in a growing research area of novel 2D materials.

Chapter 4

Characterization of elastic properties in TMDCs

In the previous chapter, we monitored photoinduced dynamical processes progressing within the timescale of tens of ps. If we span the time window to hundreds of ps, the same technique(s) could be used to monitor the CAWs which could characterize the elastic properties of our samples. The use of ultrashort laser pulses to generate ultra-high frequency ultrasound is known as picosecond ultrasonics which is one type of ultrasonics[161]. Picosecond ultrasonics was developed in 1980s to study CAWs in solids[162,163]. When an intense pump pulse excites a solid thermal stress results in the generation of CAWs that can be detected by weak probe pulses. The generation and detection of CAWs have been conducted with various solid-state materials, and it is increasingly applied to nanostructures due to its non-destructive feature. In this chapter, I will introduce our study of

CAWs in semi-metallic thin films of $MoTe_2$ and a semiconducting single crystal of SnS_2.

4.1 Generation and detection of coherent longitudinal acoustic waves in ultrathin $1T'$-$MoTe_2$ films

4.1.1 Introduction

Some fs-laser induced effects on $MoTe_2$ were discussed in chapter 3 and the photophysical properties of $MoTe_2$ were introduced in subsection 1.2.1. In this chapter, we utilize tr-bb-TA to monitor CAWs in ultrathin $1T'$-$MoTe_2$ films of varying thicknesses and at different temperatures.

The impulsive deposition of laser energy is known to create a temperature gradient normal to the surface, which leads to thermal stress and the release of elastic waves that propagate away from the heated interface. In the thin film sample, the generated strain bounces back and forth in the film[164]. The acoustic pulse causes a periodic modulation of the dielectric properties of the film. The period of the oscillations should vary linearly with film thickness seen in Equation 4.1 until the sample becomes thicker than the penetration depth[164].

$$\mathcal{T} = 2\,\ell/\upsilon \tag{4.1}$$

where $\mathcal{T}$ is the round trip period of an acoustic wave, υ is the sound velocity for acoustic waves, and ℓ is the sample thickness. We conducted tr-bb-TA spectroscopy to generate and

detect longitudinal acoustic waves in mechanically exfoliated $1T'$-$MoTe_2$ crystalline flakes of various thicknesses (4-30 nm). In the measurement, we plotted the $\mathcal{T}$ as a function of film thickness which gives us the slope of $2/\upsilon$ to determine υ. Similarly, the sound velocity in thin film of Bi_2Se_3[165] and MoS_2[77] were determined by the same approach.

4.1.2 Methodology

Samples were prepared by the team of Prof. Adam W. Tsen (University of Waterloo) and details are given in section 3.1. A photograph of a representative 10-nm $1T'$-$MoTe_2$ flake sample is shown in Figure 4.1(b). In all tr-bb-TA, flakes were impulsively excited by $\sim$ 100-fs optical pulses with a center wavelength of 520 nm, focused to about 300 μm in FWHM and with an incident peak fluence of 0.5 mJ·cm^{-2}. The optical penetration depth of 520-nm light is $\sim$ 30 nm. TA changes were probed by time delayed WL pulses $\sim$ 20 μm in FWHM at the sample position. The tr-bb-TA measurement details are described in section 2.2. It is noted that besides the CAWs, impulsive fs-optical excitation also drives the generation of coherent Raman modes as shown in Figure 4.1(c). It is much weaker but still well-presented in our tr-bb-TA spectra. This weaker signal corresponds to the $\sim$ 2.3 THz ($\sim$ 77 cm^{-1}) Raman modes present in both the T_d- and $1T'$-phases ($^2A_1$ and ^1A_g, respectively)[110,111]. The size of the pump pulse was much larger than the entire flake, thus ensuring a uniform sample excitation. Owing to our geometrical arrangement and the large size of the pump laser spot, our TA measurements were exclusively sensitive to longitudinal acoustic phonons, i.e., strain waves that propagate in the direction normal to

the plane of the layers.

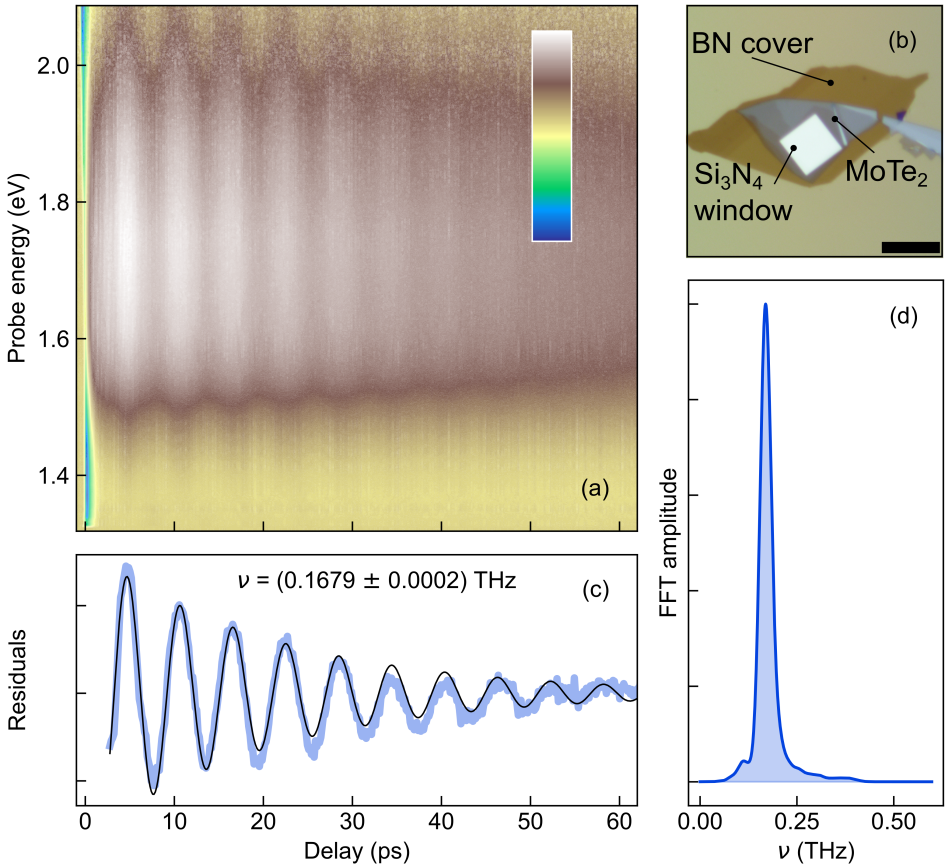

Figure 4.1: Data analysis scheme illustrated for the study of a 10-nm $1T'$-$MoTe_2$ film at room temperature, T = 295 K. (a) Raw tr-bb-TA spectra recorded as a function of the time delay with a time step of 150 fs. E_{pump} (λ = 520 nm) with F =0.5 mJ·cm^{-2}. (b) Photograph of the prepared flake following the transfer and h-BN capping. The square shape of the freestanding and transparent Si_3N_4 windows is clearly visible. (c) Blue trace: residuals obtained after averaging across the probed photon energy range and the removal of the electronic population background dynamics. Black trace: fit of the data by a damped sinusoidal function; see the text. (d) Frequency spectrum obtained by the FFT of residuals.

4.1.3 Results and Discussion

Figure 4.1(a) shows the raw tr-bb-TA spectra obtained for the 10-nm thick $1T'$-$MoTe_2$ sample. There is a clear modulation of the transient absorption signal across the probed spectral range. Figure 4.1(a) presents the residuals obtained after spectral averaging and the removal of the electronic population background dynamics. These steps are performed to improve the SNR and the confidence of the fitting and Fourier transform procedures. The value of $\mathcal{T}_L = \nu^{-1}$ and its error were calculated by fitting the residuals with a damped sinusoidal function $S(t) = A\exp(-t/\tau)\sin(2\pi\nu t + \varphi)$. Figure 4.1(d) also displays the frequency spectrum obtained via the FFT of residuals.

Figure 4.2 shows the dependence of $\mathcal{T}_L$ with flake thickness. A linear fit of the data with (0,0) intersect renders a value of $\upsilon_{L,295k} = 2990 \pm 90$ m s^{-1} at the room temperature. This is in reasonable agreement with the reported longitudinal sound velocity for the $2H$-$MoTe_2$ phase, which is $\upsilon_L = 3467$ m s^{-1} (exfoliated films)[166], $\upsilon_L = 3796$ m s^{-1} (molecular beam epitaxy-grown films)[166] and $\upsilon_L = 2800$ m s^{-1} (estimated from density functional theory calculations)[166,167]. We would like to mention that some discrepancy arising from different layer stacking configurations (i.e., $2H$ vs $1T'$) is expected. However, a relative change of $\sim$ 20% is indeed comparable to the observed variation in the elastic properties of our $MoTe_2$ flakes when the sample temperature is modified by 200 K, as displayed in Figure 4.3.

Recall that cooling below a critical temperature of $T_c \sim 250$ K[104] makes the $1T'$-$MoTe_2$ transition into the T_d-$MoTe_2$ Weyl semimetal candidate state[107–109] (see subsection 3.1.2). Here, the inset of Figure 4.3 displays the frequency spectrum obtained via FFT for a $\sim$

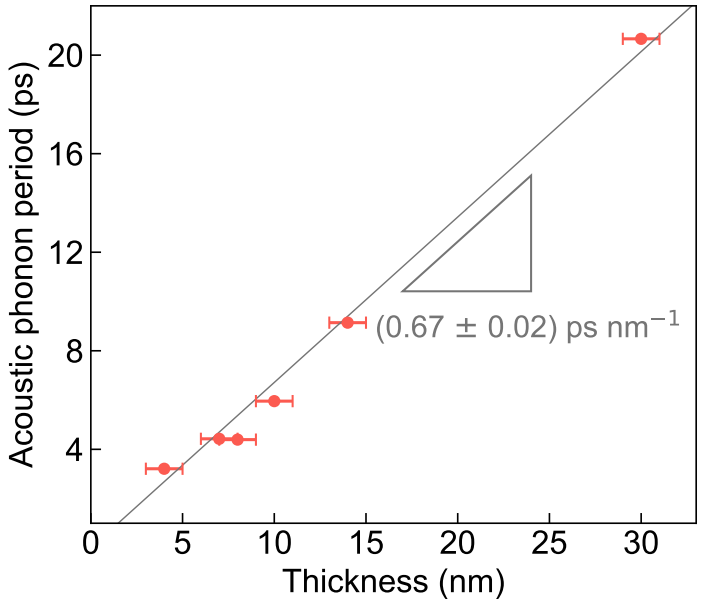

Figure 4.2: Acoustic wave period extracted from the tr-bb-TA measurements as presented in Figure 4.1 for flakes with different thicknesses. The solid trace is a linear fit of the data with (0,0) intersect. According to Equation 4.1, the slope (0.67 ± 0.02) ps nm^{-1} provides a value for $v_{L,295K}$ = (2990 ± 90) m s^{-1}. The error bars of film thicknesses are ± 1 nm. This is an upper limit that accounts for the fact that the thicknesses of $MoTe_2$ flakes are determined by measuring the changes in height on the h-BN protective layer which conforms to the features of the underlying $MoTe_2$ film. The error bars of $\mathcal{T}_L$ are smaller than the size of the symbol.

30-nm thick sample below and above T_c. The peak at ∼ 0.38 THz (13 cm^{-1}) corresponds to the characteristic $^1A_1$ interlayer shear mode of the low-temperature T_d-phase, which disappears in the high-temperature $1T'$-$MoTe_2$ state[103,166].

In order to investigate the effect of this first-order phase transition on the elastic properties of our exfoliated flakes, we performed tr-bb-TA measurements as a function of the sample temperature. According to $E_L = \rho\, v_l^2$, with the knowledge of the sound speed obtained from the tr-bb-TA we could acquire the elastic Young's modulus, E_L. Here, ρ is the density

of the material (7.67 g·cm^{-3})[168], and E_L has units of pressure. We obtained a value for $E_{L,295K} = 68 \pm 4$ GPa. Figure 4.3 illustrates the dependence of the normalized Young's modulus $E_L = E_{L,295K}$ with the temperature for two $MoTe_2$ samples with thicknesses of $\sim$ 12 nm and $\sim$ 30 nm. Given that a typical thermal expansion coefficient of 10^{-5} K would translate into negligible changes of ℓ (and ρ), it is possible to approximate $E_L/E_{L,295K} \approx$

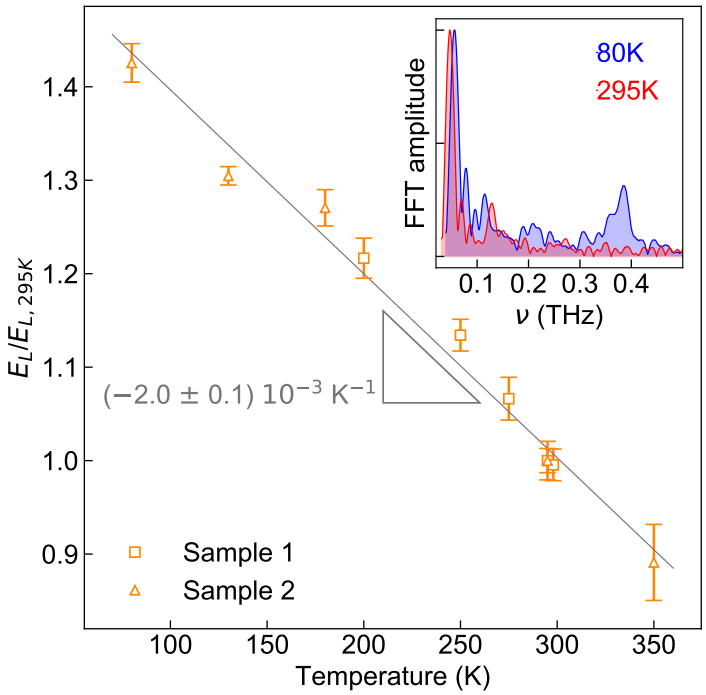

Figure 4.3: Temperature dependence of the normalized longitudinal Young's modulus approximated as $E_L/E_{L,295K} \approx (v/v_{295K})^2$ for two different $MoTe_2$ flakes with thicknesses of $\sim$ 12 nm (sample 1) and $\sim$ 30 nm (sample 2). Note that the $T_d - 1T'$ first order thermal phase transition is expected to occur at $T_c \sim 250$ K. We have not observed any drastic change in the elastic properties arising from this phase transition or variations in the film thickness in the explored range. Inset: Frequency spectrum obtained via FFT for sample 2 in its T_d- and $1T'$-states; blue and red, respectively. The mode at 0.38 THz (13 cm^{-1}) corresponds to the characteristic $^1A_1$ Raman interlayer shear mode of the T_d-phase.

$(\upsilon/\upsilon_{295K})^2$. The measured value of $E_{L,295K}$ in $1T'$-$MoTe_2$ was found to agree reasonably well with the out-of-plane stiffness constant of other layered materials such as graphite (36.5 GPa)[169] and $2H$-$MoTe_2$ (93.6 GPa, exfoliated flakes)[166]. However, Young's modulus of $MoTe_2$ displays a much more pronounced temperature dependence, i.e., $(-2.0 \pm 0.1) \times 10^{-3}$ K vs -3.0×10^{-4} K for graphite (estimated within the same temperature range from the modeled results from ref.[169]). This observation reflects the large anharmonicities of the lattice potential along the direction of the weakly interacting vdW cohesive forces in this highly anisotropic system.[170] Moreover, the linear behavior illustrated in Figure 4.3 suggests that the elastic properties of the films are not substantially altered, by either the aforementioned $T_d - 1T'$ structural transition or by the changes in the thickness within the explored $\sim$ 12- to 30-nm range. The latter statement is also consistent with the linear trend observed in Figure 4.1 despite the fact that the sub-12-nm thick $1T'$-$MoTe_2$ films were found to spontaneously transition to the T_d-phase by dimensionality effects.[106]

4.1.4 Conclusion

In conclusion, we demonstrated a reliable and noninvasive technique that can be used to determine the elastic properties of nm-thick, mm-sized materials. Especially, our approach for conducting tr-TA measurements on nm-thick, mm-sized $MoTe_2$ flakes relies on the implementation of homemade nano-fabricated optically transparent freestanding Si_3N_4 windows with dimensions that can be easily adjusted to match the small size of ultra-thin flakes typically produced by mechanical exfoliation.

4.2 Time-resolved broadband ISBS in single crystal SnS_2

4.2.1 Introduction

Light scattering by spontaneous thermal (or density) fluctuations in condensed media was first predicted by the French physicist Leon Brillouin in 1922[171]. Such density fluctuations propagate in the material at the speed of sound and, thus, can be seen as acoustic waves or phonons, which scatter light owing to these local variations of the materials refractive index. Spontaneous BS is, however, very weak, and it was not until the advent of intense light sources (i.e., lasers) that large scattering efficiencies, through a process known as stimulated Brillouin scattering (SBS)[97,172] have been observed. SBS is a nonlinear process in which density fluctuations are induced by the presence of the light field itself a phenomenon that is also referred to as electrostriction[173].

Furthermore, ultrashort laser pulses have made possible the study of impulsively generated coherent acoustic waves[173,174] bringing the investigation of SBS phenomena from the commonly exploited frequency domain to the time domain[175,176] and opening the doors to the generation and detection of coherent acoustic phonons reaching THz frequencies by Impulsive stimulated Brillouin scattering (ISBS)[77]. Perhaps, the most commonly known BS expression for a single phonon frequency or Brillouin frequency shift (ν_B) is given by

$$\nu_B = 2\,\upsilon\,\frac{n}{\lambda_0}\cos\phi \tag{4.2}$$

where υ is the speed of sound in the material, λ_0 is the wavelength of the light field in the vacuum (or air), and ϕ is the incident angle with respect to the acoustic wavefront.

Equation 4.2 and its modification to include the effect of the interface on the incident angle (i.e., Snell-Descartes refraction law) have been historically derived from phase matching or momentum conservation laws assuming the phonon relation $\nu_B = \frac{q_B\, v}{2\,\pi}$, with q_B being with a magnitude of the acoustic wave vectors[177]. However, the observable in our time-resolved transient reflectivity measurements (see scheme in Figure 4.4) arises from interference effects between the main reflected beam at the sample's surface (ray 1) and the secondary beam reflected at the moving acoustic or strain wave pulse front (ray 2). Note that the acoustic pulse effectively acts as a moving reflective interface for ray 2. In the strain propagation model (SPM)[164], for a bulk sample the period of oscillation is $T \cong \frac{\lambda_0}{2vn}$ for a back-scattered and normal incident configuration. T is the period of the observed periodic modulation in the time trace. and therefore renders an analogous expression to Equation 4.2 with $T = \nu_B^{-1}$. In subsection 4.2.1, we present an external of the SPM model, in which the effect of the interface becomes apparent via sample geometrical ray tracing and can be extended to a multilayer system. Moreover, we show angle- and time-dependent ISBS measurements performed in the model system of single crystal $2H$-SnS_2, and discuss the encountered limitations of our technique.

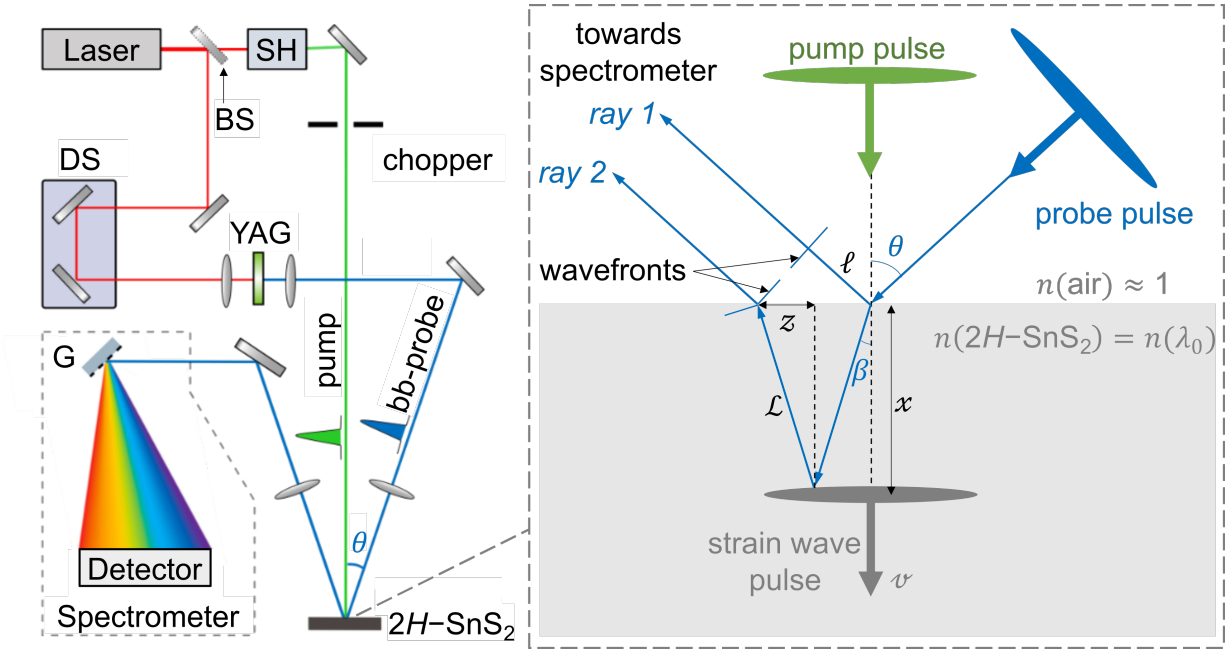

Figure 4.4: Experimental layout, and the closer view of the ray propagation geometry. Left: Experimental tr-bb-TR layout. Beam splitter (BS), second harmonic generator (SH), delay stage (DS), broadband (white light supercontinuum) probe beam, and Grating (G) as part of a dispersive spectrometer. Right: View of the ray propagation geometry. θ and β are the incident and internal probe beam angles, respectively. The pump pulse beam (p-polarized) is oriented perpendicularly to the interface and it is absorbed within the optical penetration-depth of ≈ 85 nm ($\lambda_{\text{probe}} = 400$ nm[42]) from the interface, generating an acoustic pulse that travels into the bulk of the material. This acoustic pulse changes the dielectric properties of the medium as it propagates, effectively acting as a moving reflective interface for *ray* 2. In this scheme, the wavefront of *ray* 1 and *ray* 2 are in phase, and therefore the intensity measured in the detector is enhanced by constructive interference. The probe is p-polarized to enhance the refracted fraction of the beam in order to maximize the transient changes.

4.2.2 Methodology

The scheme shown in Figure 4.4 illustrates a situation of constructive interference in which the wavefronts of *ray* 1 and *ray* 2 are in phase, and the optical path difference between

these two rays then corresponds to

$$\mathbb{N}\,\lambda_0 = 2\,n\,\mathcal{L} - l = 2\,n\,\mathcal{L} - 2\,\mathcal{L}\sin\beta\sin\theta \tag{4.3}$$

and according to Snell-Descartes' refraction law leads to

$$\mathbb{N}\,\lambda_0 = 2\,n\,\mathcal{L} - 2\,n\,\mathcal{L}\sin^2\beta = 2\,n\,\mathcal{L}\cos^2\theta \tag{4.4}$$

where n is a function of λ_0 and $\mathbb{N}$ is an integer multiple. Note that $x = \mathcal{L}\cos\beta = \upsilon\,\mathbb{N}\,T$. We therefore obtain by substitution of $\mathcal{L}$ into Equation 4.4,

$$2\,n\,\upsilon\,T\cos\beta = \lambda_0 \tag{4.5}$$

Equation 4.5 is analogous to the Brillouin frequency shown above as Equation 4.2; however, it becomes clear that β corresponds to the internal angle, which an is an important observation owing to the fact that the effect of the interface is often overlooked[178,179]. Since we cannot directly measure β in our experiments, it is more convenient to rewrite Equation 4.5 as a function of the external incident angle β making use of the Snell-Descartes' law once again,

$$2\,\upsilon\,T\sqrt{n^2 - \sin^2\theta} = \lambda_0 \tag{4.6}$$

Equation 4.6 is in agreement with previous formulae derived from phase matching and phonon dispersion relations[180,181]. Hence, T (or ν_B) is obtained, as a function of λ_0, from

the oscillatory component observed in our time-dependent transient reflectivity traces. It is noted that we have derived Equation 4.6 using the standard beam propagation model that considers only n for ray tracing (direction of the refracted beam) whereas the effect of k (imaginary part of the refractive index) is included as an attenuation factor acting on the amplitude of the refracted beam, i.e., *ray* 2. As a rule of thumb, if $k/n < 0.07$ the standard method works well[182], which is the case for our range of detected λ_0.

The sample, a single crystal of $2H$-SnS_2, was purchased from HQ Graphene and characterized via Raman measurements and XPS. The experimental layout of tr-bb-TR is shown in Figure 4.4 (a), and a detail of our transient spectroscopic setup is introduced in section 2.2. The $2H$-SnS_2 crystal was excited by $\approx$ 100-fs pump pulses centered at a photon excitation energy of $E_{\text{pump}} = 3.1$ eV (wavelength of $\lambda = 400$ nm) with an approximate incident fluence of 0.5 mJ·cm^{-2}. The probe beam and pump beam spot sizes at the crystal's surface were approximately 50 μm and 300 μm in FWHM, respectively. The repetition rate of the laser system was 6 kHz and tr-bb-TR spectra were obtained by modulating the pump beam with a mechanical chopper at 500 Hz. $2H$-SnS_2 is stable under ambient conditions and has an indirect band gap of $\approx$ 2.3 eV and a direct band gap at room temperature of $\approx$ 2.4 eV[42]. Pumping above the band gap removed the need to introduce a commonly employed transducing metallic layer and provide a well-defined optical boundary. Note that the addition of a metallic film transducer would require our model to include the effect of such a lossy medium on the path of the refracted *ray* 2. In our experimental geometrical arrangement (Figure 4.4) the pump beam was oriented perpendicular to the surface of the

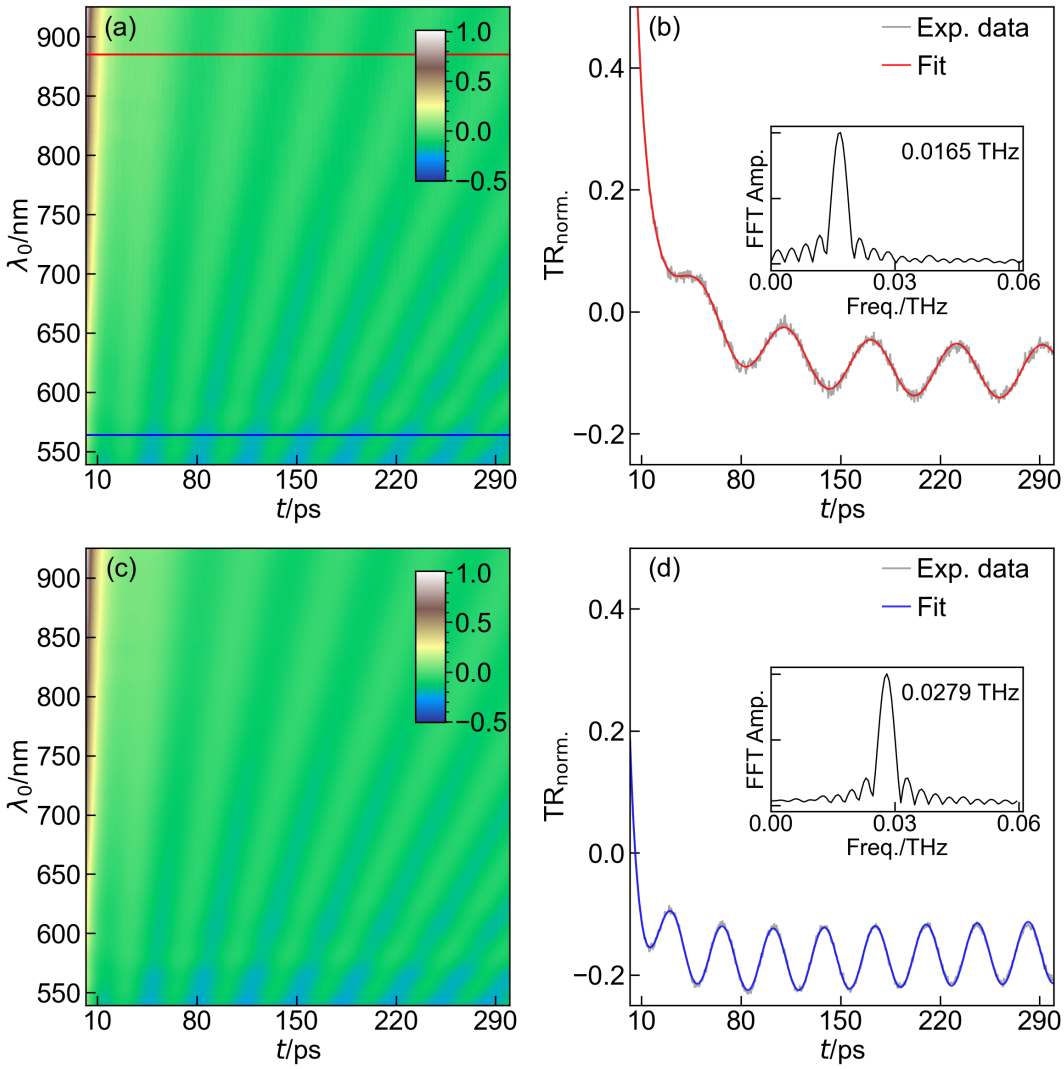

Figure 4.5: Data analysis protocol illustrated for the study of a single crystal of $2H$-SnS_2 at 295 K, with $\theta \approx 30°$. (a) Raw tr-bb-TR spectrum collected with time step of 500 fs. (b, d) The gray traces correspond to normalized raw time-dependent tr changes at fixed $E_{probe} \approx 1.9$ eV (b) and $E_{probe} \approx 1.4$ eV (d). The positions of these slices are indicated in panel (a) with the same colors (blue and red) implemented to show the results from the fits using Equation 4.7. The frequency spectra obtained from FFT analysis of the oscillatory components are shown as insets. (c) Model fitting result obtained by combining all fits as a function of E_{probe}. The similarity between panels (a) and (c) is remarkable.

crystal whereas the probe beam impinged the interface at a given incident angle θ. The tr-bb-TR measurements were performed at room temperature, 295 K, at three different incident probe beam angles, $\theta = \{15°, 30°, 45°\}$.

4.2.3 Results and Discussion

Figure 4.5(a) shows a raw tr-bb-TR spectrum obtained for $\theta \approx 30°$. Two time-dependent TR traces obtained by slicing the spectrum at two different values of λ_{probe} are shown in Figure 4.5(b) and (c) for illustrative purposes. The main feature associated with the aforementioned ISBS process is the observed long-lived oscillation, which is superimposed on a varying background that emerges from the dynamics of photoexcited carriers in $2H$-SnS_2. We determined ν_B at each λ_0 by implementing the following fitting model:

$$S(t) = A_1\, e^{\frac{-(t-t_1)}{\tau_1}} + A_2\, e^{\frac{-(t-t_2)}{\tau_2}} + A_3\, e^{\frac{-(t-t_3)}{\tau_3}} \sin(2\,\pi\,\nu_B\,t + \varphi) + C \tag{4.7}$$

where $\tau_{j=1,2,3}, A_{j=1,2,3}, t_{j=1,2,3}$, φ, and ν_B are fitting parameters; $\tau_{j=1,2,3}$ are time constants, $A_{j=1,2,3}$ are amplitudes, $t_{j=1,2,3}$ are time origins, φ is a phase relative to t_3, and C is an offset. The damping factor that accompanies the *sine* function accounts for decoherence effects acting on the propagating acoustic pulse as well as the weak absorption suffered by *ray* 2 at probing wavelengths approaching the band gap of hematite, see Figure 4.6(a). The Larger standard deviations obtained at low E_{probe} are due to the lower intensity of our broadband probe pulse in this spectral region. Figure 4.5(d) shows the result gathered from our automated model fitting procedure, which appears to the naked eye to be identical

to our raw tr-bb-TR spectrum presented in Figure 4.5(a). As can be clearly seen in our tr-bb-TR spectrum, and in accordance with Equation 4.7, T increases with increasing λ_0 (decreasing E_{probe}).

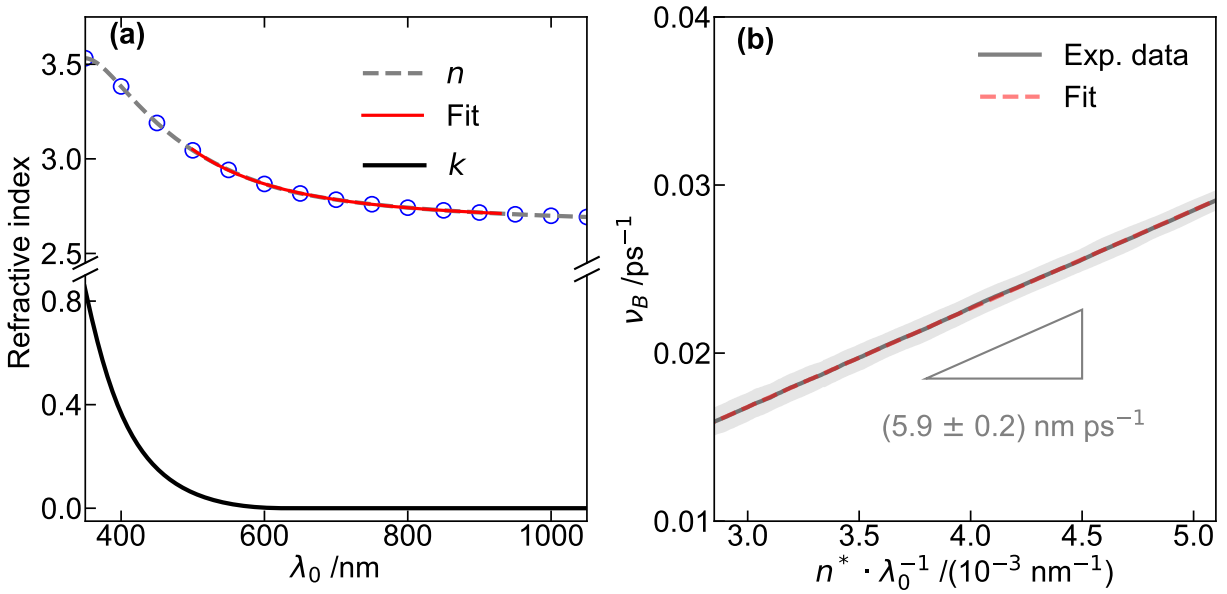

Figure 4.6: Data analysis protocol illustrated for the study of a single crystal of $2H$-SnS_2 at 295 K, with $\theta \approx 30°$. (a) Real (n) parts of the refractive index of $2H$-SnS_2 as a function of wavelength[42]. (b) The dark gray trace corresponds to the plot of $\nu_B(\lambda_0, \theta \approx 30°$ as a function of $n(\lambda_0)^* \cdot \lambda_0^{-1}$ with $n(\lambda_0)^* = \sqrt{n(\lambda_0)^2 - \sin^2(\theta = 30°)}$. The red trace represents a linear fit of the data, which yields a slope of (5.8 ± 0.2) nm ps^{-1} and v = (2.9 ± 0.1) km s^{-1}, with the error originating mostly from the uncertainty of our incident angle measurement that was estimated to be ± 5°. The light gray shadow represents the error bars in standard deviation of $\nu_B(\lambda_0, \theta \approx 30°)$ as obtained from fittings using Equation 4.7.

Figure 4.6(a) presents values of the real, $n(\lambda_0)$, and the imaginary parts, $k(\lambda_0)$, of the index of refraction of single crystal $2H$-SnS_2. The experimental values of $n(\lambda_0)$ were fitted within the wavelength interval of interest using the Cauchy relationship, $n(\lambda_0)$ =

$A + B/{\lambda_0}^2 + C/{\lambda_0}^4$. This fitting procedure was performed as a means to obtain a smooth dependence of n as a function of λ_0. According to Equation 4.6 and provided that the values of $n(\lambda_0)$, θ, and $\nu_B(\lambda_0)$ are known; υ can be obtained from the slope of the linear regression of $\nu_B(\lambda_0) = 2\,\upsilon\,n(\lambda_0) * \lambda_0^{-1}$ with $n(\lambda_0)^* = \sqrt{n(\lambda_0)^2 - \sin^2\theta}$. The observed linear trend rules out possible instrument calibration issues[178,183,184] and provides confidence to our value of υ. The fitting result is shown in Figure 4.6(b). We determined a slope of 5.8 ± 0.2 nm ps^{-1}. The slope renders a value for the longitudinal sound velocity of $\upsilon = 2.9 \pm 0.1$ km s^{-1}. Very similar results were obtained from our experiments at $\theta = \{15°, 45°\}$, which provided the values of $\upsilon = 2900 \pm 100$ m s^{-1} and $\upsilon = 2950 \pm 100$ m s^{-1}, respectively. Our values are in reasonable agreement with that determined indirectly by Mnari et al.[44], $\upsilon = 3550$ m s^{-1}, who had to model acoustic microscopy data owing to substrate effects arising from their SnS_2 films deposited on Pyrex glass. In the experiment, the velocity they measured were the average values between the velocities in the layer and in the substrate. The velocity of SnS_2 was calculated by varying the initial values of sound velocities (used as data) to refine the model through iterations by minimizing the difference between the theoretical velocities deduced from modeling and those obtained experimentally[44]. The errors in their reported values were not mentioned.

In order to explore the possibility to determine υ without prior knowledge of $n(\lambda_0)$ or to conversely obtain $n(\lambda_0)$ without prior knowledge of υ, we performed additional measurements at $\theta \approx 15°$ and determined $\nu_B\,(\lambda_0, \theta \approx 15°)$ as indicated above in Figure 4.6 for $\nu_B\,(\lambda_0, \theta \approx 30°)$. The combination of measurements at two different incident probe angles

(θ_1, θ_2) provides the following expression which is no longer dependent on $n(\lambda_0)$:

$$\nu_{B,1}^2 - \nu_{B,2}^2 = 4\,v^2\,(\sin^2\theta_2 - \sin^2\theta_1)\,\lambda_0^{-2} \tag{4.8}$$

where $\nu_{B,k=1,2} = \nu_B\,(\lambda_0, \theta_{k=1,2})$. Figure 4.7 shows the plot of $(\nu_{B,1}^2 - \nu_{B,2}^2)$ as a function of ${\lambda_0}^{-2}$. The dashed red line corresponds to a linear fit of the data, which provides a slope of $\approx$ 5.4 nm^2 ps^{-2}, and therefore a value of $\upsilon \approx$ 2.7 km s^{-1}. The light gray shadow in Figure 4.7 represents the error bars of $(\nu_{B,1}^2 - \nu_{B,2}^2)$ in standard deviation, which we found to be governed by the relative error of $\nu_{B,k} \approx$ 1 - 2% obtained from the model fitting (Figure 4.5).

Our previous study in Hematite[185] also showed such huge error bars. We estimate a reduction in the relative error of $(\nu_{B,1}^2 - \nu_{B,2}^2)$, and therefore the relative error υ, by a factor of $\approx$ 3.5 when considering the two possible extreme scenarios, $\theta \approx 0°$ and $\theta \approx \theta_B \approx 70°$ (θ_B is the Brewster's angle). In addition, $2H$-SnS_2 and Hematite both have a large average value of $n \approx 2.8$ that translate into relatively small variations of the internal angle β as a function of θ, imposing additional constraints to the observed frequency difference.

4.2.4 Conclusion

To summarize, we demonstrated a robust all-optical and non-destructive technique that can be implemented to determine the elastic properties of brittle 2D layer materials like $2H$-SnS_2 which may not withstand conventional tension and compression tests. We also

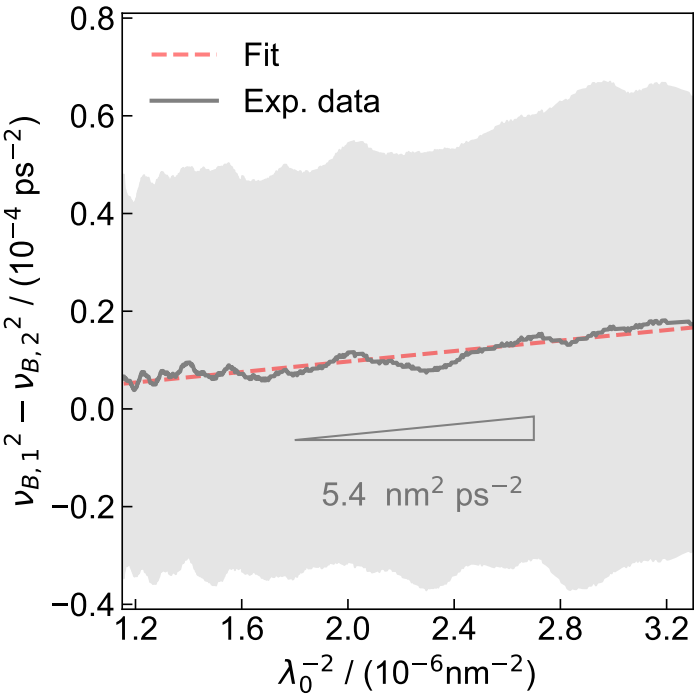

Figure 4.7: Determination of v without prior knowledge of $n(\lambda_0)$. The dark gray trace represents the plot of $\nu_{B,1}^2 - \nu_{B,2}^2$ as a function of ${\lambda_0}^{-2}$, with $\nu_{B,1} = \nu_B(\lambda_0, \theta \approx 30°)$ and $\nu_{B,2} = \nu_B(\lambda_0, \theta \approx 15°)$.The red trace corresponds to a linear fit of the data, which yields a slope of 5.4 nm^2 ps^{-2} and a value of $v \approx 2.7$ km s^{-1}. The light gray shadow represents the error in standard deviation.

showed a simple derivation of the ISBS–SPM formula by the ray tracing method and demonstrated an approach capable of providing information on both elastic and optical properties of transparent media. Additionally, our all-optical method and analysis protocol were found to provide robust results, benefiting from the implementation of a broadband probe

Chapter 5

Radiative dynamics in bilayer MoS_2/WS_2 heterostructure

In chapter 3 and chapter 4, I presented the results obtained through the implementation of tr-bb-TA and tr-bb-TR approaches for the study of interlayer dynamics, photoinduced transformations and elastic properties of some relevant TMDCs. In this chapter, I will show some preliminary results attained by fs-PLup during the investigation of the light emission dynamics from Rhodamine B in ethanol as a known model system and from a MoS_2/WS_2 bilayer heterostructure.

5.1 Motivation

As introduced in subsection 1.1.2, TMDCs show strong PL when thinned down to a monolayer due to the crossover from an indirect to a direct band gap. In addition to the change of thickness[10], PL properties can be tuned via the implementation of strain[186], electric gating[187], doping and defect engineering[188]. Moreover, owing to the giant excitonic oscillator strength of monolayer TMDCs radiative decay times in the range of few hundreds of fs to several ps are anticipated[63,64,189,190]. A fundamental understanding of the radiative recombination mechanism and the carrier dynamics in semiconducting single and few-layer TMDCs is thus critical to promote their application and improve the efficiency of optoelectronic devices.

Tr-PL studies of monolayer semiconducting TMDCs date back to 2011 and relied on the implementation of streak cameras (see section 2.5). Korn et. al.[190] reported tr fluorescence measurements in monolayer MoS_2 at various temperatures in the range of 4 K to 300 K. They found that the radiative recombination at low temperature happens on the ps timescale with a long-lived component that grows with increasing sample temperature. Similar observations were reported by Robert et. al[64] in 2016 during the investigation of monolayer $MoSe_2$ and WSe_2. However, the time resolution in these two studies was limited to ~ 5 ps. In the former[190], due to the speed of the streak camera, and in the latter, owing to the pulse width of the pump pulse used[64].

Taking on the challenge of monitoring PL signals with sub-ps resolution and exceptional spectral resolution, I developed a homemade fs-PLup with the support of Dr. Kostyantyn

Pichugin (Research Associate, UeIL) who wrote the data acquisition software for both the fs-PLup and tr-bb-TA/tr-bb-TR setups.

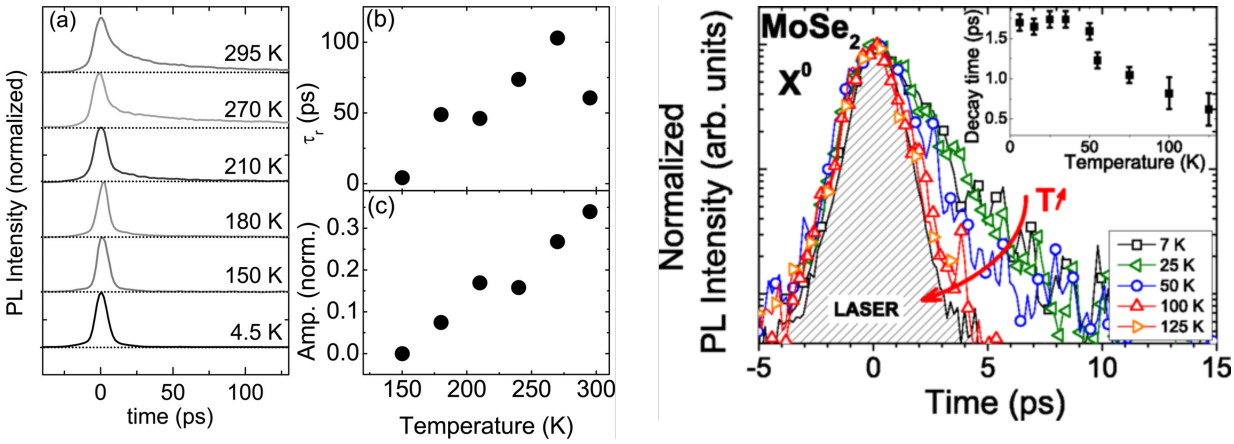

Figure 5.1: Tr-PL measurements of monolayer TMDCs. Left panel: (a) Normalized tr-PL traces measured on the monolayer MoS_2 flake for different temperatures. (b) Slow component of photocarrier recombination, τ_r, as a function of temperature. (c) Amplitude of the slow component of the tr-PL traces as a function of temperature. Reproduced from reference[190] with permission from the American Institute of Physics. Right panel: Temperature dependence of the exciton photoluminescence dynamics for the $MoSe_2$ monolayer. Reproduced from reference[64] with permission from the American Chemical Society.

5.2 Fs-PLup in MoS_2/WS_2 heterostructure

In chapter 2, I mentioned the advantages of fs-PLup, i.e., higher temporal resolution than streak cameras and better SNR than ultrafast OKE. Herein, I will show the layout of our fs-PLup, the characterization of its instrument response, and some preliminary tr-PL results.

5.2.1 Methodology

Sample preparation and characterization

Monolayer MoS_2 was grown on c-plane sapphire using the metallo-organic CVD (MOCVD) method[191]. Then monolayer WS_2 was grown on top of the MoS_2 layer to form the bilayer MoS_2/WS_2 heterostructure. Figure 5.2 shows a photograph of the coated sapphire wafer, microscope images, and characterization data. The bilayer TMDC heterostructure was provided and characterized by the group of Prof. Dr.-Ing. Andrei Vescan, RWTH, Aachen University, Germany. An SEM image and its corresponding atomic-force microscopy (AFM) image are shown in Figure 5.2(d) and its insert, respectively. Figure 5.2(e, f) show the Raman spectrum and PL spectrum. In the PL spectrum, two peaks with maxima at the wavelength of $\sim$ 625 nm and $\sim$ 670 nm correspond to A excitons of WS_2 and MoS_2, respectively. The peak at $\sim$ 700 nm corresponds to the sapphire.

Femtosecond PL up-conversion setup

A photograph of the experimental setup is shown in Figure 2.16. In the fs-PLup experiments, we utilized excitation pulses with a wavelength of $\lambda = 532$ nm and an incident fluence of 0.5 mJ·cm^{-2} to generate PL. The PL was up-converted with the 1030 nm gate pulse with a fluence of 15 mJ·cm^{-2}. The spot size of the excitation pulse at the sample was about 250 μm (FWHM) whereas the fluorescence spot size at the SFG crystal was a few mm. The gate beam spot size at the SFG crystal was set to 500 μm (FWHM). Tr-PL

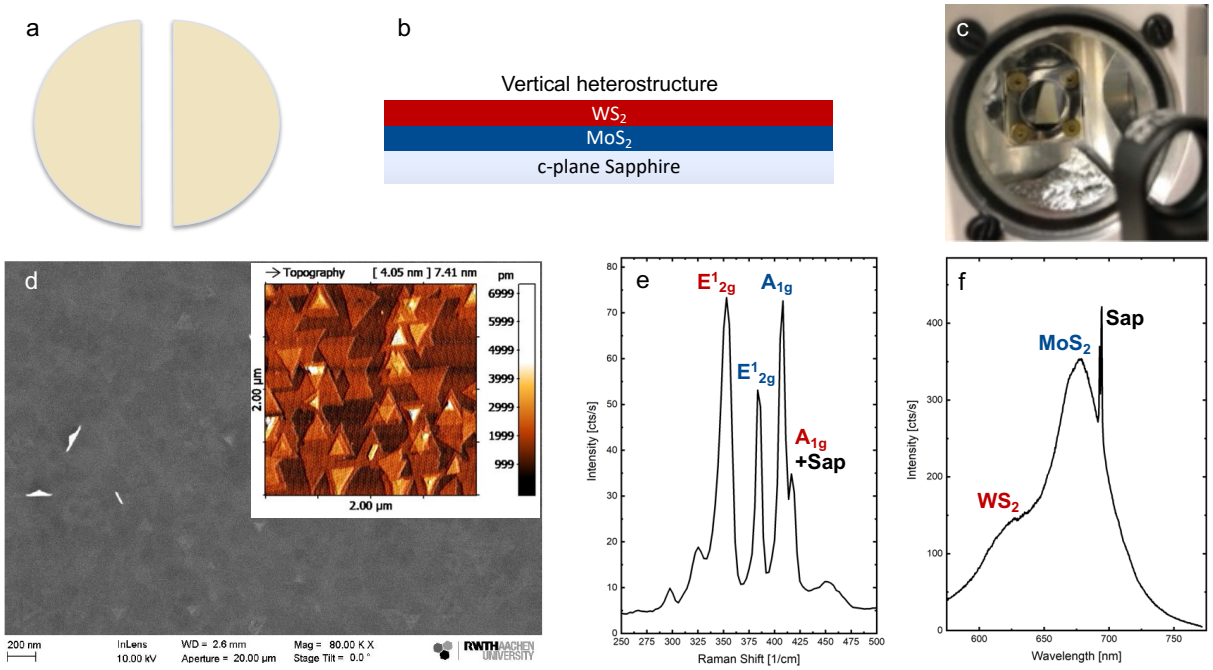

Figure 5.2: Characterization of MoS_2/WS_2 heterostructure. a. The image of MoS_2/WS_2 heterostructure on sapphire, and the photography of sample mounted in the cryostat in c. b. Schematic of vertical view of the heterostructure. Characterization data of the heterostructure in d. SEM and AFM images, e. Raman spectrum, and f. fluorescence spectrum.

spectra were obtained as a function of t via the implementation of a delay stage on the gate beam path. The main challenge in our fs-PLup studies is that the up-converted PL and PL signals from semiconducting 2D-TMDCs cannot be seen by the naked eye. Therefore, I used the organic dye Rhodamine B dissolved in ethanol as a standard model system to align the optical components. Once the setup was aligned, I replaced Rhodamine B with the bilayer sample. Since the generated PL approximately follows the same optical path only minor adjustments to the optical configuration were necessary for signal optimization. To mimic the expected up-converted PL signal and find the temporal overlap,

I set the excitation wavelength $\sim$ 600 nm and use this beam to achieve SFG and perform further alignment since the up-converted signal was visible on a fluorescence card. I finally performed fs-PLup experiments on Rhodamine B and bilayer MoS_2/WS_2 heterostructure. Some important experimental considerations are introduced below.

1. **IRF and time zero determination.** The IRF and time zero were determined by cross-correlation between the excitation beam and the gate pulse. By removing the cardboard between two OAP-mirrors (see subsection 2.5.3), the excitation beam follows the same optical path as fluorescence and meets with the gate pulse at the SFG crystal. The cross-correlation signal is plotted in Figure 5.3, and the FWHM is $\sim$ 240 fs. This value was found to depend on the pump wavelength and is typical $\sim$ 200 fs.

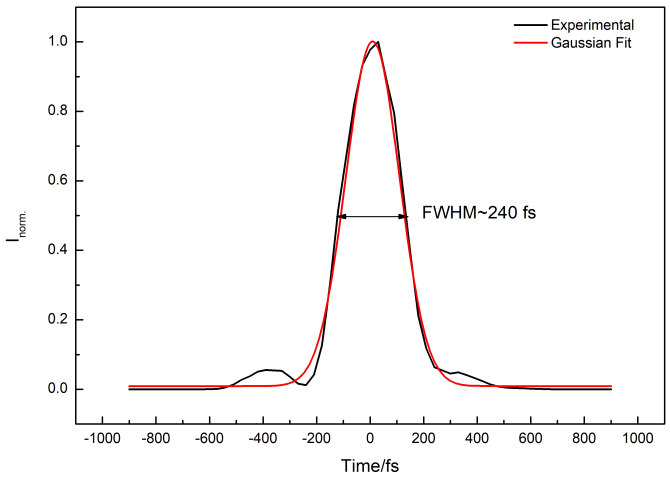

Figure 5.3: Cross-correlation between the scattered excitation pulse with the wavelength of 575 nm and the gate pulse with the wavelength of 1030 nm. The FWHM for the cross-correlation trace is $\sim$ 240 fs.

2. **Stray Light and detection of up-converted photons.** Since the signal level of up-conversion signals is normally low, the background signal should be kept as low as possible. Therefore, the fs-PLup measurement should normally be taken with the room lights off. In addition, the power of the PHAROS laser system should be locked to minimize fluctuations. To detect the weak SFG signal, the PMT was set at the highest voltage of 1100 V. At this point, it is crucial to block as much as possible the PL signal and the gate and its SHG from entering the spectrometer. Scattered light from these beams will contribute to the background noise. Since we use a quasi-collinear configuration, the up-converted signal, the gate, and the fluorescence pulse follow slightly different directions. Thus, an aperture placed right after the SFG crystal was used to select the up-converted beam and block the other two. A quasi-collinear configuration is required to achieve good SFG efficiency.

5.3 Preliminary results and future work

Next, the PL spectrum of the bilayer heterostructure was measured using our fs-PLup setup without introducing gate pulse. As can be seen in Figure 5.4, two pronounced emission peaks at $\sim$ 655 nm and $\sim$ 605 nm correspond to the A and B exciton emission peaks of MoS_2[54,56]. The emission peak at $\sim$ 630 nm corresponds to the A exciton emission peak of WS_2[54,56]. Note that we conducted PL measurements with a large excitation beam spot size ($\sim$ 250 μm in FWHM) compared to that of a Raman microscope[54,56]. Therefore, we not only collected signal from the MoS_2/WS_2 heterostructure but also from monolayer MoS_2 owing to the partial coverage. The small peak at $\sim$ 695 nm corresponds to the sapphire

substrate as also shown in Figure 5.2.

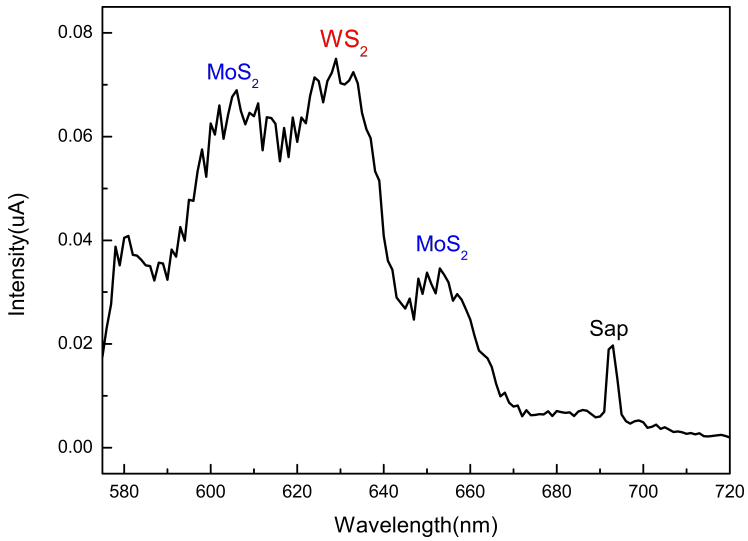

Figure 5.4: Photoluminescence spectrum of MoS_2/WS_2 bilayer. The bilayer sample is excited by vertically polarized light of 532 nm with a beam spot size of FWHM $\sim$ 250 μm. Two pronounced emission peaks at $\sim$ 655 nm and $\sim$ 605 nm correspond to the A and B exciton emission peaks of MoS_2[54,56]. The emission peak at $\sim$ 630 nm corresponds to the A exciton emission peak of WS_2[54,56]. The small peak at 695 nm corresponds to the sapphire substrate.

The tr-PL spectrum is shown in Figure 5.5 panel (a), and a temporal trace (slice) obtained at wavelength of 390 nm is displayed in panel (b). We observed that the electron-hole recombination dynamics is much faster than the previously reported for the monolayers of these TMDCs[62–64,190,192]. We also observed a huge 'chirp' from the emission dynamics of the bilayer sample. To confirm that such a huge 'chirp' is not caused by dispersion in our fs-PLup setup I collected the tr-PL spectra of Rhodamine B. Figure 5.6 shows the fluorescence of Rhodamine B in ethanol and its up-converted signal. There is no detectable chirp in the tr-PL of Rhodamine B, which seems to indicate that the large 'chirp' observed from the bilayer sample may arise from an actual photophysical phenomenon. In the tr-PL

spectral map of the bilayer heterostructure we could see that the emission peak is centered around 390 nm ($\sim$ 627 nm), and therefore could be assigned as A exciton emission from WS_2.

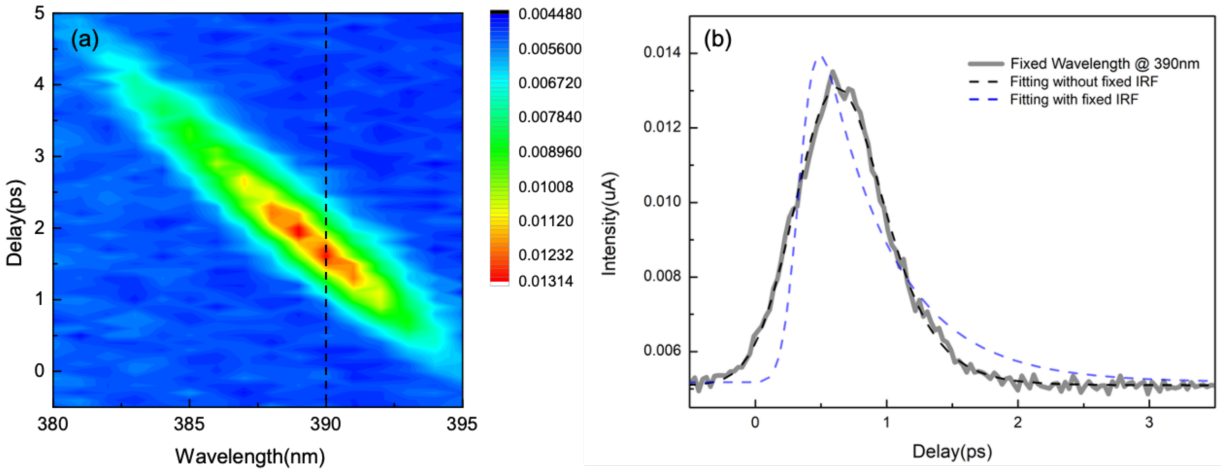

Figure 5.5: Tr-PL spectrum of MoS_2/WS_2 bilayer. The bilayer sample is excited by vertically polarized light of 532 nm with an incident fluence of 0.5 mJ·cm^{-2}, and the fluence of vertically polarized 1030 nm gate pulse is 15 mJ·cm^{-2}. (b) is showing the raw data and the fitting results. The thick gray line is the slice of PL dynamic at the wavelength of 390 nm. To obtain the time constant, τ, we fitted the raw data by applying Equation 2.9 with and without fixed σ in the IRF (FWHM $\approx 2.35\sigma$). The black dash line is the fitting result without fixed IRF (FWHM= 670 fs) which gave me $\tau = 250$ fs. The blue dash line is the fitting curve with fixed IRF (FWHM=240 fs) and $\tau = 530$ fs. When collecting the up-converted signals I set the spectrometer entrance and exit slits as 1 mm/1 mm which results in a low spectral resolution. Such low spectral resolution and the large 'chirp' might broaden the signal in the time dominant. Therefore, with characterized IRF the fitting curve cannot well present the up-converted signal.

I implemented the deconvolution procedure introduced in section 2.1 to extract the decay time. Here I compared the fitting results with and without characterized IRF, and it's found that the large 'chirp' and low spectral resolution could deteriorate (or broaden) the temporal profile of the up-converted signal. However, this was a preliminary result I would

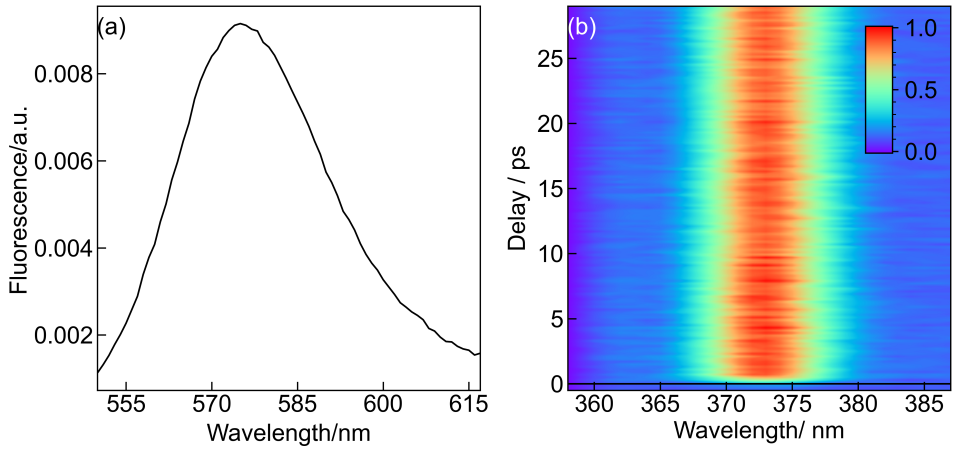

Figure 5.6: Up-conversion measurements of Rhodamine B in ethanol at 295 K. (a) Fluorescence spectrum of Rhodamine B in ethanol excited with 532 nm, (b) Fluorescence up-conversion spectrum of Rhodamine B.

like not to overexplain and conduct different fitting functions. More detailed studies will be performed in the near future in monolayer samples to try to find a plausible explanation for the observed huge 'chirp'. Nevertheless, I demonstrated the capabilities of our setup to measure tr-PL from a bilayer semiconducting 2D-TMDCs, and from a model dye in solution with good SNR, $\sim$ 200 fs temporal resolution and spectral resolution.

Chapter 6

Conclusion and Outlook

6.1 Conclusion

This thesis investigates different layered materials by means of tr-bb-TA, tr-bb-TR, and fs-PLup. We explored different photoinduced structural phenomena in the time domain. In our work on both ultra-thin films and single crystal of T_d-$MoTe_2$ (chapter 3), large BGR effects were observed during the initial 0.5 ps. The first several picoseconds in our tr-spectroscopic measurements provided information about the dynamical behaviour of the coherent $^1A_1$ interlayer shear phonon. We did not observe any signature of the preciously acclaimed PIPT. Instead, we found the formation of a metastable hot T_d-$MoTe_2$ state that develops into a persistent strained state in thin flakes. Our work demonstrates a significant contribution to the understanding of PIPTs and the requirements for these to proceed on ultrafast timescales. Importantly, the formation of light-induced long-live states in the

thin film of $MoTe_2$ presents the opportunity for light-induced manipulation of the topological properties in these types of materials. Moreover, by extending the time window of our transient measurements, we were able to monitor CAWs in thin-film of $MoTe_2$ and a single crystal of $2H$-SnS_2 (chapter 4). Here, we demonstrated that tr-bb-TR/ tr-bb-TA are reliable and non-destructive techniques to determine the elastic properties of layered materials, which are either too small for conventional mechanical tests or too brittle. Finally, I introduced our fs-PLup setup, which was built for the investigation of PL decay dynamics in a semiconducting bilayer MoS_2/WS_2 heterostructure (chapter 5). Owing to the background free and high temporal resolution features of our fs-PLup setup, we obtained good SNR and excellent ~ 200 fs temporal resolution, which revealed features never observed (still work in progress) with decay time constant of sub ps. Studying the radiative dynamics via an advanced time-resolved photoluminescence method will provide a better understanding of the radiative and non-radiative recombination processes in 2D-TMDCs, which show great promise in becoming the materials in high-performance optoelectronic and photonic devices.

6.2 Outlook

Future work will focus on the investigation of excitonic dynamics in various 2D-TMDCs and their heterostructures by fs-PLup. Special attention will be paid to the study of PL dynamics in monolayer MoS_2, WS_2 and MoS_2/WS_2 bilayer to understand the unusual 'chirp' observed in the bilayer sample (chapter 5). As for the fs-PLup setup, to cover the

entire PL broad spectral range one needs to vary the angle of the nonlinear crystal with respect to the gate and the PL beams. In the future, the SFG crystal could be mounted on a motorized rotational stage and controlled by the same data acquisition software. Recall that, for instance, monolayer $2H$-MoS_2 have K and K' valleys in which interband transitions are coupled to right and left circularly polarized light, respectively. Therefore, we could build a polarization-resolved tr-PL setup based on the current fs-PLup technique to further monitor the valley depolarization time which might limit the practical use of monolayer TMDCs for valleytronics. Furthermore, external factors, like temperature and gate voltage, will influence the exciton dynamics 2D-TMDCs. Thus, we could combine our setup with a cryostat or modify the sample substrate/mount to enable voltage gating. It is my hope that future works conducted by this fs-PLup setup could drive innovation in the field of 2D-TMDCs and their applications. As for the tr-bb-TA and tr-bb-TR techniques at UeIL, they are very mature and fully automated. However, we could not observe higher frequency coherent phonon modes due to our laser pulse width ($\sim$ 100 fs). Finalizing the construction of our homemade noncollinear OPA will confer 10 fs pump pulses and permit the observation of $\sim$ 1000 cm^{-1} modes. The noncollinear OPA setup is only missing a pair of dispersion compensating chirped mirrors to achieve this goal[193].

References

[1] Zhang, M. *et al.* Light-induced subpicosecond lattice symmetry switch in $MoTe_2$. *Phys. Rev. X* **9**, 021036 (2019).

[2] Khan, K. *et al.* Recent developments in emerging two-dimensional materials and their applications. *J. Mater. Chem. C* **8**, 387–440 (2020).

[3] Chhowalla, M. *et al.* The chemistry of two-dimensional layered transition metal dichalcogenide nanosheets. *Nat. Chem.* **5**, 263–275 (2013).

[4] Katzke, H., Tolédano, P. & Depmeier, W. Phase transitions between polytypes and intralayer superstructures in transition metal dichalcogenides. *Phys. Rev. B* **69**, 134111 (2004).

[5] Kolobov, A. V. & Tominaga, J. *Two-dimensional transition-metal dichalcogenides*, vol. 239 (Springer, 2016).

[6] Qi, Y. *et al.* Photoinduced concurrent intralayer and interlayer structural transitions and associated topological transitions in MTe_2 (M= Mo, W). *arXiv:2105.14175* (2021).

[7] Keum, D. H. *et al.* Bandgap opening in few-layered monoclinic $MoTe_2$. *Nat. Phys.* **11**, 482–486 (2015).

[8] Duerloo, K.-A. N., Li, Y. & Reed, E. J. Structural phase transitions in two-dimensional mo-and w-dichalcogenide monolayers. *Nat. Commun.* **5**, 1–9 (2014).

[9] Huang, H., Fan, X., Singh, D. J. & Zheng, W. Recent progress of tmd nanomaterials: phase transitions and applications. *Nanoscale* **12**, 1247–1268 (2020).

[10] Mak, K. F., Lee, C., Hone, J., Shan, J. & Heinz, T. F. Atomically thin MoS_2: a new direct-gap semiconductor. *Phys. Rev. Lett.* **105**, 136805 (2010).

[11] Kuc, A., Zibouche, N. & Heine, T. Influence of quantum confinement on the electronic structure of the transition metal sulfide TS_2. *Phys. Rev. B* **83**, 245213 (2011).

[12] Roldán, R. *et al.* Electronic properties of single-layer and multilayer transition metal dichalcogenides MX_2 (M= Mo, W and X= S, Se). *Ann. Phys.* **526**, 347–357 (2014).

[13] Splendiani, A. *et al.* Emerging photoluminescence in monolayer MoS_2. *Nano Lett.* **10**, 1271–1275 (2010).

[14] Mak, K. F., Xiao, D. & Shan, J. Light–valley interactions in 2D semiconductors. *Nat. Photonics* **12**, 451–460 (2018).

[15] Zeng, H., Dai, J., Yao, W., Xiao, D. & Cui, X. Valley polarization in MoS_2 monolayers by optical pumping. *Nat. Nanotechnol.* **7**, 490–493 (2012).

[16] Mak, K. F., He, K., Shan, J. & Heinz, T. F. Control of valley polarization in monolayer MoS_2 by optical helicity. *Nat. Nanotechnol.* **7**, 494–498 (2012).

[17] Liu, G.-B., Shan, W.-Y., Yao, Y., Yao, W. & Xiao, D. Three-band tight-binding model for monolayers of group-VIB transition metal dichalcogenides. *Phys. Rev. B* **88**, 085433 (2013).

[18] Zhu, C. *et al.* Exciton valley dynamics probed by kerr rotation in WSe_2 monolayers. *Phys. Rev. B* **90**, 161302 (2014).

[19] Mai, C. *et al.* Many-body effects in valleytronics: direct measurement of valley lifetimes in single-layer MoS_2. *Nano Lett.* **14**, 202–206 (2014).

[20] Dal Conte, S. *et al.* Ultrafast valley relaxation dynamics in monolayer MoS_2 probed by nonequilibrium optical techniques. *Phys. Rev. B* **92**, 235425 (2015).

[21] Mak, K. F. & Shan, J. Photonics and optoelectronics of 2D semiconductor transition metal dichalcogenides. *Nat. Photonics* **10**, 216–226 (2016).

[22] Yu, H., Laurien, M., Hu, Z. & Rubel, O. Exploration of the bright and dark exciton landscape and fine structure of MoS_2 using G_0W_0-BSE. *Phys. Rev. B* **100**, 125413 (2019).

[23] Burns, G. *Solid state physics* (Academic press, 2016).

[24] Song, S. *et al.* Room temperature semiconductor–metal transition of $MoTe_2$ thin films engineered by strain. *Nano Lett.* **16**, 188–193 (2016).

[25] Tan, Y. *et al.* Controllable 2H-to-1T' phase transition in few-layer $MoTe_2$. *Nanoscale* **10**, 19964–19971 (2018).

[26] Cho, S. *et al.* Phase patterning for ohmic homojunction contact in $MoTe_2$. *Sci.* **349**, 625–628 (2015).

[27] Song, S. *et al.* Room temperature semiconductor–metal transition of $MoTe_2$ thin films engineered by strain. *Nano Lett.* **16**, 188–193 (2016).

[28] Wang, L. *et al.* One-dimensional electrical contact to a two-dimensional material. *Sci.* **342**, 614–617 (2013).

[29] Empante, T. A. *et al.* Chemical vapor deposition growth of few-layer $MoTe_2$ in the 2H, 1T', and 1T phases: tunable properties of $MoTe_2$ films. *ACS nano* **11**, 900–905 (2017).

[30] Zhang, M. *et al.* Light induced sub-picosecond topological phase transition in $MoTe_2$. *arXiv:1806.09075* (2018).

[31] Song, H. *et al.* High-performance top-gated monolayer SnS_2 field-effect transistors and their integrated logic circuits. *Nanoscale* **5**, 9666–9670 (2013).

[32] De, D. *et al.* High on/off ratio field effect transistors based on exfoliated crystalline SnS_2 nano-membranes. *Nanotechnology* **24**, 025202 (2012).

[33] Su, G. *et al.* Chemical vapor deposition of thin crystals of layered semiconductor SnS_2 for fast photodetection application. *Nano Lett.* **15**, 506–513 (2015).

[34] Tao, Y., Wu, X., Wang, W. & Wang, J. Flexible photodetector from ultraviolet to near infrared based on a SnS_2 nanosheet microsphere film. *J. Mater. Chem. C* **3**, 1347–1353 (2015).

[35] Shi, W. *et al.* Hydrothermal growth and gas sensing property of flower-shaped SnS_2 nanostructures. *Nanotechnology* **17**, 2918 (2006).

[36] Cui, X., Xu, W., Xie, Z. & Wang, Y. High-performance dye-sensitized solar cells based on Ag-doped SnS_2 counter electrodes. *J. Mater. Chem. A* **4**, 1908–1914 (2016).

[37] Huang, Y. *et al.* Tin disulfide an emerging layered metal dichalcogenide semiconductor: Materials properties and device characteristics. *ACS nano* **8**, 10743–10755 (2014).

[38] Sriv, T., Kim, K. & Cheong, H. Low-frequency raman spectroscopy of few-layer 2H-SnS_2. *Sci. Rep.* **8**, 1–7 (2018).

[39] Shibata, T., Kambe, N., Muranushi, Y., Miura, T. & Kishi, T. Optical characterisation of single crystal 2H-SnS2 synthesised by the chemical vapour transport method at low temperatures. *J. Phys. D* **23**, 719 (1990).

[40] Gonzalez, J. M. & Oleynik, I. I. Layer-dependent properties of SnS_2 and $SnSe_2$ two-dimensional materials. *Phys. Rev. B* **94**, 125443 (2016).

[41] Panda, S., Antonakos, A., Liarokapis, E., Bhattacharya, S. & Chaudhuri, S. Optical properties of nanocrystalline SnS_2 thin films. *Mater. Res. Bull.* **42**, 576–583 (2007).

[42] Ermolaev, G. A. *et al.* Broadband optical constants and nonlinear properties of SnS_2 and $SnSe_2$. *Nanomaterials* **12**, 141 (2021).

[43] Burton, L. A. *et al.* Electronic and optical properties of single crystal SnS_2: an earth-abundant disulfide photocatalyst. *J. Mater. Chem. A* **4**, 1312–1318 (2016).

[44] Mnari, M., Cros, B., Amlouk, M., Belgacem, S. & Barjon, D. Study of the elastic properties of sprayed SnO_2 and SnS_2 layers. *Can. J. Phys.* **77**, 705–715 (2000).

[45] He, X. & Shen, H. Ab initio calculations of band structure and thermophysical properties for SnS_2 and $SnSe_2$. *Phys. B: Condens. Matter* **407**, 1146–1152 (2012).

[46] Wang, H., Gao, Y. & Liu, G. Anisotropic phonon transport and lattice thermal conductivities in tin dichalcogenides SnS_2 and $SnSe_2$. *RSC advances* **7**, 8098–8105 (2017).

[47] Zhen, Z.-Q. & Wang, H.-Y. Density functional study of the electronic, elastic, and lattice dynamic properties of SnS_2. *Acta Phys. Pol. A* **137** (2020).

[48] Zhan, S., Zheng, L., Xiao, Y. & Zhao, L.-D. Phonon and carrier transport properties in low-cost and environmentally friendly SnS_2: A promising thermoelectric material. *Chem. Mater.* **32**, 10348–10356 (2020).

[49] Peng, B., Ang, P. K. & Loh, K. P. Two-dimensional dichalcogenides for light-harvesting applications. *Nano Today* **10**, 128–137 (2015).

[50] Huo, N., Yang, Y. & Li, J. Optoelectronics based on 2D TMDs and heterostructures. *J. Semicond.* **38**, 031002 (2017).

[51] Bernardi, M., Palummo, M. & Grossman, J. C. Extraordinary sunlight absorption and one nanometer thick photovoltaics using two-dimensional monolayer materials. *Nano Lett.* **13**, 3664–3670 (2013).

[52] Ceballos, F., Bellus, M. Z., Chiu, H.-Y. & Zhao, H. Ultrafast charge separation and indirect exciton formation in a MoS_2-$MoSe_2$ van der Waals heterostructure. *ACS nano* **8**, 12717–12724 (2014).

[53] Bian, A. *et al.* Ultrafast charge transfer and carrier dynamics in a $WS_2/MoSe_2$ few-layer van der Waals heterostructure. *J. Mater. Chem. C* **10**, 5328–5335 (2022).

[54] Hong, X. *et al.* Ultrafast charge transfer in atomically thin MoS_2/WS_2 heterostructures. *Nat. Nanotechnol.* **9**, 682–686 (2014).

[55] Jiang, Y., Chen, S., Zheng, W., Zheng, B. & Pan, A. Interlayer exciton formation, relaxation, and transport in TMD van der Waals heterostructures. *Light Sci. Appl.* **10**, 1–29 (2021).

[56] Chen, H. *et al.* Ultrafast formation of interlayer hot excitons in atomically thin MoS_2/WS_2 heterostructures. *Nat. Commun.* **7**, 1–8 (2016).

[57] Pan, S., Ceballos, F., Bellus, M. Z., Zereshki, P. & Zhao, H. Ultrafast charge transfer between $MoTe_2$ and MoS_2 monolayers. *2D Materials* **4**, 015033 (2016).

[58] Zewail, A. H. Femtochemistry: Atomic-scale dynamics of the chemical bond. *J. Phys. Chem. A* **104**, 5660–5694 (2000).

[59] Abraham, H. & Lemoine, J. Disparition instantanée du phénomène de kerr. *CR Acad. Sci. Hebd Seances Acad. Sci. D* **129**, 206–208 (1899).

[60] Lloyd-Hughes, J. *et al.* The 2021 ultrafast spectroscopic probes of condensed matter roadmap. *J. Condens. Matter Phys.* **33**, 353001 (2021).

[61] Shah, J. *Ultrafast spectroscopy of semiconductors and semiconductor nanostructures*, vol. 115 (Springer Science & Business Media, 2013).

[62] Chernikov, A., Ruppert, C., Hill, H. M., Rigosi, A. F. & Heinz, T. F. Population inversion and giant bandgap renormalization in atomically thin WS_2 layers. *Nat. Photonics* **9**, 466–470 (2015).

[63] Pöllmann, C. *et al.* Resonant internal quantum transitions and femtosecond radiative decay of excitons in monolayer WSe_2. *Nat. Mater.* **14**, 889–893 (2015).

[64] Robert, C. *et al.* Exciton radiative lifetime in transition metal dichalcogenide monolayers. *Phys. Rev. B* **93**, 205423 (2016).

[65] Pogna, E. A. *et al.* Photo-induced bandgap renormalization governs the ultrafast response of single-layer MoS_2. *ACS nano* **10**, 1182–1188 (2016).

[66] Ruckebusch, C., Sliwa, M., Pernot, P. d., De Juan, A. & Tauler, R. Comprehensive data analysis of femtosecond transient absorption spectra: A review. *J. Photochem. Photobiol. C: Photochem. Rev.* **13**, 1–27 (2012).

[67] Bonneau, R., Wirz, J. & Zuberbuhler, A. Methods for the analysis of transient absorbance data (technical report). *Pure Appl. Chem.* **69**, 979–992 (1997).

[68] van Wilderen, L. J., Lincoln, C. N. & van Thor, J. J. Modelling multi-pulse population dynamics from ultrafast spectroscopy. *PloS one* **6**, e17373 (2011).

[69] Berera, R., van Grondelle, R. & Kennis, J. Ultrafast transient absorption spectroscopy: principles and application to photosynthetic systems. *Photosynth. Res.* **101**, 105–118 (2009).

[70] Kumar, N. *et al.* Exciton-exciton annihilation in $MoSe_2$ monolayers. *Phys. Rev. B* **89**, 125427 (2014).

[71] Sun, D. *et al.* Observation of rapid exciton–exciton annihilation in monolayer molybdenum disulfide. *Nano Lett.* **14**, 5625–5629 (2014).

[72] You, Y. *et al.* Observation of biexcitons in monolayer WSe_2. *Nat. Phys.* **11**, 477–481 (2015).

[73] Okada, M. *et al.* Observation of biexcitonic emission at extremely low power density in tungsten disulfide atomic layers grown on hexagonal boron nitride. *Sci. Rep.* **7**, 1–7 (2017).

[74] Tan, P. *et al.* The shear mode of multilayer graphene. *Nat. Mater.* **11**, 294–300 (2012).

[75] Lee, C. *et al.* Anomalous lattice vibrations of single-and few-layer MoS_2. *ACS nano* **4**, 2695–2700 (2010).

[76] Bertoldo Menezes, D., Reyer, A., Yüksel, A., Bertoldo Oliveira, B. & Musso, M. Introduction to terahertz raman spectroscopy. *Spectrosc. Lett.* **51**, 438–445 (2018).

[77] Ge, S. *et al.* Coherent longitudinal acoustic phonon approaching THz frequency in multilayer molybdenum disulphide. *Sci. Rep.* **4**, 1–7 (2014).

[78] Boschetto, D. *et al.* Real-time observation of interlayer vibrations in bilayer and few-layer graphene. *Nano Lett.* **13**, 4620–4623 (2013).

[79] Mallat, S. *A wavelet tour of signal processing* (Elsevier, 1999).

[80] Thompson, C. & Shure, L. *Signal Processing Toolbox: user's Guide (r2022a)* (MathWorks, 2022).

[81] Huang, S.-Y. & Bai, Z. Wavelets, advanced (2003).

[82] Borisagar, K. R., Thanki, R. M. & Sedani, B. S. Fourier transform, short-time fourier transform, and wavelet transform. In *Speech Enhancement Techniques for Digital Hearing Aids*, 63–74 (Springer, 2019).

[83] Mallat, S. *et al.* A wavelet tour of signal processing: the sparce way. *AP Professional, Third Edition, London* (2009).

[84] Molina-Sánchez, A., Palummo, M., Marini, A. & Wirtz, L. Temperature-dependent excitonic effects in the optical properties of single-layer MoS_2. *Phys. Rev. B* **93**, 155435 (2016).

[85] Gibertini, M., Koperski, M., Morpurgo, A. F. & Novoselov, K. S. Magnetic 2D materials and heterostructures. *Nat. Nanotechnol.* **14**, 408–419 (2019).

[86] Mahgoub, M. *et al.* Longitudinal phase space studies at the pitz facility. *MOPPP032, these proceedings* (2016).

[87] Lemmetyinen, H. *et al.* Time-resolved fluorescence methods (IUPAC technical report). *Pure Appl. Chem.* **86**, 1969–1998 (2014).

[88] Yuan, L. & Huang, L. Exciton dynamics and annihilation in WS_2 2D semiconductors. *Nanoscale* **7**, 7402–7408 (2015).

[89] Wang, H., Zhang, C. & Rana, F. Ultrafast dynamics of defect-assisted electron–hole recombination in monolayer MoS_2. *Nano Lett.* **15**, 339–345 (2015).

[90] Zhao, L. & Xia, T. Probing RNA conformational dynamics and heterogeneity using femtosecond time-resolved fluorescence spectroscopy. *Methods* **49**, 128–135 (2009).

[91] Xie, Y. *et al.* Femtosecond time-resolved fluorescence study of P3HT/PCBM blend films. *J. Phys. Chem. C* **114**, 14590–14600 (2010).

[92] Yu, Z., Gundlach, L. & Piotrowiak, P. Efficiency and temporal response of crystalline kerr media in collinear optical kerr gating. *Opt. Lett.* **36**, 2904–2906 (2011).

[93] Zhang, H. *et al.* Efficient optical kerr gate of tellurite glass for acquiring ultrafast fluorescence. *J. Opt.* **14**, 065201 (2012).

[94] Yan, L.-H. *et al.* Application of optical kerr gate with $SrTiO_3$ crystal in acquisition of gated spectra from a supercontinuum. *Chin. Phys. Lett.* **29**, 074207 (2012).

[95] Strickland, D. & Mourou, G. Compression of amplified chirped optical pulses. *Opt. Commun.* **55**, 447–449 (1985).

[96] Chen, K., Gallaher, J. K., Barker, A. J. & Hodgkiss, J. M. Transient grating photoluminescence spectroscopy: an ultrafast method of gating broadband spectra. *The journal of physical chemistry letters* **5**, 1732–1737 (2014).

[97] Boyd, R. W. *Nonlinear optics* (Academic press, 2020).

[98] Shah, J. Ultrafast luminescence spectroscopy using sum frequency generation. *IEEE J. Quantum Electron.* **24**, 276–288 (1988).

[99] Dmitruk, I. *et al.* Efficiency estimates and practical aspects of an optical kerr gate for time-resolved luminescence spectroscopy. *Methods Appl. Fluoresc.* **4**, 044007 (2016).

[100] Zhao, L., Lustres, J. L. P., Farztdinov, V. & Ernsting, N. P. Femtosecond fluorescence spectroscopy by upconversion with tilted gate pulses. *Phys. Chem. Chem. Phys.* **7**, 1716–1725 (2005).

[101] Dmitriev, V. G., Gurzadyan, G. G. & Nikogosyan, D. N. *Handbook of nonlinear optical crystals*, vol. 64 (Springer, 2013).

[102] Cheon, Y., Lim, S. Y., Kim, K. & Cheong, H. Structural phase transition and interlayer coupling in few-layer 1T' and T_d $MoTe_2$. *ACS nano* **15**, 2962–2970 (2021).

[103] Zhang, K. *et al.* Raman signatures of inversion symmetry breaking and structural phase transition in type-II Weyl semimetal $MoTe_2$. *Nat. Commun.* **7**, 1–6 (2016).

[104] Vellinga, M., De Jonge, R. & Haas, C. Semiconductor to metal transition in $MoTe_2$. *J. Solid State Chem.* **2**, 299–302 (1970).

[105] Rhodes, D. *et al.* Engineering the structural and electronic phases of $MoTe_2$ through W substitution. *Nano Lett.* **17**, 1616–1622 (2017).

[106] He, R. *et al.* Dimensionality-driven orthorhombic $MoTe_2$ at room temperature. *Phys. Rev. B* **97**, 041410 (2018).

[107] Soluyanov, A. A. *et al.* Type-II Weyl semimetals. *Nature* **527**, 495–498 (2015).

[108] Jiang, J. *et al.* Signature of type-II Weyl semimetal phase in $MoTe_2$. *Nat. Commun.* **8**, 1–6 (2017).

[109] Yan, B. & Felser, C. Topological materials: Weyl semimetals. *arXiv:1611.04182* (2016).

[110] Zhang, K. *et al.* Raman signatures of inversion symmetry breaking and structural phase transition in type-II Weyl semimetal $MoTe_2$. *Nat. Commun.* **7**, 1–6 (2016).

[111] Chen, S.-Y., Goldstein, T., Venkataraman, D., Ramasubramaniam, A. & Yan, J. Activation of new raman modes by inversion symmetry breaking in type II Weyl semimetal candidate T'-$MoTe_2$. *Nano Lett.* **16**, 5852–5860 (2016).

[112] Cheng, M. *et al.* Photoinduced interlayer dynamics in T_d-$MoTe_2$: A broadband pump-probe study. *arXiv:2201.04961* (2022).

[113] Crepaldi, A. *et al.* Enhanced ultrafast relaxation rate in the Weyl semimetal phase of $MoTe_2$ measured by time-and angle-resolved photoelectron spectroscopy. *Phys. Rev. B* **96**, 241408 (2017).

[114] Sciaini, G. & Miller, R. D. Femtosecond electron diffraction: heralding the era of atomically resolved dynamics. *Rep. Prog. Phys.* **74**, 096101 (2011).

[115] Sciaini, G. Recent advances in ultrafast structural techniques. *Appl* **9**, 1427 (2019).

[116] Nakamura, A., Shimojima, T., Nakano, M., Iwasa, Y. & Ishizaka, K. Electron and lattice dynamics of transition metal thin films observed by ultrafast electron diffraction and transient optical measurements. *Struct. Dyn.* **3**, 064501 (2016).

[117] Perfetti, L. *et al.* Time evolution of the electronic structure of 1T-TaS_2 through the insulator-metal transition. *Phys. Rev. Lett.* **97**, 067402 (2006).

[118] Eichberger, M. *et al.* Snapshots of cooperative atomic motions in the optical suppression of charge density waves. *Nature* **468**, 799–802 (2010).

[119] Dai, Y. *et al.* Ultrafast carrier dynamics in the large magnetoresistance material WTe_2. In *International Conference on Ultrafast Phenomena*, UTu4A–47 (Optical Society of America, 2016).

[120] Waldecker, L. *et al.* Momentum-resolved view of electron-phonon coupling in multilayer WSe_2. *Phys. Rev. Lett.* **119**, 036803 (2017).

[121] Rossnagel, K. On the origin of charge-density waves in select layered transition-metal dichalcogenides. *J. Condens. Matter Phys.* **23**, 213001 (2011).

[122] Sie, E. J. *et al.* An ultrafast symmetry switch in a Weyl semimetal. *Nature* **565**, 61–66 (2019).

[123] Zhong, S. *et al.* Origin of magnetoresistance suppression in thin γ-$MoTe_2$. *Phys. Rev. B* **97**, 241409 (2018).

[124] Lee, M.-C. *et al.* Strong spin-phonon coupling unveiled by coherent phonon oscillations in ca 2 ruo 4. *Physical Review B* **99**, 144306 (2019).

[125] Zeiger, H. *et al.* Theory for displacive excitation of coherent phonons. *Phys. Rev. B* **45**, 768 (1992).

[126] Scholz, R., Pfeifer, T. & Kurz, H. Density-matrix theory of coherent phonon oscillations in germanium. *Phys. Rev. B* **47**, 16229 (1993).

[127] Kuznetsov, A. V. & Stanton, C. J. Theory of coherent phonon oscillations in semiconductors. *Phys. Rev. Lett.* **73**, 3243 (1994).

[128] Dhar, L., Rogers, J. A. & Nelson, K. A. Time-resolved vibrational spectroscopy in the impulsive limit. *Chem. Rev.* **94**, 157–193 (1994).

[129] Garrett, G. A., Albrecht, T., Whitaker, J. & Merlin, R. Coherent thz phonons driven by light pulses and the sb problem: what is the mechanism? *Physical review letters* **77**, 3661 (1996).

[130] Merlin, R. Generating coherent THz phonons with light pulses. *Solid State Commun.* **102**, 207–220 (1997).

[131] DeCamp, M., Reis, D., Bucksbaum, P. & Merlin, R. Dynamics and coherent control of high-amplitude optical phonons in bismuth. *Phys. Rev. B* **64**, 092301 (2001).

[132] Stevens, T., Kuhl, J. & Merlin, R. Coherent phonon generation and the two stimulated Raman tensors. *Phys. Rev. B* **65**, 144304 (2002).

[133] Misochko, O., Hase, M. & Kitajima, M. On the nature of coherent phonons generated by ultrashort laser pulses in single-crystal antimony. *Phys. Solid State* **46**, 1741–1749 (2004).

[134] Riffe, D. M. & Sabbah, A. Coherent excitation of the optic phonon in Si: Transiently stimulated Raman scattering with a finite-lifetime electronic excitation. *Phys. Rev. B* **76**, 085207 (2007).

[135] Santos-Cottin, D. *et al.* Low-energy excitations in type-II Weyl semimetal T_d- $MoTe_2$ evidenced through optical conductivity. *Phys. Rev. Mater.* **4**, 021201 (2020).

[136] Wall, S. *et al.* Ultrafast changes in lattice symmetry probed by coherent phonons. *Nat. Commun.* **3**, 1–6 (2012).

[137] Kiwia, H. L. & Westrum Jr, E. F. Low-temperature heat capacities of molybdenum diselenide and ditelluride. *J. Chem. Thermodyn* **7**, 683–691 (1975).

[138] Beal, A., Knights, J. & Liang, W. Transmission spectra of some transition metal dichalcogenides. II. group VIA: trigonal prismatic coordination. *J. Phys. C* **5**, 3540 (1972).

[139] Mannebach, E. M. *et al.* Dynamic optical tuning of interlayer interactions in the transition metal dichalcogenides. *Nano Lett.* **17**, 7761–7766 (2017).

[140] Kumazoe, H. *et al.* Photo-induced lattice contraction in layered materials. *J. Condens. Matter Phys.* **30**, 32LT02 (2018).

[141] Li, D. *et al.* Anisotropic enhancement of second-harmonic generation in monolayer and bilayer MoS_2 by integrating with TiO_2 nanowires. *Nano Lett.* **19**, 4195–4204 (2019).

[142] Liang, J. *et al.* Monitoring local strain vector in atomic-layered $MoSe_2$ by second-harmonic generation. *Nano Lett.* **17**, 7539–7543 (2017).

[143] Mennel, L., Paur, M. & Mueller, T. Second harmonic generation in strained transition metal dichalcogenide monolayers: MoS_2, $MoSe_2$, WS_2, and WSe_2. *APL Photonics* **4**, 034404 (2019).

[144] Zhou, L. *et al.* Nonlinear optical characterization of 2D materials. *Nanomaterials* **10**, 2263 (2020).

[145] Khan, A. R. *et al.* Extraordinary temperature dependent second harmonic generation in atomically thin layers of transition-metal dichalcogenides. *Adv. Opt. Mater.* **8**, 2000441 (2020).

[146] Cavalleri, A. *et al.* Femtosecond structural dynamics in VO_2 during an ultrafast solid-solid phase transition. *Phys. Rev. Lett.* **87**, 237401 (2001).

[147] Cavalleri, A., Dekorsy, T., Chong, H. H., Kieffer, J.-C. & Schoenlein, R. W. Evidence for a structurally-driven insulator-to-metal transition in VO_2: A view from the ultrafast timescale. *Phys. Rev. B* **70**, 161102 (2004).

[148] Baum, P., Yang, D.-S. & Zewail, A. H. 4D visualization of transitional structures in phase transformations by electron diffraction. *Sci.* **318**, 788–792 (2007).

[149] Tao, Z. *et al.* Decoupling of structural and electronic phase transitions in VO_2. *Phys. Rev. Lett.* **109**, 166406 (2012).

[150] Morrison, V. R. *et al.* A photoinduced metal-like phase of monoclinic VO_2 revealed by ultrafast electron diffraction. *Sci.* **346**, 445–448 (2014).

[151] Wall, S. *et al.* Ultrafast disordering of vanadium dimers in photoexcited VO_2. *Sci.* **362**, 572–576 (2018).

[152] Chollet, M. *et al.* Gigantic photoresponse in 1/4-filled-band organic salt (EDO-TTF)$_2$PF$_6$. *Sci.* **307**, 86–89 (2005).

[153] Onda, K. *et al.* Photoinduced change in the charge order pattern in the quarter-filled organic conductor (EDO-TTF)$_2$PF$_6$ with a strong electron-phonon interaction. *Phys. Rev. Lett.* **101**, 067403 (2008).

[154] Gao, M. *et al.* Mapping molecular motions leading to charge delocalization with ultrabright electrons. *Nature* **496**, 343–346 (2013).

[155] Huang, F.-T. *et al.* Polar and phase domain walls with conducting interfacial states in a *w*eyl semimetal $MoTe_2$. *Nat. Commun.* **10**, 1–9 (2019).

[156] Basov, D., Averitt, R. & Hsieh, D. Towards properties on demand in quantum materials. *Nat. Mater.* **16**, 1077–1088 (2017).

[157] Santos-Cottin, D. *et al.* Low-energy excitations in type-II Weyl semimetal T_d-$MoTe_2$ evidenced through optical conductivity. *Phys. Rev. Mater.* **4**, 021201 (2020).

[158] Zhang, J. *et al.* Cooperative photoinduced metastable phase control in strained manganite films. *Nat. Mater.* **15**, 956–960 (2016).

[159] Li, X. *et al.* Terahertz field–induced ferroelectricity in quantum paraelectric $SrTiO_3$. *Sci.* **364**, 1079–1082 (2019).

[160] Stojchevska, L. *et al.* Ultrafast switching to a stable hidden quantum state in an electronic crystal. *Sci.* **344**, 177–180 (2014).

[161] Maris, H. Picosecond ultrasonics. *Sci. Am.* **278**, 86–89 (1998).

[162] Thomsen, C. *et al.* Coherent phonon generation and detection by picosecond light pulses. *Phys. Rev. Lett.* **53**, 989 (1984).

[163] Eesley, G. L., Clemens, B. M. & Paddock, C. A. Generation and detection of picosecond acoustic pulses in thin metal films. *Appl. Phys. Lett.* **50**, 717–719 (1987).

[164] Thomsen, C., Grahn, H. T., Maris, H. J. & Tauc, J. Surface generation and detection of phonons by picosecond light pulses. *Phys. Rev. B* **34**, 4129 (1986).

[165] Glinka, Y. D., Babakiray, S., Johnson, T. A., Holcomb, M. B. & Lederman, D. Acoustic phonon dynamics in thin-films of the topological insulator Bi_2Se_3. *J. Appl. Phys.* **117**, 165703 (2015).

[166] Chen, K. *et al.* Accelerated carrier recombination by grain boundary/edge defects in mbe grown transition metal dichalcogenides. *APL Materials* **6**, 056103 (2018).

[167] Lindroth, D. O. & Erhart, P. Thermal transport in van der waals solids from first-principles calculations. *Phys. Rev. B* **94**, 115205 (2016).

[168] Brown, B. E. The crystal structures of WTe_2 and high-temperature $MoTe_2$. *Acta Crystallogr.* **20**, 268–274 (1966).

[169] Marsden, B., Mummery, A. & Mummery, P. Modelling the coefficient of thermal expansion in graphite crystals: implications of lattice strain due to irradiation and pressure. *Proc. R. Soc. A: Math. Phys. Eng. Sci.* **474**, 20180075 (2018).

[170] McKinney, R. W., Gorai, P., Manna, S., Toberer, E. & Stevanović, V. Ionic vs. van der Waals layered materials: identification and comparison of elastic anisotropy. *J. Mater. Chem. A* **6**, 15828–15838 (2018).

[171] Brillouin, L. Diffussion of light and x-rays by a homogeneous transparent bady. *Ann. Phys.* **9**, 88–122 (1922).

[172] Damzen, M., Vlad, V., Mocofanescu, A. & Babin, V. *Stimulated Brillouin scattering: fundamentals and applications* (CRC press, 2003).

[173] Harb, M. *et al.* Excitation of longitudinal and transverse coherent acoustic phonons in nanometer free-standing films of (001) Si. *Phys. Rev. B* **79**, 094301 (2009).

[174] Rivas, N. *et al.* Generation and detection of coherent longitudinal acoustic waves in ultrathin 1 T'-$MoTe_2$. *Appl. Phys. Lett.* **115**, 223103 (2019).

[175] Nelson, K. A. Stimulated brillouin scattering and optical excitation of coherent shear waves. *J. Appl. Phys.* **53**, 6060–6063 (1982).

[176] Matsuda, O., Wright, O., Hurley, D., Gusev, V. & Shimizu, K. Coherent shear phonon generation and detection with picosecond laser acoustics. *Phys. Rev. B* **77**, 224110 (2008).

[177] Still, T. *High frequency acoustics in colloid-based meso-and nanostructures by spontaneous Brillouin light scattering* (Springer Science & Business Media, 2010).

[178] Devos, A. & Côte, R. Strong oscillations detected by picosecond ultrasonics in silicon: Evidence for an electronic-structure effect. *Phys. Rev. B* **70**, 125208 (2004).

[179] Pontecorvo, E. *et al.* Visualizing coherent phonon propagation in the 100 GHz range: A broadband picosecond acoustics approach. *Appl. Phys. Lett.* **98**, 011901 (2011).

[180] Ruello, P. *et al.* Photoexcitation of gigahertz longitudinal and shear acoustic waves in $BiFeO_3$ multiferroic single crystal. *Appl. Phys. Lett.* **100**, 212906 (2012).

[181] Lejman, M. *et al.* Giant ultrafast photo-induced shear strain in ferroelectric $BiFeO_3$. *Nat. Commun.* **5**, 1–7 (2014).

[182] Chang, P. C., Walker, J. & Hopcraft, K. Ray tracing in absorbing media. *J. Quant. Spectrosc. Radiat. Transf.* **96**, 327–341 (2005).

[183] Brivio, S. *et al.* Observation of anomalous acoustic phonon dispersion in $SrTiO_3$ by broadband stimulated brillouin scattering. *Appl. Phys. Lett.* **98**, 211907 (2011).

[184] Brivio, S. *et al.* Response to "comment on 'observation of anomalous acoustic phonon dispersion in $SrTiO_3$ by broadband stimulated brillouin scattering' "[*Appl. Phys. Lett.* **100**, 206101 (2012)]. *Appl. Phys. Lett.* **100**, 206101 (2012).

[185] Gicala, P. *et al.* Time-resolved broadband impulsive stimulated brillouin scattering in single crystal hematite. *Appl. Phys. Lett.* **118**, 264101 (2021).

[186] Conley, H. J. *et al.* Bandgap engineering of strained monolayer and bilayer MoS_2. *Nano Lett.* **13**, 3626–3630 (2013).

[187] Ross, J. S. *et al.* Electrical control of neutral and charged excitons in a monolayer semiconductor. *Nat. Commun.* **4**, 1–6 (2013).

[188] Mouri, S., Miyauchi, Y. & Matsuda, K. Tunable photoluminescence of monolayer MoS_2 via chemical doping. *Nano Lett.* **13**, 5944–5948 (2013).

[189] Moody, G. *et al.* Intrinsic homogeneous linewidth and broadening mechanisms of excitons in monolayer transition metal dichalcogenides. *Nat. Commun.* **6**, 1–6 (2015).

[190] Korn, T., Heydrich, S., Hirmer, M., Schmutzler, J. & Schüller, C. Low-temperature photocarrier dynamics in monolayer MoS_2. *Appl. Phys. Lett.* **99**, 102109 (2011).

[191] Thompson, A. G. MOCVD technology for semiconductors. *Mater. Lett.* **30**, 255–263 (1997).

[192] Zhang, X.-X., You, Y., Zhao, S. Y. F. & Heinz, T. F. Experimental evidence for dark excitons in monolayer WSe_2. *Phys. Rev. Lett.* **115**, 257403 (2015).

[193] Liebel, M., Schnedermann, C. & Kukura, P. Sub-10-fs pulses tunable from 480 to 980 nm from a nopa pumped by an yb: Kgw source. *Opt. lett.* **39**, 4112–4115 (2014).

[194] Kertesz, M. & Hoffmann, R. Octahedral vs. trigonal-prismatic coordination and clustering in transition-metal dichalcogenides. *J. Am. Chem. Soc.* **106**, 3453–3460 (1984).

[195] Fang, C., Wiegers, G., Haas, C. & De Groot, R. Electronic structures of, and in the real and the hypothetical undistorted structures. *J. Condens. Matter Phys.* **9**, 4411 (1997).

[196] Schaibley, J. R. *et al.* Valleytronics in 2D materials. *Nat. Rev. Mater.* **1**, 1–15 (2016).

[197] Maiti, R. *et al.* Strain-engineered high-responsivity $MoTe_2$ photodetector for silicon photonic integrated circuits. *Nat. Photonics* **14**, 578–584 (2020).

[198] Liu, Y., Zhang, S., He, J., Wang, Z. M. & Liu, Z. Recent progress in the fabrication, properties, and devices of heterostructures based on 2D materials. *Nano-Micro Lett.* **11**, 1–24 (2019).

[199] Richter, W. Extraordinary phonon raman scattering and resonance enhancement in tellurium. *J Phys Chem Solids* **33**, 2123–2128 (1972).

[200] Underwood, D. F., Kippeny, T. & Rosenthal, S. J. Ultrafast carrier dynamics in cdse nanocrystals determined by femtosecond fluorescence upconversion spectroscopy. *J. Phys. Chem. B* **105**, 436–443 (2001).

[201] Keene, J. D., McBride, J. R., Orfield, N. J. & Rosenthal, S. J. Elimination of hole–surface overlap in graded CdS_xSe_{1-x} nanocrystals revealed by ultrafast fluorescence upconversion spectroscopy. *ACS nano* **8**, 10665–10673 (2014).

[202] Bram, O., Cannizzo, A. & Chergui, M. Ultrafast broadband fluorescence up-conversion study of the electronic relaxation of metalloporphyrins. *J. Phys. Chem. A* **123**, 1461–1468 (2019).

[203] Dubietis, A., Tamošauskas, G., Šuminas, R., Jukna, V. & Couairon, A. Ultrafast supercontinuum generation in bulk condensed media. *Lith. J. Phys.* **57** (2017).

[204] Mahr, H. & Hirsch, M. D. An optical up-conversion light gate with picosecond resolution. *Opt. Commun.* **13**, 96–99 (1975).

[205] Gerecke, M., Bierhance, G., Gutmann, M., Ernsting, N. P. & Rosspeintner, A. Femtosecond broadband fluorescence upconversion spectroscopy: Spectral coverage versus efficiency. *Rev. Sci. Instrum.* **87**, 053115 (2016).

[206] Ji, Z. *et al.* Robust stacking-independent ultrafast charge transfer in MoS_2/WS_2 bilayers. *ACS nano* **11**, 12020–12026 (2017).

[207] Wang, Q. H., Kalantar-Zadeh, K., Kis, A., Coleman, J. N. & Strano, M. S. Electronics and optoelectronics of two-dimensional transition metal dichalcogenides. *Nat. Nanotechnol.* **7**, 699–712 (2012).

[208] Xu, X., Yao, W., Xiao, D. & Heinz, T. F. Spin and pseudospins in layered transition metal dichalcogenides. *Nat. Phys.* **10**, 343–350 (2014).

[209] Xiao, D., Yao, W. & Niu, Q. Valley-contrasting physics in graphene: magnetic moment and topological transport. *Phys. Rev. Lett.* **99**, 236809 (2007).

[210] Beaulieu, S. *et al.* Ultrafast dynamical Lifshitz transition. *Sci. Adv.* **7**, eabd9275 (2021).

[211] Li, D. *et al.* Anisotropic enhancement of second-harmonic generation in monolayer and bilayer MoS_2 by integrating with TiO_2 nanowires. *Nano Lett.* **19**, 4195–4204 (2019).

[212] Liang, J. *et al.* Monitoring local strain vector in atomic-layered $MoSe_2$ by second-harmonic generation. *Nano Lett.* **17**, 7539–7543 (2017).

[213] Mennel, L., Paur, M. & Mueller, T. Second harmonic generation in strained transition metal dichalcogenide monolayers: MoS_2, $MoSe_2$, WS_2, and WSe_2. *APL Photonics* **4**, 034404 (2019).

[214] Zhou, L. *et al.* Nonlinear optical characterization of 2D materials. *Nanomaterials* **10**, 2263 (2020).

[215] Zhao, W. *et al.* Evolution of electronic structure in atomically thin sheets of WS_2 and WSe_2. *ACS nano* **7**, 791–797 (2013).

APPENDICES

Appendix A

Python Code for Data Analysis

A.1 Extract Time-resolved Data from Snoop File

```
from __future__ import print_function
import matplotlib.pyplot as plt
import numpy as np
import matplotlib.gridspec as gridspec
Nsize = 14.0

### FIND VALUE FROM 1D ARRAY ###
'''
Returns the index and the closest value
of an array of floating numbers
'''
def find_value(array,value):
```

```
    idx = (np.abs(array-value)).argmin()
    closest_value = array[idx]
    iValue = np.where(array == closest_value)
    return int(iValue[0]),closest_value

### READ A FILE FROM SNOOP ###
'''
Reads a file and returns Wavelenght,TimeDelay, Matrix Absorption and File's name.
%Timezeromm = Where both beams are overlaped in the stage position [mm].
%iniWL = Remove wavelenght points from the beginning.
%cutWL = Remove wavelenght points from the back.
%iniPos = Remove Delay points from the beginning.
%cutPos = Remove Delay points from the back.
%flip = Fix the sign of the overall spectra by controling the sign at a given wavelenght (flip = wavelenght you want to follow and make positive). It's inactivate by default (no correction).
'''

def Absorption(Path,File,Timezeromm,iniWL,cutWL,iniPos,cutPos,flip=None):
    import numbers
    File = np.array(File)
    Filename = Path + File[0]
    name = File[0].partition('.txt')
    name = name[0].replace("_", " ")
    F = open(Filename,'r')
```

```
    N1='smth'
    while not '<Wavelengths>' in N1:
        N1 = F.readline()
    R = F.readline()
    R = R.split(' ')
    Wavelength = np.array(list(map(float, R)))
    indexWL = Wavelength.shape[0]
    N1 = F.readline()
    N1 = F.readline()
    R = F.readline()
    R = R.split(' ')
    TimeDelay = np.array(list(map(float, R)))
    indexTD = TimeDelay.shape[0]
    N1 = F.readline()
    N1 = F.readline()
    R = F.readlines()[0:indexTD]
    n=[]
    for i in range(indexTD):
        n.append(R[i].split(' '))
    IntensityProbe=np.array(n)
    F = open(Filename,'r')
    N1='smth'
    while not '<Pump+Probe Intensities>' in N1:
        N1 = F.readline()
    R = F.readlines()[0:indexTD]
    F.close()
```

```
    n1 = []
    for i in range(indexTD):
        n1.append(R[i].split(' '))
    IntensityPumpProbe=np.array(n1)
    y = []
    y1 = []
    Absorption2 = np.zeros((indexTD,indexWL))
    for i in range(indexTD):
        if i > iniPos and i < indexTD-cutPos:
            for j in range(indexWL):
                if j > iniWL and j < indexWL-cutWL:
                    y = IntensityPumpProbe[i,j].astype(np.float)
                    y1 = IntensityProbe[i,j].astype(np.float)
                    if isinstance(y,numbers.Number) and isinstance(y1,
numbers.Number) and y/y1>0:
                        Absorption2[i,j]=1000*np.log10(y/y1)
                    else:
                        Absorption2[i,j]=0.0
    #### Cutting and getting the data into arrays ###
    Y=(Timezeromm-TimeDelay[iniPos+1:indexTD-cutPos])/0.15
    X=Wavelength[iniWL+1:indexWL-cutWL]
    Z=Absorption2[iniPos+1:indexTD-cutPos,iniWL+1:indexWL-cutWL]
    if flip != None:
        iflip = find_value(X,flip)[0]
        for i in range(Y.shape[0]):
            if Z[i,iflip] < 0:
```

```
87                  Z[i,:]=-Z[i,:]
88      np.savetxt('./Wavelength.txt',X,fmt='%f')
89      np.savetxt('./Time delay.txt',Y,fmt='%f')
90      np.savetxt('./Time-resolved signal.txt',Z,fmt='%f')
91      return X,Y,Z,name
```

Listing A.1: Python example

Once the time-resolved data file from Snoop is processed through above python code in Spyder, three arrays will be generated to store wavelength (nm), time delay (ps), and the absorption/reflection signal. Note that the absorption/reflection signal is a 2D-array, and each data point means the signal intensity at certain wavelength and time delay.

A.2 Oscillation Component Analysis from Time-resolved Data

```
1 ### 1st ANALYSIS METHOD CONVENTIONAL FFT ###
2 '''
3 Returns residuals from a range of the (StartE,StopE), fits them from T1
4 and then calculates the FFT spectrum.
5 %X = Wavelenght.
6 %Y = Time Delay.
7 %Z = Signal matrix. Ideally, it should be chirp corrected.
8 %StartE = Wavelength you would like to start averaging.
9 %StopE = Wavelength you would like to stop averaging.
```

```
%freqIni = lower limit for the phonon frequency spectrum.
%freqEnd = higher limit for the phonon frequency spectrum.
If is bigger than (1/temporal steps) then uses the latter as freq limit.
%plot = True or False. By default it will show the plot, but it can be
    turned off (False).
'''
def Phonon(X,Y,Z,StartE,StopE,freqIni,freqEnd,plot=True):
    from lmfit import Model as lmModel
    import scipy.fftpack
    from scipy.constants import speed_of_light,pi
    iE = find_value(X,StartE)[0]
    iE1 = find_value(X,StopE)[0]
    PhononMean = np.mean(Z[:,iE:iE1],axis=1) # average of data across
    probe energies.
    iCut = find_value(Y, T1)[0] # down limit in time to fit
    iCut1 = find_value(Y,T2)[0] # up limit in time to fit

    ### SUBSTRATE ELECTRONIC BACKGROUND and GET RESIDUALS###
    def Fit(x,A,B,C):
        return A*x+B
    gmodel = lmModel(Fit)
    result = gmodel.fit(PhononMean[iCut:iCut1], x=Y[iCut:iCut1],A=1.0,B
    =10.0,C=0.0)
    Residuals = PhononMean[iCut:iCut1]-result.best_fit

    ### CONVENTIONAL FFT of RESIDUALS ###
```

```
33      Npts = Y[iCut:iCut1].shape[0]
34      Npad = int(Npts*5.)
35      TimeUnit = (Y[iCut:iCut1].max()-Y[iCut:iCut1].min())/float(Npts) #
    sample spacing
36      yf = scipy.fftpack.fft(Residuals,Npts+Npad)
37      xf = np.linspace(0.0,1.0/TimeUnit, Npts+Npad)
38      xf_cm = xf*1E10/speed_of_light
39      iFreq1 = find_value(xf_cm,freqIni)[0]  # cut-off frequency down-limit
    .
40      freqLim = 1.0/TimeUnit*1E10/speed_of_light
41      if freqEnd > freqLim:
42          iFreq2 = find_value(xf_cm,freqLim)[0]  # cut-off freq. upper-
    limit.
43      else:
44          iFreq2 = find_value(xf_cm,freqEnd)[0]  # cut-off freq. upper-
    limit.
45      xf_cm = xf_cm[iFreq1:iFreq2]
46      Y_f = 2.0/Npts*np.abs(yf[iFreq1:iFreq2])
47
48      #### MAKING THE FFT PLOT TO EVAULATE FITTING RESULT ###
49      if plot == True:
50          fig = plt.figure(figsize=(10, 8))
51          plt.subplots_adjust(left=None, bottom=None, right=None, top=None,
    wspace=None, hspace=None)
52          gs0 = gridspec.GridSpec(2,2)
53          ax0 = plt.Subplot(fig, gs0[0,:])
```

```
54          fig.add_subplot(ax0)
55          ax1 = plt.Subplot(fig, gs0[1,0])
56          fig.add_subplot(ax1)
57          ax2 = plt.Subplot(fig, gs0[1,1])
58          fig.add_subplot(ax2)
59          ax0.plot(Y,PhononMean,'ro')
60          ax0.plot(Y[iCut:iCut1],result.best_fit,'-k',label='Linear Fit')
61          ax0.set_ylabel('Transient signal', fontsize=Nsize)
62          ax0.set_xlabel('Delay / ps', fontsize=Nsize)
63          ax1.plot(Y[iCut:iCut1],Residuals,'-',lable='Residuals')
64          ax1.set_ylabel('Residuals', fontsize=Nsize)
65          ax1.set_xlabel('Delay / ps', fontsize=Nsize)
66          ax2.plot(xf_cm,Y_f,'-')
67          ax2.set_xlabel('Frequency / cm$^{-1}$', fontsize=Nsize)
68          ax2.set_ylabel('FFT intensity / a.u.', fontsize=Nsize)
69          plt.savefig('FFT.png',format='png')
70          plt.show()
71      return Y[iCut:iCut1],Residuals,xf_cm,Y_f
72
73  ### 2nd SHORT TIME FFT (SPECTROGRAM) ###
74  '''Using a temporal windows (called Hamming), we are windowing the
        residuals in time-domain
75  and doing FFT from each segment. That computes a full FFT spectrum for
        each time-step.
76  This function returns Time delays, frequency values and a matrix with FFT
        amplitudes
```

```
%array_time = Time Delays
%array_absorption = Residuals in time domain (e.g. from Phonon function).
%freqIni = lower limit you want to display.
%freqEnd = higger limit you want to display.
%plot = True or False. By default it will show the plot, but it can be
    turned off (False)
'''
def Spectrogram(array_time,Residuals,freqIni,freqEnd,plot=True):
    from scipy.signal import hamming
    from tftb.processing import Spectrogram
    from scipy.constants import speed_of_light
    time_cut = find_value(array_time,Ts)[0] # down limit in time to
    analysis
    Y_short = array_time[time_cut:]
    Residuals = Residuals[time_cut:]
    TimeUnit1=(Y_short.max()-Y_short.min())/float(Y_short.shape[0]) # ps
    per points in plot
    fwindow = hamming(1000)
    spec = Spectrogram(Residuals, n_fbins=2048, fwindow=fwindow)
    spec.run()
    Xf = 1/TimeUnit1*spec.freqs*1E10/speed_of_light
    iFreq1 = find_value(Xf,freqIni)[0]  # cut-off frequency down-limit.
    iFreq2 = find_value(Xf,freqEnd)[0]  # cut-off frequency upper-limit.
    Xf = Xf[iFreq1:iFreq2]
    Zf = spec.tfr[iFreq1:iFreq2,:]
    if plot == True:
```

```
100         contours = plt.contourf(Y_short,Xf,Zf,300, cmap='terrain', alpha
    =0.8)
101         plt.xlim(Y_short.min(),Y_short.max())
102         plt.xlabel('Delay/ps)', fontsize =Nsize)
103         plt.ylabel('Phonon Freq. (cm$^{-1}$)', fontsize =Nsize)
104         plt.tick_params(labelsize=Nsize)
105         cbar = plt.colorbar(mappable=contours)
106         cbar.set_label('Intensity (a.u.)', fontsize =Nsize)
107         cbar.ax.tick_params(labelsize=Nsize)
108         plt.tight_layout()
109         plt.show()
110     return Y_short,Xf,Zf
111
112 ### 3rd CWT: construct a time-frequency representation of a signal ###
113 '''
114 Calculates CWT and returns a cwt cross section at a particular width(ibin
    ), the FFT frequencies and amplitudes at that cross section, and the
    complete cwt matrix
115 %array_time = Time delays.
116 %Residuals = Residuals in time-domain.
117 %ibin = integer from 1 to 100 that is proporcional to the width of the
    wavelet.
118 %freqIni = lower limit you want to display.
119 %freqEnd = higger limit you want to display.
120 %plot = True or False. By default it will show the plot, but it can be
    turned off (False)
```

```
'''
def CWT(array_time,Residuals,ibin,freqIni,freqEnd,plot=True):
    from scipy import signal,fftpack
    from scipy.constants import speed_of_light
    widths = np.arange(1.,100.,1.) # array of bins (widths) where you
   want to investigate.
    cwtmatr = signal.cwt(Residuals,signal.ricker, widths) # builds the
   CWT matrix.
    width_s = str(round(widths[ibin],1))
    cwt_bin = cwtmatr[ibin,:] # Cross section of the CWT matrix at ibin.
    ### FFT after CWT ###
    Npts = cwt_bin.shape[0]
    Npad = Npts*5
    TimeUnit=(array_time.max()-array_time.min())/float(Npts)
    yf = fftpack.fft(cwt_bin,Npts+Npad)
    xf = np.linspace(0.0, 1.0/TimeUnit,Npts+Npad)
    xf_cm = xf*1E10/speed_of_light
    iFreq1 = find_value(xf_cm,freqIni)[0]
    iFreq2 = find_value(xf_cm,freqEnd)[0]
    xf_cm = xf_cm[iFreq1:iFreq2]
    Y_f = 2.0/Npts * np.abs(yf[iFreq1:iFreq2])
    freq_osc_s = str(round(xf_cm[Y_f.argmax()],1))
    ###########
    if plot == True:
        fig = plt.figure(figsize=(10   8 ))
        plt.subplots_adjust(left=None, bottom=None, right=None, top=None,
```

```
 wspace=None, hspace=None)
145         gs0 = gridspec.GridSpec(2,2)
146         ax0 = plt.Subplot(fig, gs0[0,:])
147         fig.add_subplot(ax0)
148         ax1 = plt.Subplot(fig, gs0[1,0])
149         fig.add_subplot(ax1)
150         ax2 = plt.Subplot(fig, gs0[1,1])
151         fig.add_subplot(ax2)
152         ax0.imshow(cwtmatr, extent=[array_time.min(), array_time.max(),
    cwtmatr.shape[0],0], cmap='terrain', aspect='auto', vmax=abs(cwtmatr)
    .max(), vmin=-abs(cwtmatr).max())
153         ax0.set_ylabel(r'$\#$ bins', fontsize=Nsize)
154         ax0.set_xlabel('Delay / ps', fontsize=Nsize)
155         ax0.tick_params(labelsize=Nsize)
156         ax1.plot(array_time,cwt_bin,'-r',label = 'w = %s' %(width_s))
157         ax1.set_xlabel('Delay / ps', fontsize=Nsize)
158         ax1.set_ylabel('Intensity / a.u.', fontsize=Nsize)
159         ax1.tick_params(labelsize=Nsize)
160         ax1.legend()
161         ax2.plot(xf_cm, Y_f,'-b',label='%s cm$^{-1}$' %(freq_osc_s))
162         ax2.set_xlabel('Frequency / cm$^{-1}$', fontsize=Nsize)
163         ax2.set_ylabel('FFT intensity / a.u.', fontsize=Nsize)
164         ax2.tick_params(labelsize=Nsize)
165         ax2.legend()
166         plt.tight_layout()
167         plt.show()
```

```
168     return cwt_bin,cwtmatr,xf_cm,Y_f
```

A.3 Single Value Decomposition and Global Fit

```
1  import numpy as np
2  import matplotlib.pylab as plt
3  ### INPUTS ###
4  Z = np.loadtxt('Time-resolved signal.txt')
5  ### SVD ANALYSIS: estimate the number of signal components ###
6  u, s, v = np.linalg.svd(Z)
7  print(s)
8  ### NUMBER OF COMPONENTS ###
9  i = 10000
10 j = 0
11 thresh = 1000.0*np.mean(s[-10:])
12 # thresh could be modify based on the data
13 while i > thresh:
14     i = s[j]
15     j += 1
16 ### PLOT RESULT ###
17 plt.figure(figsize=(8,6))
18 plt.plot(s[:30], '-ro')
19 plt.title('SVD analysis: Diagonal of $\Delta$Absorption matrix (
       Components= %s)' %(j-1), fontsize=Nsize)
20 plt.xlabel('\# bins', fontsize=Nsize)
```

```
plt.ylabel('Intensity / a.u.', fontsize=Nsize)
plt.tick_params(labelsize=Nsize)
plt.tight_layout()
```

Once using the SVD analysis to estimate the number of decaying component, a function with certain numbers of exponential component could be defined to analyze.

```
from lmfit import minimize, Parameters, report_fit
### INPUTS ###
icut = 20 # down limit in time to analysis
X = np.loadtxt('Wavelength.txt')
Y = np.loadtxt('Time delay.txt')
Z = np.loadtxt('Time-resolved signal.txt')
ts = []
As = []
x1 = []
data = []
Time = Y[icut:]
for i in range(0,X.shape[0],10):
    # Instead of fitting at each wavelength, we fit every 10 points. This
    could be modify considering the size of data.
    x2 = X[i]
    y1 = Z[icut:,i]
    x1.append(x2)
    data.append(y1)
data = np.array(data)
ndata = data.shape[0]+1
```

```
x1 = np.array(x1)
def Func(x, A1, t, A2):
    return  A1 * np.exp(-x/t)+ A2 # one decaying component
def exp_dataset(params, i, x):
    A1 = params['A1_%i' %(i+1)]
    t = params['t_%i' %(i+1)]
    A2 = params['A2_%i' %(i+1)]
    return Func(x, A1, t, A2,)
def objective(params, x, data):
    # calculate total residual for fits to several data sets held in a 2D
    array, and modeled by Func
    resid = 0.0*data[:] # make residual per data set
    for i in range(data.shape[0]):
        resid[i, :] = data[i, :] - exp_dataset(params, i, x)
        # now flatten this to a 1D array, as minimize() needs
    return resid.flatten()
fit_params = Parameters() # create sets of parameters, one per data set
for iy, y in enumerate(data):
    fit_params.add('A1_%i' % (iy+1), value=5.0, min=0.0, max=50.0)
    fit_params.add('t_%i' % (iy+1), value=50.0, min=45.0, max=105.0)
    fit_params.add('A2_%i' % (iy+1), value=3.0, min=0.0, max=50.0)
for iy in (range(2,ndata,1)):
    fit_params['t_%i' % iy].expr = 't_1'
# now constrain all values of sigma to have the same value by assigning
   sig_2, sig_3, ... to be equal to sig_1
out = minimize(objective, fit_params, args=(Time, data))
```

```
report_fit(out.params)
for i in range(1,data.shape[0],1):
    ts += [[x1[i], out.params['t_%i' %i].value]]
    As += [[x1[i], out.params['A1_%i' %i].value, out.params['A2_%i' %i].
   value]]
FitPara1 = np.array(ts)
FitPara2 = np.array(As)
FitPara1_s = str(round(FitPara1[1,1],2))
### PLOT FITTINGS ###
for i in range(0,data.shape[0],10):
    y_fit = exp_dataset(out.params, i, Time)
    plt.plot(Time, data[i, :], 'o', Time, y_fit, '-')
plt.show() # evaluate the fitting result
### SPECTRA ###
plt.figure(figsize=(10,8))
plt.plot(FitPara2[:,0],FitPara2[:,1],'-r', label='A1')
plt.plot(FitPara2[:,0],FitPara2[:,2],'-k', label='A2')
plt.plot(FitPara2[:,0],FitPara2[:,1]*np.exp(-0.5/57)+FitPara2[:,2], label
   ='Global Fitting')
plt.legend(fontsize=Nsize)
plt.title('Using F($\lambda$,t) = A1($\lambda$)*exp(-t/$\\tau$) + A2($\
   lambda$), with $\\tau$= %s ps' %(FitPara1_s), fontsize=Nsize)
plt.xlabel('Wavelength / nm', fontsize=Nsize)
plt.ylabel('$\Delta$Absorption / $\Delta$mOD', fontsize=Nsize)
plt.tick_params(labelsize=Nsize)
plt.tight_layout()
```

```
67 plt.show()
```

Appendix B

Laser irradiation test for $MoTe_2$ thin films

Test A1: 28 nm-thick $MoTe_2$ sample – strain buildup

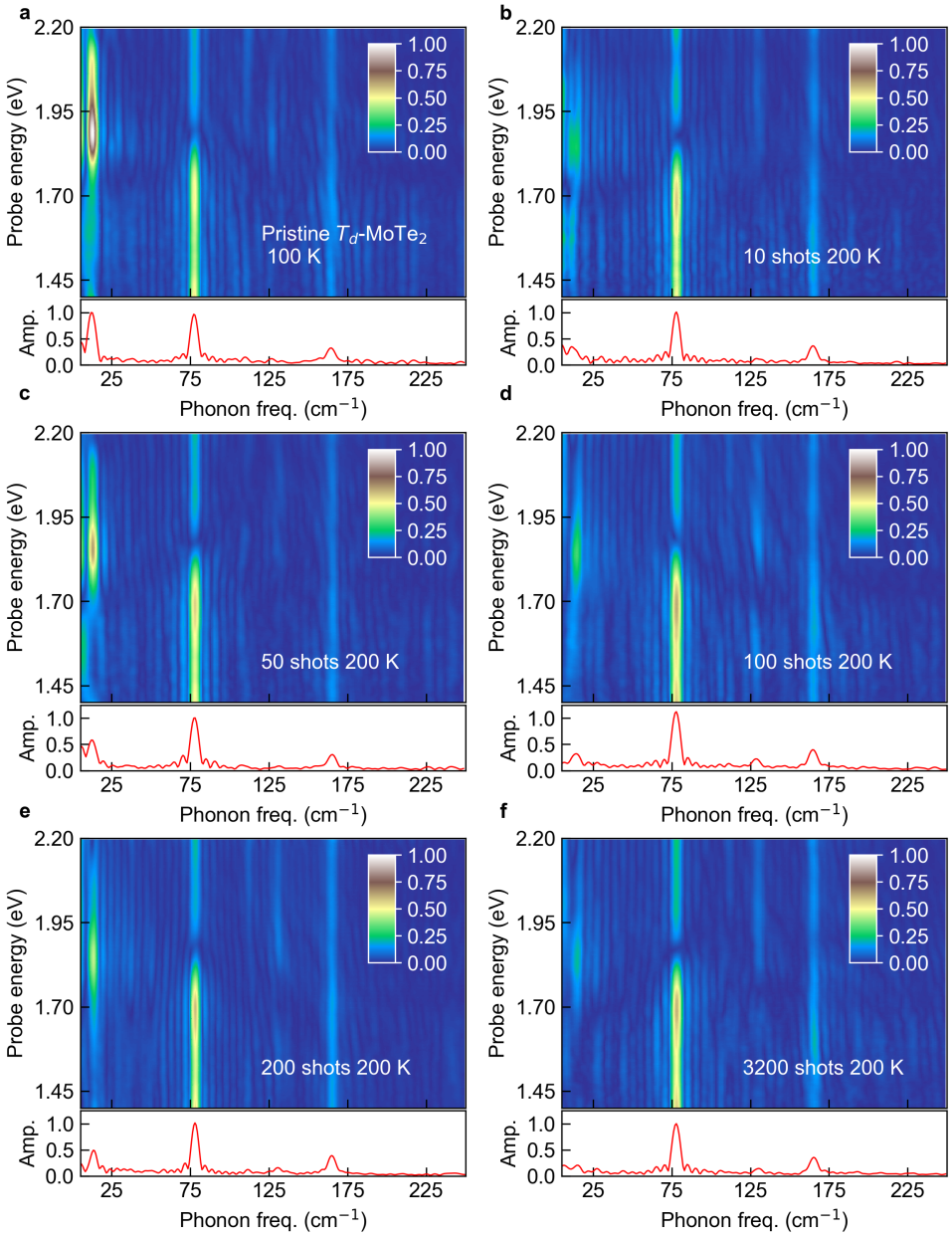

Figure B.1: Fourier power spectra for laser irradiation test A1. (a) Pristine sample. (b-f) Same specimen following laser irradiation exposures. The temperatures and cumulative number of laser shots employed in irradiation cycles are indicated in each panel. Irradiation exposures were carried out with $F = 2.6$ mJ·cm^{-2}. All tr-bb-TA measurements were performed at 100 K, $F \approx 0.4$ mJ·cm^{-2}.

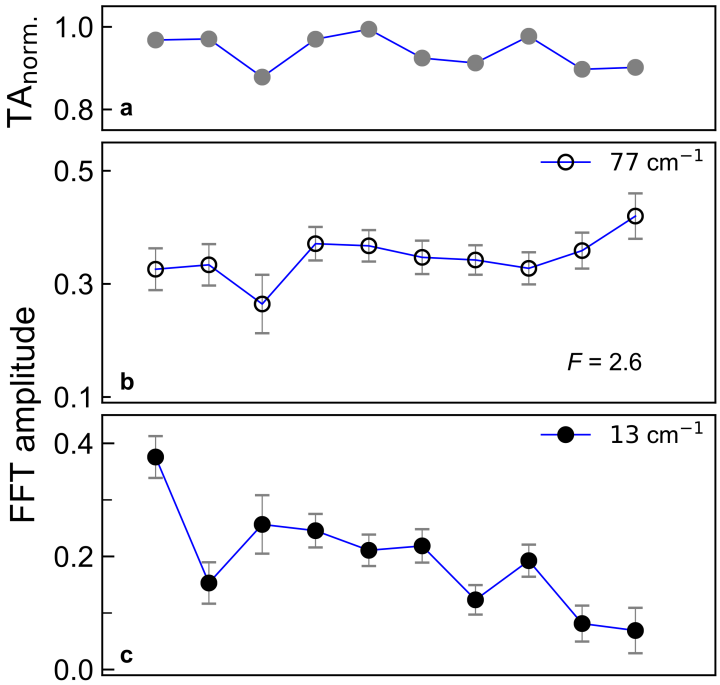

Figure B.2: Laser induced changes as a function of the cumulative number of laser irradiation pulses for laser irradiation test A1. From left to right the number of cumulative laser shots is 0, 10, 20, 30, 40, 50, 100, 200, 3200, and 5200. (a) Recorded maximum magnitude of TA signal, normalized by its initial value. (b) Fourier amplitude of the 77 cm^{-1} mode. (c) Fourier amplitude of the 13 cm^{-1} mode. The temperatures and fluences employed during laser irradiation exposures are indicated in the figure. All tr-bb-TA measurements were carried out at 100 K, $F \approx 0.4$ mJ·cm^{-2}.

Test A2: 27 nm-thick $MoTe_2$ sample – strain buildup

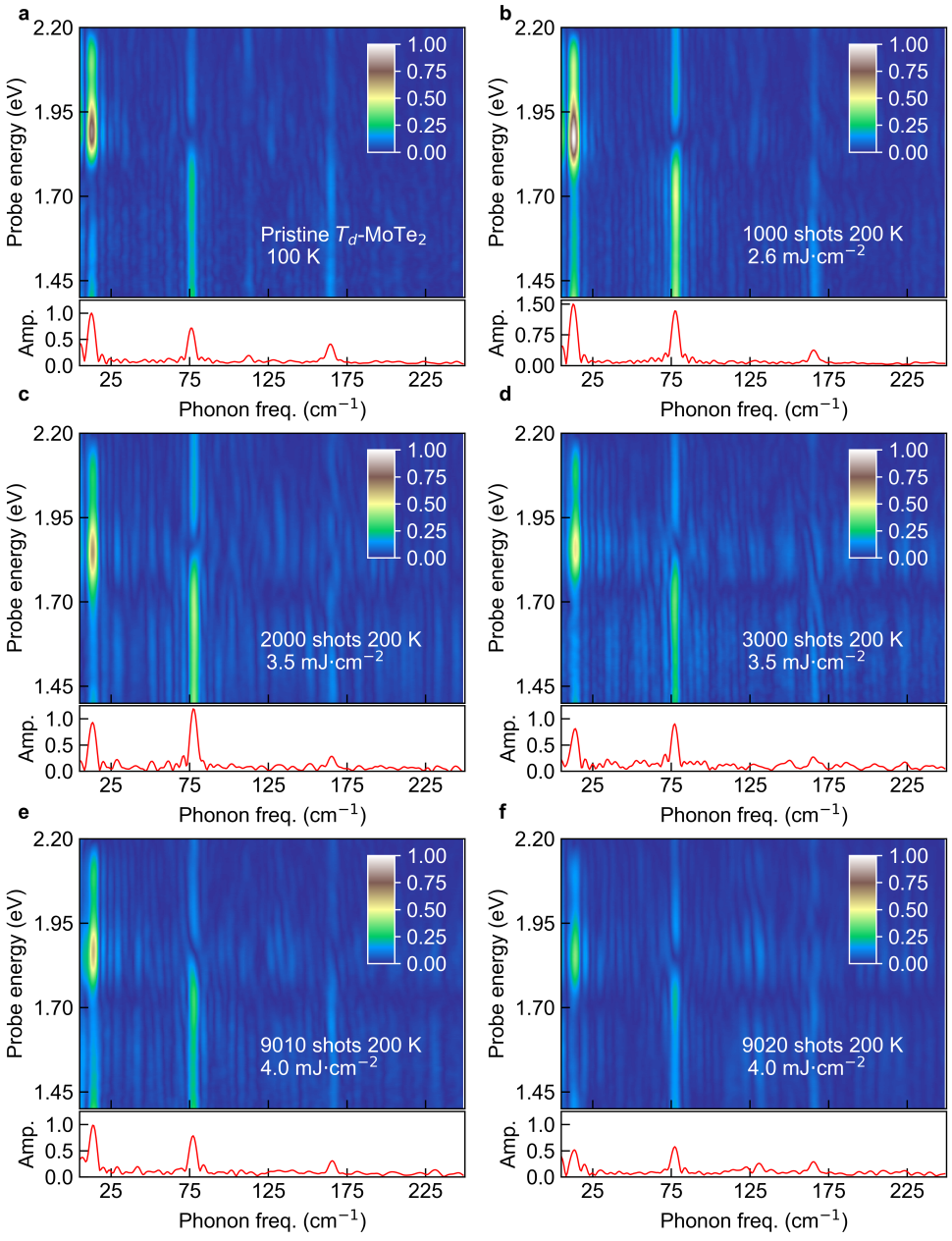

Figure B.3: Fourier power spectra for laser irradiation test A2. (a) Pristine sample. (b-f) Same specimen following laser irradiation exposures. The temperatures and cumulative number of laser shots employed in irradiation cycles are indicated in each panel. Irradiation exposures were carried out with $F = 2.6$ mJ·cm^{-2}. All tr-bb-TA measurements were performed at 100 K, $F \approx 0.5$ mJ·cm^{-2}.

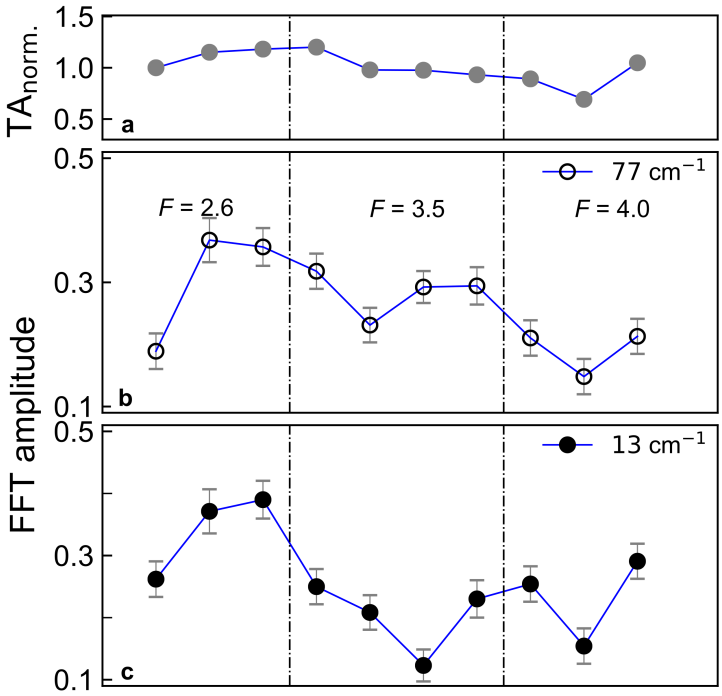

Figure B.4: Laser induced changes as a function of the cumulative number of laser irradiation pulses for laser irradiation test A2. From left to right the number of cumulative laser shots is 0, 10, 1000, 2000, 3000, 6000, 9000, 9010, 9020, 9050. (a) Recorded maximum magnitude of TA signal, normalized by its initial value. (b) Fourier amplitude of the 77 cm^{-1} mode. (c) Fourier amplitude of the 13 cm^{-1} mode. Fluences employed during laser irradiation exposures are indicated in the figure. Irradiation cycles were performed at 200 K. All tr-bb-TA measurements were carried out at 100 K, $F \approx 0.5$ mJ·cm^{-2}.